POLITECNICO DI TORINO

Master's Degree in Energy and Nuclear Engineering

Master's Degree Thesis

Improved interfaces and innovative joining strategies for high-pressure SOEC integration

Supervisors

Prof. Federico Smeacetto
Dr. Fabiana D'Isanto
Dr. Simone Anelli

Candidate

Paolo Serafini

Academic Year 2023/2024

ABSTRACT

Green hydrogen is emerging as a versatile chemical and energy carrier in a context promoting decarbonisation and transition to renewable energy sources. Power-to-H2 systems can be successfully integrated with renewable energy systems by using excess electricity for H2 production. Solid Oxide Electrolyzers Cells (SOECs) are one of the most attractive options due to their high electrical conversion efficiency and potential for CO2 co-electrolysis. This advantage is related to their elevated operating temperatures, ranging from 600 to 900 °C, which allow a significant increase in the transport processes involved in the stack operation. Nevertheless, high temperatures have a strong impact on system's durability due to thermal degradation issues. Therefore, the stack components must comply with severe thermal, chemical and mechanical conditions. A key component for long-term reliable operation is the interface between the metallic interconnects and the ceramic electrolyte, which must fulfil the important tasks of joining cell components, providing electrical insulation and preventing gas mixing. Glass-ceramics (GCs) are among the most promising sealing materials due to their thermochemical and thermomechanical compatibility with other stack components and their mechanical properties. From the perspective of large-scale production and commercialization, integrating stack fabrication with Additive Manufacturing (AM)-3D printing techniques offers significant benefits, including reduced energy consumption, material wastage, and machining steps. This thesis was developed in the context of the HyP3D Horizon Europe project (GA 101101274) aiming at the realization of ultra-high power density SOEC stacks of 2.14kW. New strategies to achieve high-pressure difference resistant joints, with a surface engineering approach, such as laser modification of the interconnect, thus improving the overall joining reliability, will be reviewed and discussed in this MSc thesis. Since the reliability of the joined materials over a pressure difference plays a key role in preventing gas mixing and consequent stack failure, 3D-printed corrugated cells with embedded functionality will be joined to enhanced surface-modified interconnect-sealant interfaces. Two barium-based and one strontium-based commercial glass systems are characterized for pressurized SOEC applications at 850 °C and 5 bar. Thermochemical and thermomechanical compatibility of the GCs with the interconnector and electrolyte materials are evaluated through microstructural and compositional evaluation. Rheological characterization of glass powder pastes is performed for Robocasting deposition, and the effect of printing parameters variation is analysed observing the extruded filaments. The shear strength of the Crofer22APU-to-3YSZ joint is estimated through a single lap offset (SLO) testing. Finally, the effect of increased surface roughness, measured through profilometric analysis, on substrates' wettability and mechanical properties is investigated through laser modification on Crofer22APU. An Infrared Nanosecond fibre laser treatment leading to a suitable roughness on the interconnect surface is demonstrated to be a feasible approach to obtain mechanical interlocking effect, thus enhancing the adhesion of the sealing system. The shear strength results of the improved joined interfaces will be discussed, showing the positive effects of the optimal surface processing on the joining strength and reliability.

INDEX

LIST OF FIGURES

LIST OF TABLES

1. INTRODUCTION

1.1. Role of Hydrogen

The global energy scenario is experiencing a process of transition and diversification towards alternative energy sources in order to mitigate greenhouse gases emissions and ensure energy security. This shift is primarily motivated by the major issue of climate change and due to the world's complex economical and geopolitical context.

The International Energy Agency (IEA) annual report states that approximately the 72% of the global greenhouse gases emissions are imputable to fossil CO_2 (Carbon Dioxide). In 2023, CO_2 emissions were equal to 37.4 Gt, the 1.1% higher with respect to 2022 [1]. Emissions are forecasted to reach 34 Gt of CO_2 by 2050, far from the net zero emissions (NZE) target of the 2015 Paris Agreement. IEA have presented pathways for achieving decarbonisation and limiting global warming to 1.5 °C [2], posing electrification, energy efficiency, energy storage, sustainable biomass and carbon capture technologies as crucial for the achievement of the NZE by 2050.

Under these premises, hydrogen can be relevant in the decarbonisation of the power generation and hard-to-abate sectors, not only as fuel but also as chemical, energy carrier and storage media, as reported in the NZE long-term scenarios to 2050 in **Figure 1.1**. However, referring to 2022 data, hydrogen demand corresponds to 95 Mt, limited to refining, chemical, and steel industry [3].

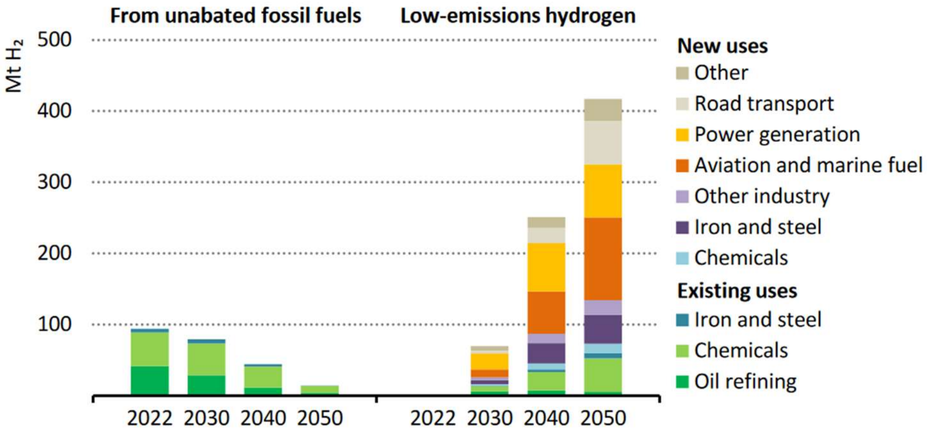

Figure 1.1 *Global hydrogen demand in the NZE Scenario, 2022-2050 [2]*

As far as hydrogen production is concerned, it mostly relies on traditional routes, namely steam methane reforming and coal gasification. Referring to H_2 colour classification, hydrogen obtained with this processes is named grey and brown hydrogen, respectively. A possible alternative to curb CO_2 emissions is combining these technologies with Carbon Capture Utilisation and Storage systems (CCUS). The hydrogen produced from the combination of traditional methods and CCUS is called blue hydrogen. Nevertheless, in a scenario where energy transition is leaded by renewable energy sources, intrinsically characterized by an intermittent nature, the most interesting option is their integration with low emission H_2-production technologies. In fact, hydrogen can be produced exploiting excess electricity from photovoltaic and wind technologies in the so-called power-to-hydrogen technologies. Particularly, the most interesting production pathway, due to significant steps in development and commercialisation of a variety of devices which rely on high production rates and conversion efficiencies, is represented by water electrolysis technologies, referred to as electrolyzers [4]. Hydrogen produced through renewable electricity is called green hydrogen. Other technologies for clean hydrogen production relies on photocatalytic water splitting and thermochemical water splitting [5]. Hydrogen colours are summarized in **Figure 1.2**

In the NZE scenario, a global installed electrolysis power of 3300 GW is expected by 2050, versus the 1 GW of installed power at present days, which contributes to the 0.1% of the global hydrogen demand. As proposed in *Global Hydrogen Review* 2023, a first option to scale up low-emission technologies for hydrogen production relies on transitioning the existing hard-to-abate sectors to clean hydrogen. Undoubtedly, one of the key factor in the spreading of low emissions hydrogen technologies are the hydrogen production costs. Currently, H_2 - production costs from emerging technologies are not competitive with traditional routes. Specifically, H_2 production from fossil sources is in the range 1 ÷ 3 USD/kgH_2, 1.5 ÷ 3.6 USD/kgH_2 from fossil fuels with CCUS and 3.4 ÷ 12 USD/kgH_2 from electrolysis with low-emission electricity [3]. Economies of scale, reduction of low-carbon electricity costs and technological developments in conversion efficiency, will be determining factors in lowering these prices.

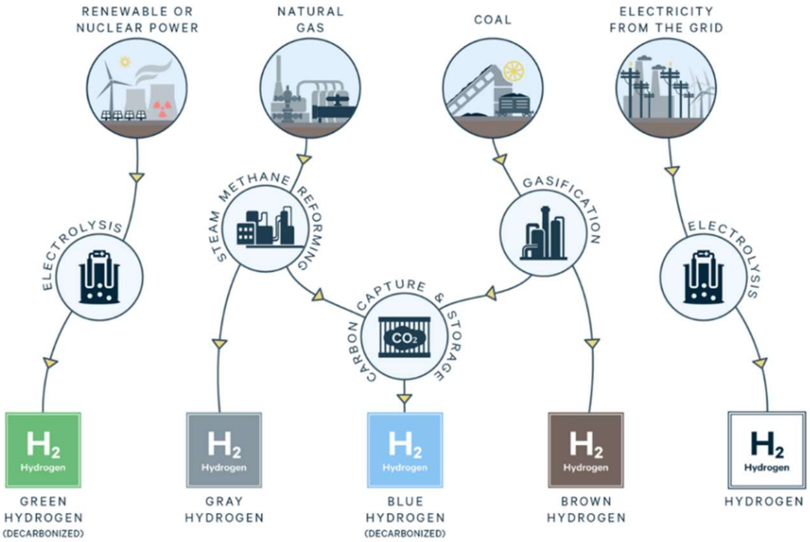

Figure 1.2 *Hydrogen classification "by colors"[6]*

1.2. Electrolysis and Electrolysers: an overview

Electrolysis is a process in which electrical energy is used to drive a nonspontaneous redox reaction. The device used to conduct electrolysis is a particular type of electrochemical cell, called electrolytic cell, which allows the conversion of electrical energy into the chemical energy of a product. On the other hand, when the chemical energy of a fuel is converted into electricity in an electrochemical cell, we refer to it as fuel cell. More specifically, electrolytic and fuel cells are structures able to promote a complete redox reaction by organizing it in two separate steps and in two different parts of the dispositive.

Hydrogen, along with oxygen, can be produced through an electrolytic cell by using electrical energy to split water molecules. The chemical reaction can be expressed as follows (Equation 1.1):

$$2H_2O \xrightarrow[electrical\ energy]{} 2H_2 + O_2 \tag{1.1}$$

Generally, electrolytic cells are classified basing on operating temperature and type of conducted ion through the electrolyte. In **Table 1.1** there are reported the general characteristics of the three main electrolyzers technologies: Alkaline water electrolyzers (AWEs), Proton exchange membrane electrolysis cells (PEMECs) and Solid oxide electrolyzer cells (SOECs).

Table 1.1 *Overview of the main characteristics and operating parameters of the three main electrolyser technologies. Adapted from [4], [7], [8]*

CELL CHARACTERISTICS	AWE	PEMEC	SOEC
Operating Temperature [°C]	65-100	70-90	600-900
Pressure [bar]	25-30	30-80	1
Electrolyte	20-30%	Polymer Membrane	Ceramic
Charge Carrier	OH^-	H^+	O^{2-}
Catalyst	Platinum, nickel	Platinum	Nickel
Fuel Compatibility	H_2O	H_2O	H_2, CH_4, CO_2
Specific Energy Consumption [kWh/Nm^3 of H_2]	3.8-5.4	4.3-5.2	3.6
Development Status	Commercial	Commercial	R&D

Alkaline electrolyzers account for more than the 60% of the global electrolysis installed capacity, followed by PEMEC with the 30%, whereas solid oxide electrolyzers represent approximately the 1% of the total installed capacity [3].

The basic working principle of the three quoted electrolyser cells is reported in **Figure 1.3**.

Alkaline electrolyzers are a well-established commercial technology with systems of the MW scale, operating at a low temperature of 65-100 °C and a pressures between 25-30 bar. AWEs' electrodes are immersed in a liquid electrolyte which is a 30 wt% aqueous solution of potassium hydroxide. They are separated by a diaphragm which allows the passage of hydroxide ions but prevents gas mixing. The electrodes commonly utilized in alkaline electrolysers are composed of porous metal frameworks that are highly conductive and coated with catalysts with a large surface area. These structures facilitate the permeation of the liquid electrolyte onto the electrocatalyst surface, enabling the gases produced at the interface between the liquid electrolyte, solid electrocatalyst, and gas phase to migrate from the electrode to the surrounding environment. One of the main drawbacks of this technology is the high ohmic loss associated to the ions passage through diaphragm and electrolyte [9].

PEMECs present an electrically insulating but ion-conducting polymer membrane as electrolyte. Water is split in oxygen and protons at the anode. These protons pass through the membrane and recombine at the cathode to form hydrogen. In PEM electrolyzers, the catalysts commonly used are platinum for the cathode and an iridium/ruthenium oxide mixture for the anode, both supported on carbon. The proton-conducting membrane is typically Nafion, which is a fluorinated polymer containing sulfonic acid functional groups. Since the need of these types of membranes to be hydrated, their operative temperature is limited at approximately 90 °C, representing a limit of their application. With respect to AWE, PEMEC allows to obtain higher current densities and voltage efficiencies, nonetheless, the durability is reduced, due to membrane lifetime and catalyst loss, and manufacturing costs are elevated [9] [10].

In SOECs, steam is reduced to hydrogen and oxide ions at the interface between the cathode and electrolyte. Then, O^{2-} ions pass through the dense YSZ electrolyte and are oxidized at the anode to form gaseous oxygen. Cathode (fuel electrode) and anode (oxygen electrode) must show specific electrical, thermal and chemical properties, such as high electronic and ionic conductivity, good catalytic activity and thermochemical compatibility with the other components. Generally, the material used for the cathode is a Ni-YSZ composite, whereas a Mixed Ionic-Electronic Conductor (MIEC) material, such as perovskites, is utilized for the oxygen electrode. In general, the high operating temperatures, between 600 and 900 °C, enhance fuel flexibility and reduce susceptibility to fuel impurities with respect to low-temperature electrolysers. In addition, at high temperatures an increase of transport phenomena is observed, leading to higher efficiencies compared to other systems. Nevertheless, this also leads to drawbacks such as long start-up time of the device, higher cost of the components of the Balance of Plant (BOP) and lower durability due to thermal degradation [11].

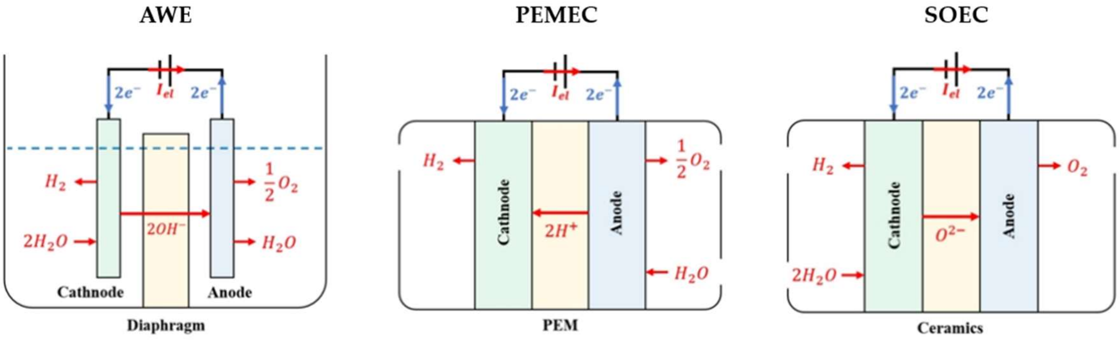

Figure 1.3 *Schemes of the operating principle of AWE, PEMEC and SOEC [12]*

1.3. Solid Oxide Electrolysers Cells

Conversion efficiency from electrical to chemical energy is crucial, as the electrical consumption represents the major component in the hydrogen production cost [3]. As a consequence, it is fundamental to develop cost-efficient technologies. Among other types of electrolyzers, high temperature SOEC are the most efficient ones, with high production yields and a low specific energy consumption of approximately 3.6 kWh/Nm^3 [8], [13]. In addition, SOECs can be used in co-electrolysis processes to generate syngas, which is generally defined as a gaseous mixture of hydrogen, methane, carbon monoxide and carbon dioxide. This can be achieved thanks to its high operating temperatures, ranging from 600 to 900 °C, which allow the reduction of both steam and CO_2 for the production of hydrogen and CO [14]. Another relevant aspect and developing trend is the high-pressure operation of SOEC stacks. Several studies have been done on SOEC pressurized operation from the numerical and experimental point of view. Henke et al. [15] observed through numerical investigation an increase in the Open Circuit Voltage (OCV), in the reaction kinetics and in mass transport processes, using a two-dimensional model in a range of pressures between 0.5 and 20 bar. Riedel et al. performed an experimental test at pressure between 1.4 and 8 bar on a 10-layer SOEC stack, observing an increase in the OCV and a slight positive influence on the performance of the stack, with a small decrease of the activation and diffusion resistance at higher pressures [16]. Jensen et al. found an increase in SOEC efficiency of approximately the 5% shifting from 1 bar to 20 bar the operating pressure, and estimated an investment cost reduction of the 40-50% related to the post- production hydrogen compression system for its use and storage [17].

However, degradation processes due to extended operation at elevated temperatures, and the understating of the other resulting degradation phenomena, are the main issues in long-term operation. Degradation mechanisms related to mechanical instability due to thermal stress, loss of gas-tightness (e.g. due to electrolyte or sealant failure) and electrochemical degradation of cell components (e.g. chromium poisoning of the electrodes or catalyst coarsening and migration) cause premature stack failure [18], [19], [20]. These are the main critical issues related to the scaling up and commercialisation of SOECs [21]. Currently, the two biggest SOECs plants were installed in 2023 in a refinery in Netherlands and in a NASA research centre in California, accounting respectively for a capacity of 2.6 and 4 MW [22].

From the operational point of view, the fundamental elements of a SOEC are two porous electrodes and a dense ionic conducting electrolyte, as shown in **Figure 1.4**. Regarding the working principle, steam is fed to the porous cathode, where, under an external applied voltage between the two electrodes, H_2O molecules are reduced to hydrogen and oxide ions O^{2-}. These ions are transferred through the dense electrolyte to the anode, where they are oxidized. The net reaction is given by the sum of the reduction and oxidation reactions evolving separately at two electrodes, as reported in Equations (1.2) and (1.3).

Fuel electrode electrochemical reaction (Equation 1.2):

$$2H_2O(g) + 4e^- \Leftrightarrow 2O^{2-} + 2H_2(g) \tag{1.2}$$

Oxygen electrode electrochemical reaction (Equation 1.3):

$$2O^{2-} \Leftrightarrow O_2(g) + 4e^- \tag{1.3}$$

As underlined by the bidirectionality of the arrows in the equation, this device could reversibly work both as electrolyzer and fuel cell, converting the chemical energy of hydrogen into electrical energy.

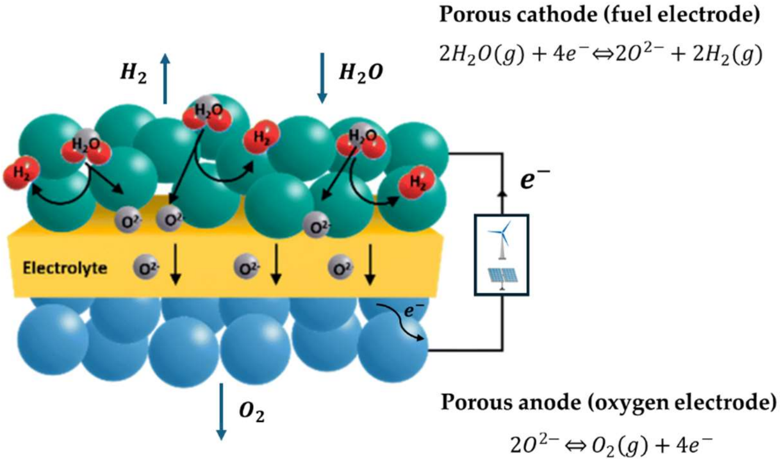

Figure 1.4 *Schematic representation of SOEC operation mode for water electrolysis [13].*

State-of-the-art (SoA) SOECs are processed in two different configurations: planar and tubular (see ***Figure*** **1.5**) . With respect to the planar configuration, the tubular one shows superior mechanical strength and sealing effectiveness. Although planar cells require a larger sealing length between the anode and cathode compartments, they are preferred due to better manufacturability and higher fuel utilisation [23]. In the planar configuration, either the electrodes (generally the fuel electrode) or the electrolyte has the function of supporting the device's structure. The choice is mostly related to balancing factors such as mechanical strength, electrochemical performances, efficiency, and specific application requirements. For example, in the case of the electrolyte supported cell, a trade-off between mechanical stability, which increases with YSZ layer thickness, and ohmic resistance, which decreases with electrolyte thickness, has to be found [11].

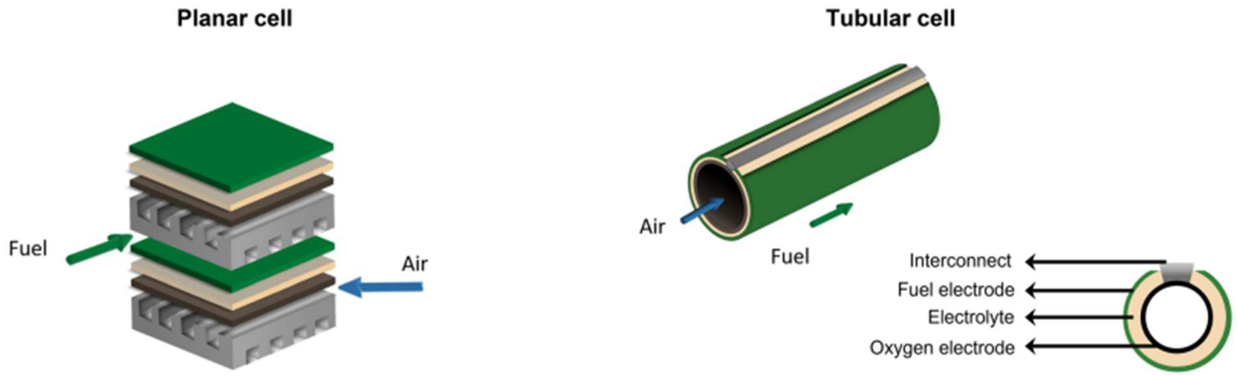
Planar cell

Tubular cell

Figure 1.5 *Schematic representation of SOEC planar and tubular configuration*

1.4. SOEC operation

The minimum electrical energy required to dissociate one mole of water at certain temperature and pressure conditions, equals the molar Gibbs free energy of formation of water at those specific temperature and pressure, according to Equation 1.4 [11], [24].

$$\Delta\bar{G}(T,p) = \Delta\bar{H}(T,p) - T\Delta\bar{S}(T,p) \tag{1.4}$$

Where $\Delta\bar{G}$ is the molar Gibbs free energy of formation of water, $\Delta\bar{H}$ is the molar enthalpy change and $\Delta\bar{S}$ is the molar entropy change. Being an endothermic process, $\Delta\bar{G}(T,p)$ is positive. This result can be applied to both low and high temperature electrolysis. Translating the result in terms of the OCV, it is possible to express the specific ideal energy consumption as reported in **Figure 1.6**. For steam electrolysis, the equilibrium voltage of the cell can be expressed using the Nernst Law (Equation 1.5)[24]:

$$OCV = +\frac{\Delta\bar{G}^\circ(T,p_0)}{4F} + \frac{RT}{4F}\ln\left[\frac{p_{O_2}}{p_0}\left(\frac{p_{H_2}}{p_{H_2O}}\right)^2\right] \tag{1.5}$$

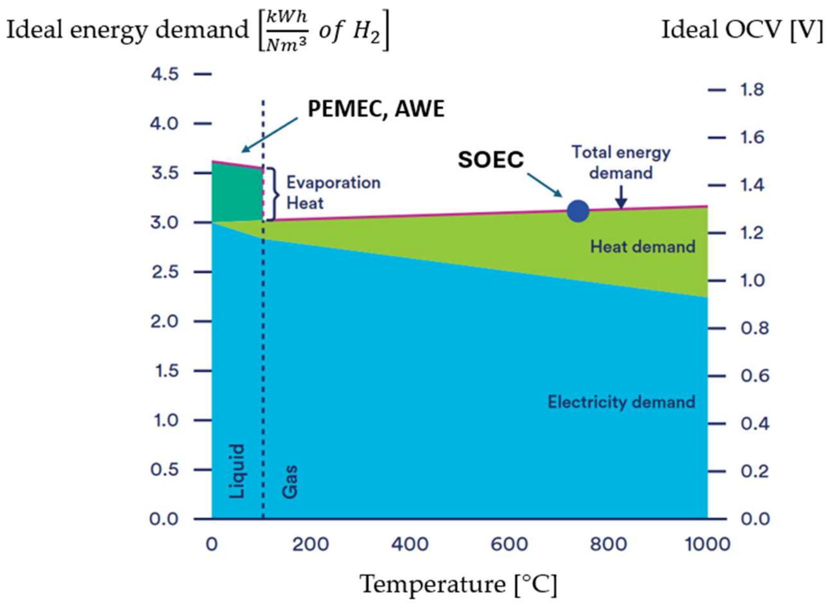

Figure 1.6 *Ideal Energy Demand in Water Electrolysis as a Function of Temperature. Adapted from [19]*

Where p_0 is the standard pressure (generally 1 atm), p_{O_2}, p_{H_2} and p_{H_2O} are the oxygen, hydrogen and water partial pressure at the electrodes, and F is the Faraday constant in $\left[\frac{C}{mol}\right]$. From **Figure 1.6**, it is possible to observe that the minimum specific energy consumption is approximately equal to 3 kWh per $Nm^3\ of\ H_2$. Moreover, it can be noticed how increasing the temperature, the heat demand accounts for a larger share of the total energy demand, reducing the electricity consumption. Considering the Nernst Law, it can also be seen how the partial pressure of the single chemical species influences the OCV.

During the cell operation, both for electrolytic cell and fuel cell operation three main sources of losses can be identified: activation losses, ohmic losses and concentration losses [25]. As a consequence, to drive the whole electrolysis process, an additional voltage is required. More specifically, the cell voltage can be expressed as the sum of the OCV and the single overpotentials associated with each irreversibility, as expressed in Equation 1.6 [11].

$$V_{cell} = OCV + \eta_{act} + \eta_{ohm} + \eta_{conc} \tag{1.6}$$

For electrochemical cells, the voltage evolution is generally expressed as a function of the current density through the so-called polarization curve, which represents the operational map of the device. A typical SOEC polarization curve is reported in **Figure 1.7**.

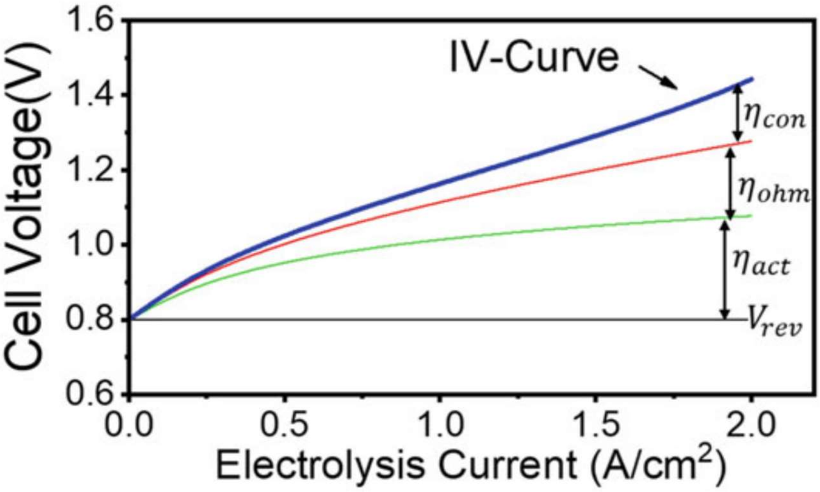

Figure 1.7 *j-V relation of a SOEC and the contribution of different overpotentials, where "j" is the current density in [A/cm^2] [11]*

The theoretical hydrogen production can be calculated through the Faraday's Law (Equation 1.7) [11]:

$$\dot{n_{H_2}} = \frac{I}{z_{H_2}F} \tag{1.7}$$

Where $\dot{n}_{H_2}$ is the hydrogen production rate expressed in $\left[\frac{mol}{s}\right]$, I is the current in [A] and z is the charge number, equal to the number of electrons delivered or recombined by a certain chemical specie ($z = 2$ in the case of hydrogen).

1.5. SOCs Stack Layout and Materials

1.5.1. Cell and Stack Layout

As previously mentioned, the basic unit of a SOC (Solid Oxide Cell) , both SOEC and SOFC, is the cathode-electrolyte-anode layered structure, also called Membrane Electrode Assembly (MEA). Typically, a single unit cell has a power of tens or hundreds of watts, due to low voltage, current density and surface area. Therefore, to increase power, several cells are stacked together in series using metallic interconnectors.

As far as the SOC production process is concerned, it involves several critical steps and it is generally based on tape casting and screen printing techniques [11], [26], [27].

Generally, as shown in **Figure 1.8**, three-types of cell design can be identified for SOC: electrode (fuel or oxygen electrode) supported, electrolyte supported and externally supported. For each type of the listed cell designs, the respective component is thicker than the others to provide mechanical support to the cell. Electrolyte supported cells have emerged as one of the most promising configurations thanks to their mechanical strength, ease of fabrication and lower production costs. Nevertheless, the disadvantage of this design is related to the reduction of performance due to an increase in ohmic losses. In fuel-electrode supported cells, a thick and porous electrode offers mechanical support. In this case, the electrolyte layer can be significantly thinner, decreasing the ohmic resistance and allowing a reduction of the operating temperature. However, electrode-supported SOCs exhibit higher electronic resistance and low redox stability, resulting in higher sensitivity for damage caused by redox cycling [13].

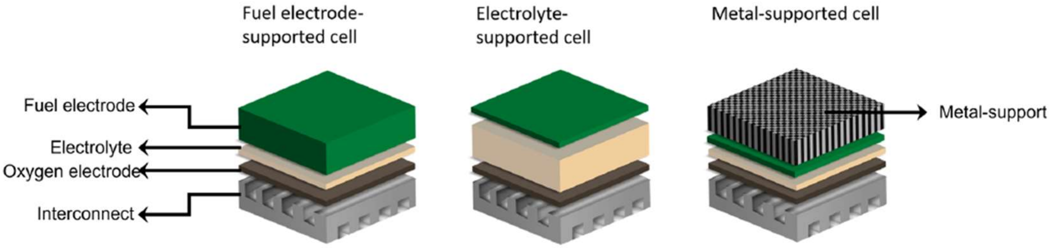

Figure 1.8 *Representation of the three different cell support types reported in the literature: (fuel-) electrode-supported cells, electrolyte-supported cells, and metal-supported cells [13].*

The combination of MEA and metallic interconnector is called a Single Repeating Unit (SRU). A SOEC/SOFC stack is formed by a series of SRUs, as schematized in **Figure 1.9**. Furthermore, in planar SOEC, it is necessary to ensure proper gas tightness in each cell and stack component, to avoid gas mixing and leakages, using a sealing material.

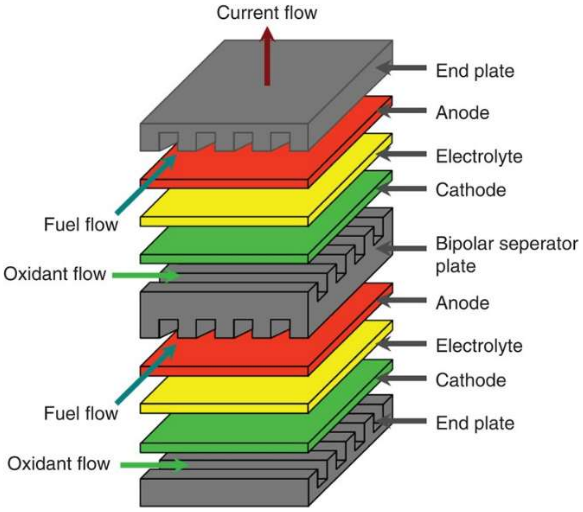

Figure 1.9 *Simple schematization of stack configuration for fuel cell operation [28]*

1.5.2. State-of-the-art materials for SOEC stack

Solid Oxide Electrolysers operate under a harsh environment, from the thermal and electrochemical point of view. Furthermore, single components have to show some specific characteristics and compatibility with the rest of the system. This is the reason why the development of SOEC has increasingly gone towards the reduction of the operating temperatures, to decrease thermal degradation, and towards the selection of durable and efficient materials, to achieve improvements in extended operation performances.

1.5.2.1. Electrolyte materials

The electrolyte in SOEC applications should present good O^{2-} ionic conductivity ($> 0.1\ S/cm$) at operating temperature (600-900 °C), but also low electronic conductivity and molecular diffusivity. In addition, it has to be chemically stable in both reducing and oxidizing environments, being in contact with both oxygen and fuel electrodes. Finally, it should be chemically and thermo-mechanically compatible (e.g., CTE matching) with the other cell components, mechanically resistant to ensure durability and the constitutive material processing should be suitable for large-scale production [11],[13].

Currently, thanks to its good ionic conductivity at the operating temperature, oxygen partial pressure range for ionic conduction and chemical stability, the state-of-the-art material is Yttria-Stabilized Zirconia (YSZ) [11], [13], [29], [30]. YSZ is a ceramic in which the cubic crystal structure of zirconium dioxide (ZrO_2) is made stable at room temperature by an addition of yttrium oxide (Y_2O_3). By the addition of yttria to pure zirconia, Y^{3+} ions replace Zr^{4+} on the cationic sublattice and oxygen vacancies are generated due to charge neutrality. The electrochemical and thermo-mechanical properties of YSZ depend on the molar amount of Y_2O_3 doping as shown in **Figure 1.10**. In particular, 3%mol YSZ (3YSZ) shows better fracture toughness and flexural strength concerning 8%mol YSZ (8YSZ), but a lower ionic conductivity [13]. In electrolyte-supported cells, 3YSZ is generally preferred due to its superior mechanical properties.

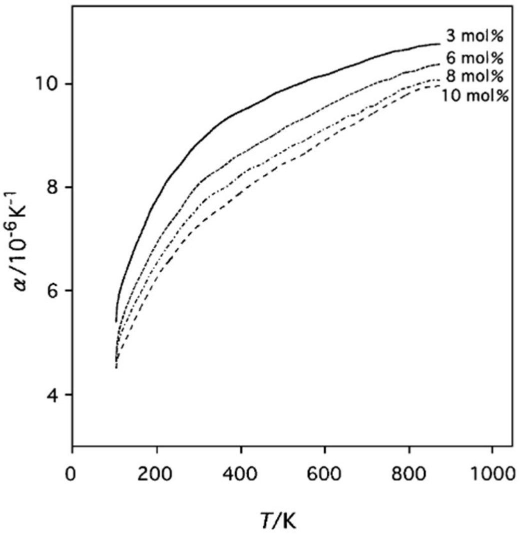

Figure 1.10 *Thermal expansion coefficient of YSZ with various Y_2O_3 content measured by a dilatometer [31].*

Gadolinium-doped ceria is another SoA electrolyte material. It shows higher ionic conductivity concerning 3YSZ and 8YSZ over the whole operating temperature range. Nonetheless, it does not show chemical stability in reducing environment, due to the tendency of Ce^{4+} to reduce to Ce^{3+}, leading to an increase in electronic conductivity and lower mechanical properties [32].

.

1.5.2.2. Electrodes materials

In a SOEC the electrodes should comply with several specifications[11], [33]:

- Interconnected porosity, in order to allow gas diffusion of H_2O, H_2 and O_2
- Sufficient electronic and ionic conductivity (σ_e and σ_i, respectively): $\sigma_e > 100$ S cm^{-1} and $\sigma_i > 0.001$ S cm^{-1} for the oxygen electrode, and $\sigma_e > 100$ S cm^{-1} and $\sigma_i > 0.01$ S cm^{-1} for the fuel electrode [11].

- Good catalytic activity for the Hydrogen Evolution Reaction (HER) and the Oxygen Evolution Reaction (OER), respectively at the fuel and oxygen electrode.
- Chemical stability in the operating environment: reducing for the fuel electrode and oxidant for the oxygen electrode
- Thermomechanical and chemical compatibility with the other components of the cell.

Good electronic and ionic conductivity and interconnected porosity are necessary to limit the overpotentials related to transport processes and to increase the useful reaction area, which can be explained by introducing the Triple Phase Boundary (TPB) concept. TPBs are electrochemically active sites, at the electrode/electrolyte interface, where electrochemical reactions take place. In a SOEC the three involved phases are an ion conductor (electrolyte), an electron conductor (electrode) and a porous phase, which allows the passage of molecules, as shown in **Figure 1.11**. Thanks to the intermixing of these phases, along with good transport of the reactive species, an extended electrochemically active interface can be obtained, improving electrode efficiency [33].

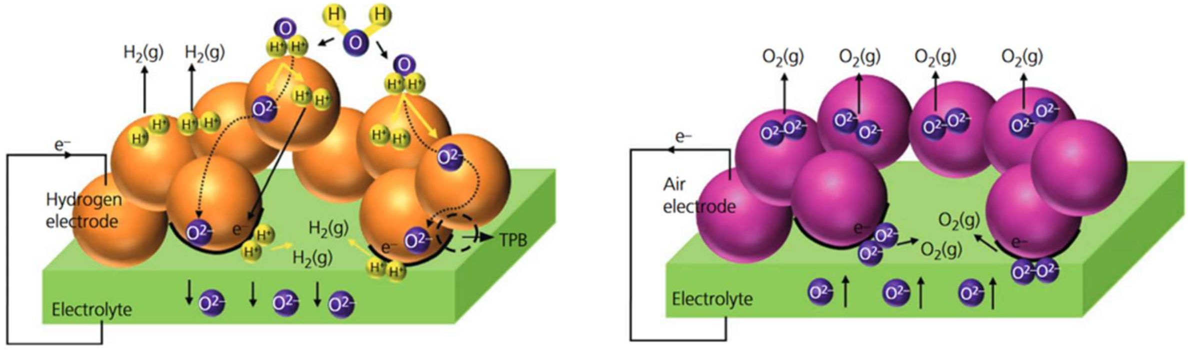

Figure 1.11 *Schematic representation of the transport of molecules, electrons and ions at the two electrodes [20]*

For the fuel electrode, which operates in a reducing environment, the SoA material is a NiO-YSZ cermet [11], [29], [32], [34]. Nickel shows good catalytic activity for HER and high electronic conductivity. However, it has low ionic conductivity. This is the reason for the YSZ addition, which also allows for increased thermomechanical and chemical compatibility with the electrolyte material, chemical stability in reducing environment and TPB density. It should be noted that properties, such as electric conductivity and porosity not only depend on composition but also on the material fabrication process [35], [36].

Regarding the oxygen electrode, lanthanum strontium manganite (LSM) was the most used material [37]. With its perovskite structure ABO_3, LSM shows high chemical stability, good electronic conductivity and excellent catalytic activity for OER. Furthermore, it has high thermomechanical and chemical compatibility with the electrolyte. Nevertheless, single phase electron conductor materials, and in particular LSM, generally have low ionic conductivity. As a consequence, it is often coupled with YSZ to form a composite material [38], [39]. In recent years, to increase the useful active area for OER reactions, the category of Mixed Ionic-Electronic Conductor material has been considered. MIECs are single-phase materials having significant electronic and ionic conductive properties. There are three main families of MIEC materials: perovskites, double perovskites and Ruddlesden-Popper phases [11]. In SOEC applications, Cobalt-based lanthanum strontium oxide (LSC) and lanthanum strontium ferrite oxide (LSCF) perovskite materials are the SoA for the oxygen electrode, showing good mixed ionic-electronic conductivity. In addition, Co-based electrodes present better properties in terms of performance and structural stability [40]. The most relevant critical issue is related to the thermal expansion coefficient, which is higher concerning common electrolyte materials such as YSZ [41]. The three previously mentioned material categories for the oxygen electrode are summarized in **Figure 1.12**: single-phase electron conductor materials (a), ionic/electronic conductive composite materials (b), and single-phase MIEC (c).

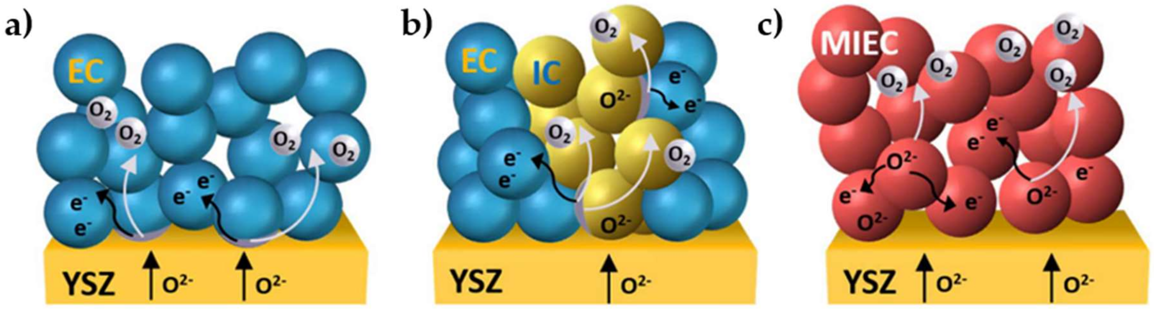

*Figure 1.12 Representation of the microstructures for SOC electrodes: **(a)** Single-phase electron conductor, e.g., LSM; **(b)** ion conduction (IC)/electronic conduction (EC) composite structure, e.g., LSM-YSZ; **(c)** Single-phase MIEC electrode, e.g., LSCF [13].*

1.5.2.3. *Interconnector materials*

As previously mentioned, solid oxide electrolysers are characterized by the repetition of a single unit to form a stack of cells. The element which acts as a bridge between the oxygen electrode and the fuel electrode of adjacent MEAs is named the interconnector. An interconnector should have good electrical conductivity and allow the flow of gases at the two electrodes through a series of channels.

The interconnector must be dense and tight to molecular diffusion, an excellent electrical conductor and thermochemically stable in both oxidizing and reducing environments at high temperatures. Chemical stability is mostly related to the minimization of undesired reactions which lead to the formation of phases that enhance electrical resistivity and induce mechanical degradation. As for the previous components, the CTE of the interconnector should match with that of the electrodes and the electrolyte, to minimize thermal stresses during the heating and cooling of the system [42]. Moreover, it should satisfy criteria related to mechanical stability, strength, creep resistance, ease of fabrication and cost of the material [43].

There are two main classes of materials for the interconnector of SOECs: ceramics materials and metallic alloys. Nowadays, metallic alloys are generally the chosen ones for this kind of application. Low cost, availability, and ease of fabrication make metals more attractive than ceramic oxides as interconnect materials. Currently, the state-of-the-art is represented by the CROFER22 APU, which is a Cr-Fe alloy [11], [13], [29], [32]. Ferritic stainless steel, such as Crofer22 APU, is considered promising thanks to the characteristic of the oxide scale and to the compatible CTE (12.6 $10^{-6}\ K^{-1}$ [11]) with other cell components (electrodes, electrolyte and glass-ceramic sealant). Cr-Fe alloys are characterized by the formation of chromium oxide Cr_2O_3 layers at high temperatures in oxidizing environments. This layer is electrically conductive, nonetheless, excessive growth of the layer would lead to an excessive area specific resistance (ASR). Another relevant issue is related to Cr-evaporation and reduction of chromia (Cr_2O_3) at the oxygen electrode. Subsequent chromia diffusion and deposition at the oxygen electrode/electrolyte interface lead to TPB sites blocking with deterioration of cell performances. This mechanism is schematized in **Figure 1.13** for SOFC application. Therefore, generally, the Cr percentage is kept between 20-25% to ensure limited oxide layer formation and Cr evaporation. A possibility for reducing Cr-induced poisoning is represented by the addition of Manganese (Mn) as an alloying element. The presence of Mn leads to the formation of a second outer Cr-Mn spinel layer which reduces chromia evaporation [13]. Another possible solution to the problem of chromium evaporation and diffusion is the deposition of protective ceramic coatings. Particular attention has been given to materials belonging to the spinel family, such as Co-Mn and Cu-Mn spinels [44].

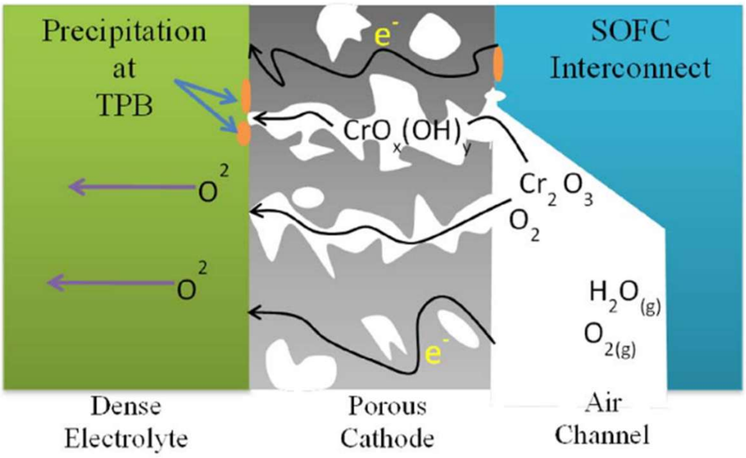

Figure 1.13 *Schematic representation of Cr-poising in SOFC operation [32]*

1.5.2.4. Glass-ceramic sealants

Sealants are used in SOEC stacks to fulfil two main tasks: avoiding gas mixing at the electrodes and providing electrical insulation to avoid short circuits in the stack. Therefore, two of the main characteristics of a sealant are high density, to prevent molecular diffusion of the gases and high electrical resistivity. Moreover, the CTE should be compatible with one of the other components to avoid cracks generation and delamination during the operation. It must be chemically stable in the working environment to avoid undesired reactions with the atmosphere and with the other components. Finally, good adherence to the joined components and mechanical strength of the joined system is needed to ensure mechanical integrity during extended operation [11]. The sealant is placed between one of the two electrodes and the interconnector and between the electrolyte and the interconnector, depending on the cell configuration (e.g. electrolyte supported, or fuel electrode supported cell). In any case, it has to be able to join a metal and a ceramic composite counterpart, as shown for a generic SOC stack configuration in **Figure 1.14**.

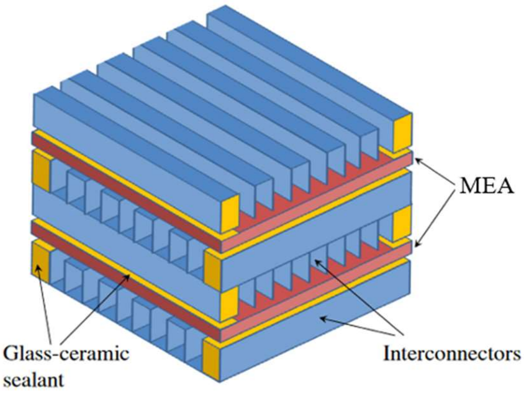

Figure 1.14 *Possible sealing configuration for planar stack [45]*

Sealants for SOFC/SOEC can be classified as rigid and compressive sealants [46]. Compressive sealants are not rigidly bonded to the stack components, therefore the CTE does not need to be strictly compatible with the other materials. Nonetheless, the application of pressure is required to ensure the sealing. On the contrary, rigid sealants do not require applied pressure, but stricter requisites must be fulfilled to have proper adherence, gas tightness and thermomechanical compatibility.

Glass-ceramic (GC) sealants have emerged as one of the most promising rigid sealants thanks to their thermochemical and structural stability [46], [47]. GCs are defined as composite materials constituted of crystals in a glassy matrix. This type of system is obtained through controlled sintering and crystallization of fine powdered glasses. This result is obtained through heat treatment at temperatures around the softening point, leading to partial crystallization with a residual amorphous phase remaining in the system. A relevant advantage of glass-ceramics is related to the possibility of tailoring the glass system composition, acting on the degree of sinter-crystallization and the formed phases during crystallization, to obtain the desired thermal and mechanical properties. Glasses are made of three different types of units: glass formers, glass modifiers and intermediates. Glass formers are compounds, such as silica and boron oxide, which can easily form a glass when cooled from a molten state. Glass modifiers are compounds unable to form glass alone. They cause a breakdown of the glass network and weekly bond to the formed system. Examples of these types of compounds are alkali oxides, earth-alkali oxides and zinc oxides. Finally, intermediates are compounds, such as alumina, titanium oxide and zirconia that cannot form the glass alone, but, in a limited amount, they can take part in the glass network formation [48]. A schematic representation of a multicomponent glass network is shown in **Figure 1.15**. Generally, when designing a glass-ceramic sealant proper balancing between glass formers, modifiers and intermediates has to be found to reach high durability of the stack and minimise degradation.

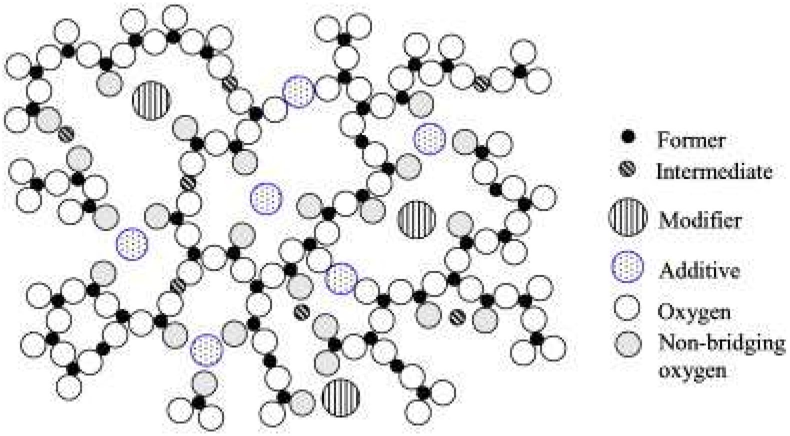

Figure 1.15 *Schematic representation of multicomponent glass network, highlighting glass formers, glass modifiers and intermediates ("additive" in the image)*

The majority of GC sealants that have been analysed and proposed so far are alkaline-earth aluminosilicate-based. Precisely, Ba-based and Sr-based systems, with silica (SiO_2) as glass former, have been taken under consideration. On the other hand, alkali oxides are generally avoided due to their high reactivity with electrolyte and interconnector materials and to the decrease in their electrical resistivity when a voltage is applied [11].

Ba-based glass systems have been taken under consideration due to the improvement in CTE matching with other stack components related to Ba_2SiO_5 phase formation (CTE 12-14 x 10^{-6} K^{-1})[49], good wettability and adhesion with Crofer22 APU interconnect and 3YSZ electrolyte. Furthermore, good chemical stability and electrical resistivity have been observed under applied voltage [50], [51], [52]. From the mechanical point of view, different studies have investigated Ba-containing sealants under tensile and shear stress conditions reporting significant mechanical strength, necessary to withstand the complex thermomechanical tensions arising during stack operation [53], [54], [55]. However, Ba-aluminosilicate GC system is characterized by the formation, during crystallization, of a low-CTE celsian phase ($BaAl_2Si_2O_8$), which might lead to stress generation at the interface with other materials and within the glass-ceramic itself. In addition, barium oxide (BaO) reacts with chromium vapours (such as CrO_3 and $CrO_2(OH)_2$) from interconnector, forming high-CTE barium chromate ($BaCrO_4$). This is one of the main drawbacks of this GC: the large difference between the CTE of barium chromate ((18-20) x $10^{-6}\,K^{-1}$), the sealing glass ((10-13) x $10^{-6}\,K^{-1}$) and the interconnector ((11-13) x $10^{-6}\,K^{-1}$) causes a reduction of the bonding strength and possible detachment between components[11], [32]. Due to these issues, Sr-aluminosilicate GC systems are considered as a possible substitute. With the addition of Sr, a reduction of viscosity and an adjustment of the CTE is observed. Additionally, mechanical properties seem to improve before and after aging at high temperatures with respect to Ba systems [56]. Javed et al. observed a shear mechanical strength at room temperature similar to other barium-containing GC sealants [57] and no formation of undesired Sr-chromates appearance or diffusion of elements across the Croferr22 APU/CG/Crofer22 APU joined system after dual atmosphere test at 850 °C for 1000h [58]. Nonetheless, even in strontium-containing glass ceramics, a too elevated Sr content leads to the formation of a detrimental high-CTE $SrCrO_4$ phase from the reaction with chromium from the interconnector [59] [60].

As far as the pure shear strength of a joint is concerned, three main tests can be identified for the evaluation of the pure shear strength of a joint [61], [62]: single lap offset (SLO) under compression, single lap (SL) under compression and asymmetrical 4-point bending test (A4PB). In the scientific literature on this topic, different results about shear strength are found depending on the type of test. Ferraris et al. [53] compared a torsional test and the ISO 13124 test for the evaluation of shear strength of a calcium-aluminosilicate glass (KMBY) ceramic joined steel for SOFC, obtaining respectively $71 \pm 5\ Mpa$ and $42 \pm 6\ Mpa$. Smeacetto et al. [63] studied the torsional shear strength of joined Crofer22 APU sample with a silica-based, boron-containing glass, obtaining a result of $24\ Mpa$ in the case of as received Crofer22 APU and of $32\ Mpa$ in case of laser processed Crofer22 APU. Da Silva et al. [55] using a pull and shear test setup obtained different values of shear strength for barium-based glass-ceramic systems depending on the barium content, ranging from 3 to 40 Mpa. Javed et al. [57] analysed the shear strength of two Sr-based glasses through SLO test both at room temperature and 800 °C, obtaining, respectively, values of approximately 14 Mpa and 5 Mpa.

1.6. 3D Printing for SOFC/SOEC applications

As mentioned in Section 1.5.1, SOC production relies on multistep processes based on tape casting and screen printing techniques. However, the three-dimensional layered structure of SOC is suitable for the use of techniques that are gaining more and more importance in the energy sector, namely Additive Manufacturing (AM) techniques [26]. AM, or 3D printing, techniques consist in the realisation of a three-dimensional object by deposition of subsequent layers of material using a digital input, i.e. a computer-aided design (CAD) model [26], [27], [64], [65]. Additive Manufacturing allows the production of complex three-dimensional parts using plastic, metallic and ceramic materials. Compared to traditional manufacturing methods, AM has the potential to change at different levels of the production and prototyping chain. Particularly, market environments characterized by demand for customization, flexibility, design complexity and high transportation costs for the delivery of end products can benefit from the introduction of these emerging fabrication techniques [65]. Moreover, 3D printing technologies have exhibited a significant contribution in decreasing the energy consumption connected to manufacturing processes, with a reduction of material wastage and the elimination of machining steps [26], [27]. A wide variety of AM technologies have been implemented. The American Society for Testing and Materials (ASTM F2792-12a) have listed over 50 different AM technologies classified into 7 different processes [27]. Since fuel cells and electrolysis technologies are based on complex systems consisting of multilayer electrochemical cells, coated interconnectors with flow channels and gas manifolds, 3D printing technologies can positively contribute from different perspectives. The integration of cutting-edge single-step fabrication methods such as 3D printing of ceramics is essential for overcoming the significant limitations and reliability issues associated with conventional manufacturing of SOECs, which requires an elevated number of steps also involving manual assembly and multiple joints [66]. Nonetheless, the topic of additive manufacturing of SOEC has been explored only during the last years, due to a lack of knowledge on 3D-printing for functional ceramics. In particular, 3D printing of functional ceramics for SOEC application has been obtained through stereolithography (SLA) [67], [68] and slurry-based technologies, such as inkjet printing and robocasting techniques[69], [70], [71].

1.6.1. Colloidal suspension stabilization for AM techniques

SLA and robocasting techniques are based on different methods for the realization of the 3D green body. Nevertheless, in both cases, ceramic materials are processed through the realization of highly loaded colloidal ceramic powder suspensions, also called pastes or ink in AM applications. The homogeneous dispersion of the ceramic powder inside the system and its rheological properties are of paramount importance for the realization of a green body and final 3D-printed structure [72], [73]. For this reason, the basic theoretical principles for obtaining a stable colloidal suspension are explained in the following paragraphs.

A colloidal suspension can be defined as a highly concentrated slurry of particles dispersed in a low-viscosity solvent (aqueous or organic) and, in reduced proportions, organic additives (dispersant and binder). The rheological behaviour of the paste is dominated by the inter-particle interactions, which, based on the DLVO theory, can be expressed as the combination of electrostatic and Van der Waals contributions [74].

The morphology and size distribution of the ceramic particles are fundamental properties to rationalize the results of the rheological characterization of the pastes which will be presented later in the manuscript. At rest, the particles are randomly dispersed throughout the liquid continuum phase under the action of Brownian motion, referable to thermal equilibrium at a given temperature. On the other hand, when shear stress in a certain direction is applied, the particles assume a more ordered arrangement in strings or layers along that preferential direction, making the movement past each other and leading to a reduction of the viscosity of the system. Inks realized by the dispersion of small particles are characterized by a larger effect of Brownian motion relative to the shearing effect of the applied shear rate. On the contrary, for large particle dispersions the relative effect of Brownian motion is smaller and the applied shear stress leads to a more relevant reduction of the viscosity [75]. The qualitative result of this observation is reported in **Figure 1.16**.

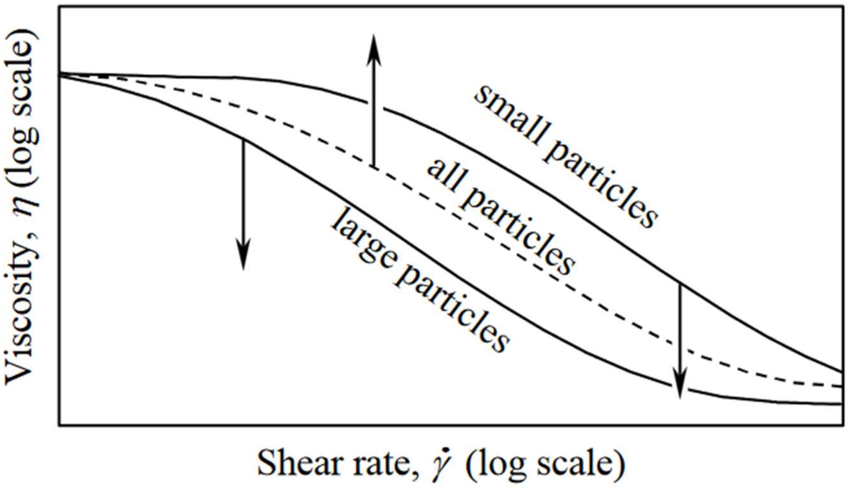

Figure 1.16 *Schematic diagram of viscosity as a function of shear rate and particle size for a shear-thinning colloidal suspension [75]*

A particular case of interest is represented by ceramic powders presenting a bi-modal particle sized distribution. In a bi-disperse suspension, the lubrication effect of small particles can lead to higher fluidity and, therefore, lower viscosity. The viscosity of a bimodal suspension has been demonstrated to have a minimum concerning the volume ratio of the two particle sizes, as shown in **Figure 1.17** [74].

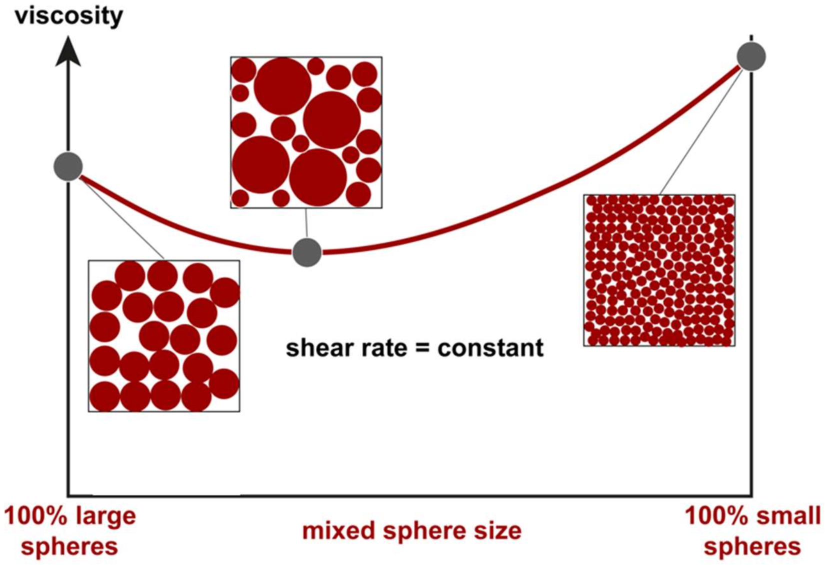

Figure 1.17 *Qualitative trend of viscosity for a polydisperse colloidal suspension at constant shear rate and solid loading [105]*

DLVO theory, and other possible formulations of the inter-particle interactions, constitute a starting point for the formulation of a stable suspension. Particularly, tuning the attractive-repulsive forces is a fundamental issue for adjusting the rheological properties of suspensions for 3D printing. Three main stabilization methods can be identified (see **Figure 1.18**) [74]:

- Electrostatic stabilisation, that is modifying the pH of the suspension to change the net charge on the particle's surface.
- Steric stabilisation, which consists of using specific dispersants (e.g. polymers) that bind to the particles covering the surface, generating a physical barrier.
- Electrosteric stabilization, which consists in a combination of electrostatic and steric stabilisations. The molecules used as dispersants are polyelectrolytes (e.g. polymers having a charged group) that bind to the surface and increase the repulsion with the addition of an electrostatic contribution to the steric mechanism.

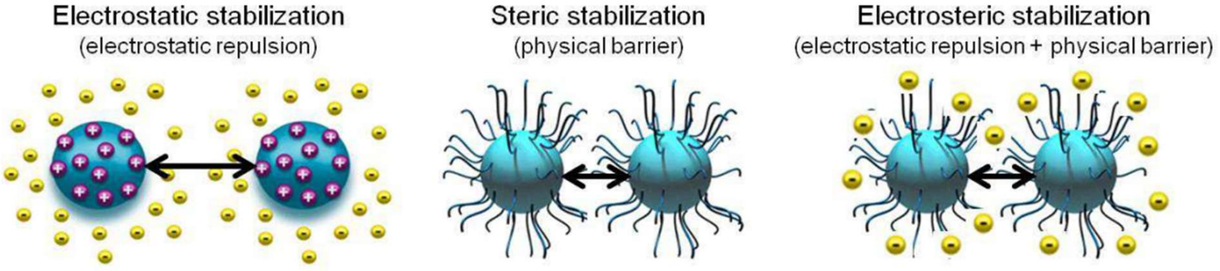

Figure 1.18 *Mechanisms for colloidal stabilisation [76]*

Another organic compound generally added to colloidal suspensions for AM is a binder. Binders are utilised to provide sufficient mechanical strength to the system such that the green bodies can retain the desired shape without breaking or damage, allowing the realisation of a self-standing structure.

Summarizing, by tailoring the solid loading and the inter-particles interactions, with the addition of binders and dispersants, is possible to adjust the rheological characteristics of a paste. Nevertheless, the main drawback of this approach is that these inks may be very sensitive to variations on the chemistry and pH of the environment, making them unstable and difficult to control.

1.6.2. Stereolithography

Stereolithography can be described as an additive fabrication process that uses a UV laser for the selective photopolymerization of a liquid UV-curable photopolymer to build layered structures[26]. The ceramic powder is dispersed in a liquid photopolymer, together with a photoinitiator, absorbing in the UV range of the source, and with other additives, as explained in the previous section [73], [77]. The SLA system is generally composed of a tank with uncured resin, a movable platform, a UV laser and a mirror system, as shown in **Figure 1.19**. From the operational point of view, a CAD design file is transferred to the SLA apparatus and the UV light is irradiated on the liquid resin following a specific pattern. Once the first layer is solidified, the platform moves downwards, and the subsequent layer is cured. The process continues until the desired three-dimensional structure is obtained. Then, the green body is removed from the apparatus, the excess resin is removed and then it is subjected to thermal processing to remove the organic fraction and to allow the densification of the system [26].

SLA techniques have been used to investigate the effect on performances of SOC components' geometrical modifications. Pesce et al. [78] and Marquez et al. [79] fabricated similar planar and corrugated electrolytes, using 8YSZ and Ytterbium-doped scandia-stabilized zirconia respectively, through SLA, observing a substantial increase in power density during SOFC operation, straightforwardly corresponding to the increase in the active area of the 3D printed corrugated electrolyte. Martos et. al [80] investigated a novel ultra-compact SOC stack concept operating in reversible mode and based on 3YSZ electrolyte-supported corrugated cells fabricated by 3D printing, proving the durability of the cell in mid-term operation (500h), enhanced power density and mechanical robustness with respect to conventional SOC technologies based on SoA materials.

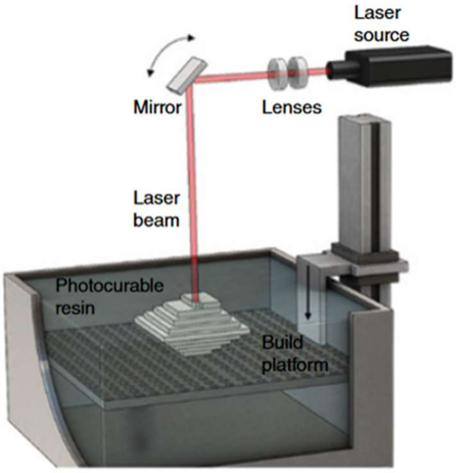

Figure 1.19 *Schematic representation of SLA process [26]*

1.6.3. Robocasting

Robocasting, also called Direct Ink Writing (DIW), is a freeform fabrication technique for dense ceramics and composites that is based on layer-wise deposition of highly loaded colloidal suspensions [81], [82]. This technique, thanks to its low-cost and simplicity concerning other AM devices, has been considered for the deposition of different typologies of ceramic materials, such as Al_2O_3, 3YSZ, carbide and nitride. Over the last few years, many efforts were made to combine robocasting and other 3D-printing techniques for the fabrication of SoA electrolytes and electrodes [71], [83]. As far as this thesis is concerned, Robocasting is considered for the deposition of the glass powder forming the GC sealing layer of the stack.

Robocasting is based on material extrusion through a nozzle by applying pressure to the paste, as represented in **Figure 1.20**. Based on the methodology of the pressure application, robocasting technologies can be divided into: screw driven, piston-driven and pneumatic dispensing [84].

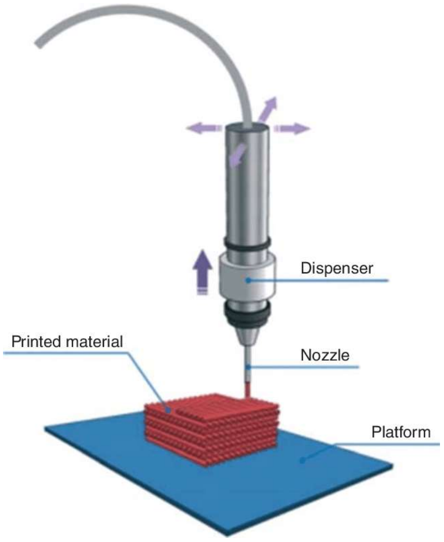

Figure 1.20 Schematic representation of the Robocasting process [85]

After deposition, the pastes should be able to support their weight during assembly, thanks to tailored composition and viscoelastic properties. Therefore, the ink's rheology is the most critical and complex aspect for the fabrication of the desired three-dimensional structure.
The characterization and processing of the ink consists of different steps and can be summarized as follows [72], [84]:

1. Characterization of the powder, i.e. particle morphology and particle size distribution
2. Ink formulation
3. Ink rheology, i.e. experimental and analytical analysis
4. Definition of the printing parameters
5. Definition of the post-printing processes

For the correct extrusion of the material, the paste should have a viscoelastic shear-thinning behaviour, characterized by the reduction of the viscosity when increasing the shear stress (**Figure 1.21**). On the other hand, if viscosity increases at increased shear rates (shear-thickening behaviour) extrusion is difficult, with possible jamming of the flow through the nozzle.

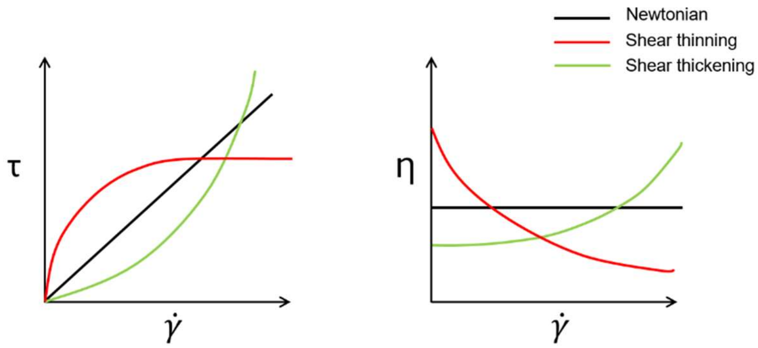

Figure 1.21 *Flow curves for a Newtonian (black), shear thinning (red) and shear thickening fluid (green). Shear stress vs shear rate plot (left), Viscosity vs shear rate plot (right) [86]*

The experimental results are then fitted with best fit models and compared with analytical models of the nozzle to predict the extrudability of the paste. The rheological behaviour of ceramic inks used in DIW generally does not follow Newtonian's law. DIW pastes' flow curve typically has a non-linear trend, which can be well fitted by the Herschel–Bulkley model, as expressed in Equation 1.8.

$$\tau = \tau_y^H + k\dot{\gamma}^n \tag{1.8}$$

Where τ is the stress [Pa], τ_y^H is the Herschel-Bulkley yield stress [Pa], $\dot{\gamma}$ is the shear rate $[s^{-1}]$, k is the consistency index $[Pa \cdot s^n]$ and n is the power law index [74], [75], [87]. If $n \ll 1$, a shear thinning fluid is described, while $n > 1$ describes shear thickening. Other models that can be applied for the fitting of the experimental data in the case of DIW inks are the Carreau and Cross models [72].

In the solidification step, the ink must exhibit a transition from a liquid-like to a solid-like state to retain its shape right after deposition. A viscoelastic material can be described using a generalization of Hook's law, introducing the so-called complex viscosity η^* and the complex modulus G^*, as reported in Equation 1.9:

$$\sigma = \eta^*\dot{\gamma} = G^*\gamma = (G' + iG'')\gamma \tag{1.9}$$

Where γ is the strain of the material. The complex modulus can be decomposed in two component: G', the storage modulus, and G'' the loss modulus. The storage modulus describes the elastic component of the stress, whereas the loss modulus describes the viscous part. The low-stress region in which the storage modulus remains constant with the stress is the linear viscoelastic region (LVR). When the storage modulus starts decreasing, the material is in its non-linear region. The intersection of G' and G'' corresponds to the yield point, where the material starts having a completely viscous behaviour with a transition from solid to liquid. Nevertheless, the elastic-to-viscous transition occurs in a range of stresses, called yielding-interval [86]. The typical trend of storage and loss modulus for a viscoelastic fluid is reported in **Figure 1.22**. Another important parameter is the time needed for the solid-to-liquid transition.

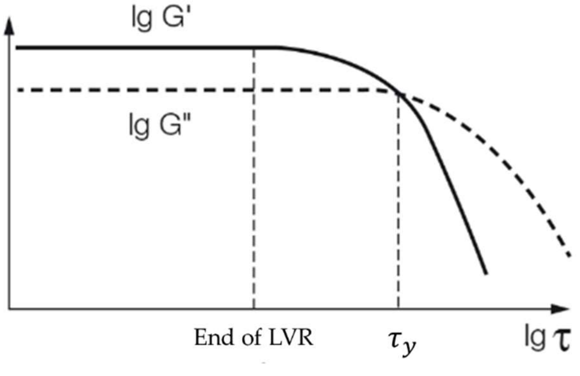

Figure 1.22 *Shear moduli vs shear stress for a viscoelastic material [88]*

The experimental results are then combined with analytical models to predict the spreading of the ink. In addition, the printing parameters should be adjusted so that the stress in the nozzle is higher than the yield stress of the material, to allow a correct extrusion.

As far as the layer support steps are concerned, the rheological parameters obtained from experiments related to the extrusion and solidification steps are combined with analytical models to predict the self-sustaining capacity of the structure. The majority of the models focus on determining the maximum height of the printed part from a yield stress ink after which failure occurs.

The green part obtained from Robocasting/DIW technology has to be subjected to additional processes of burning out of the organic part and sintering to increase the density and reduce the porosity of the final 3D-printed object.

1.7. Scope of the thesis

This thesis is focused on the study, evaluation and optimisation of glasses for use as sealants in SOEC applications, with an operative temperature of 850 °C and an operative pressure of 5 bar. High-temperature solid oxide electrolysis cells are by far the most efficient electrolysis systems, and their development can constitute a breakthrough in green hydrogen production and energy storage from renewables. This work is developed in the frame of the Horizon Europe project's HYP3D (Grant Agreement No. 101101274), focused on developing advanced SOEC technology by using 3D printing of ceramic materials to enable high-pressure hydrogen production. More specifically, the project aims at the realization of an ultra-compact configuration by acting on the geometrical modification of standard component shapes to obtain a large active area. Pressurized operation of SOEC can provide benefits both on cell, improving overall conversion efficiency, and system level, as for many industrial applications hydrogen has to be compressed before being used or stored. Currently, SOEC stacks are being studied and used under pressurized operation in big vessels to ensure the absence of a gradient of pressure between the inner and outer parts of the system. However, the stability of the device in an environment in which a gradient of pressure is present is yet to be assessed. The operation at high gas pressure requires the use of reliable sealing technologies at the metallic interconnect interface. Consequently, joint design, sealing material processing and optimisation, and surface tailoring of components to be joined are critical issues for a reliable and extended operation of the system.

In this work, three commercial glasses are characterised and the composition of one of the base glass systems is optimized by the addition of 3YSZ, following a composite approach. The thermochemical and thermomechanical compatibility of the sintered and crystallized glass-ceramic systems with the electrolyte and interconnector materials is evaluated in static air through the realization of joined samples. Surface modification of the interconnector material by laser machining is investigated to assess a possible improvement in wettability and mechanical resistance of the joined system thanks to enhanced interlocking between the materials. The mechanical resistance of the joined substrates is assessed in shear mode through single-lap offset tests. Finally, the rheological properties of glass powder loaded pastes are assessed, since the future steps involve the joining of 3D-printed YSZ to Crofer22APU with glass sealant deposition by Robocasting.

2. MATERIALS AND EXPERIMENTAL METHODS

The experimental activity focuses on the characterization of glass and glass-ceramic systems and their compatibility with SoA materials for interconnector, Crofer22 APU, and electrolyte, 3mol.% Yttria-Stabilized Zirconia. Thermal, thermomechanical, XRD and EDS analysis are performed to assess the variation of the behaviour of the glass and glass-ceramic systems with temperature, and to identify the characteristic phases formed during crystallization. Moreover, since the final objective is the automized deposition of the glass powder paste through the robocasting technique, the rheological properties of glass powder loaded pastes are analysed. Finally, the mechanical properties of the joined system, Crofer22APU/sealant/3YSZ are evaluated through mechanical tests.

2.1. Materials

2.1.1. Glasses

In this work, three commercial glasses are characterized as candidates to be used as a glass-ceramic sealant in the SOEC application at an operating temperature of 850 °C and at an operating pressure of 5 bar:

- MO-SCI 1862
- MO-SCI 1729
- SCHOTT G018-392

The compositions are reported in **Table 2.1** [89], [90], [91]. It can be observed that two of them are barium-based glasses, MO-SCI 1862 and Schott G018-392, whereas MO-SCI 1729 is a strontium-based glass.

***Table 2.1** Commercial glasses composition from company datasheets [89], [90], [91]*

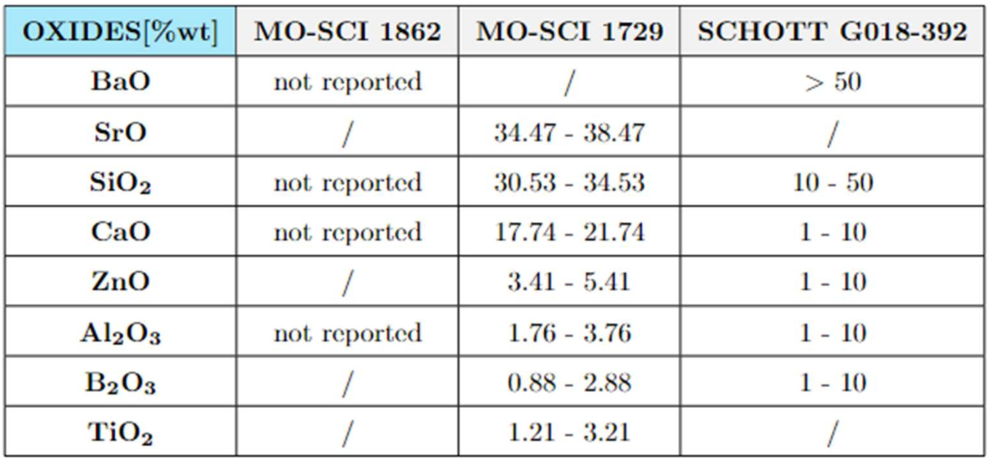

OXIDES[%wt]	MO-SCI 1862	MO-SCI 1729	SCHOTT G018-392
BaO	not reported	/	> 50
SrO	/	34.47 - 38.47	/
SiO_2	not reported	30.53 - 34.53	10 - 50
CaO	not reported	17.74 - 21.74	1 - 10
ZnO	/	3.41 - 5.41	1 - 10
Al_2O_3	not reported	1.76 - 3.76	1 - 10
B_2O_3	/	0.88 - 2.88	1 - 10
TiO_2	/	1.21 - 3.21	/

For the first characterization of the corresponding glass ceramics, the recommended thermal treatments reported in the commercial datasheets are used (see **Table 2.2**).

Table 2.2 *Recommended thermal treatments from datasheets [89], [90], [91]*

Commercial Glass	Recommended thermal treatment
MO-SCI 1862	900 °C for 1 hour ↑ 5°C ↓ 3 °C
MO-SCI 1729	850 °C for 2 hours ↑ 5°C ↓ 3 °C
SCHOTT G018-392	850 °C for 30 minuts ↑ 5°C ↓ 3 °C

2.1.2. Crofer22 APU and Laser modifications

Two types of Crofer22 APU with different geometrical characteristics are used depending on the test. The Crofer22APU/sealant/3YSZ joined samples observed at the SEM are realized using square metal substrates of approximately 1cm x 1cm having a thickness of 0.5 mm. On the other hand, the joints for mechanical tests are realized with Crofer22 APU parallelepipeds (12.5 x 25 x 2.5) mm.

The Crofer22 APU substrates' surfaces are laser modified to increase the roughness of the surface and observe possible improvements in adhesion and strength of the interface between the interconnector and the glass-based sealing, increasing the mechanical properties of the joined system. A higher roughness should increase the contact area, enabling to exploitation of the mechanical interlocking effect in a glass-to-metal joint, thanks to sealant infiltration in interconnector crevices. In the project, an Infrared Nanosecond fibre laser is used to modify the Crofer22APU surface. The parameters for the laser modification, named "C1", are listed in the following table (**Table 2.3**).

Table 2.3 *Parameters for laser modification of Crofer22 APU*

Modification	Power [W]	Rep. Rate [kHz]	Scan speed [mm/s]	Scan spacing [μm]	Pulse width [ns]
C1	20	20	15	60	12

Where the repetition rate is the frequency with which the laser pulses are emitted, the scan speed defines how fast the laser scans the sample surface, the scan spacing defines the distance between each laser line scan in both directions, and the pulse width defines the duration of each laser pulse. A schematic representation of the configuration of the laser scan is presented in **Figure 2.1**.

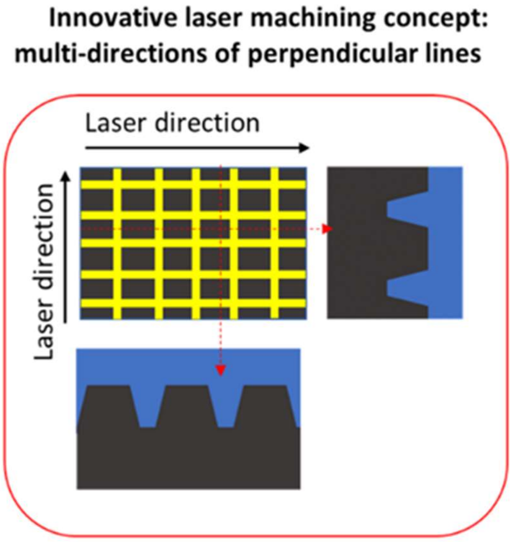

Figure 2.1 *Schematic representation of the laser scan path on the metallic substrate*

2.1.3. 3YSZ

As for the Crofer22 APU, different types of 3YSZ are used depending on the scope of the test. The first preliminary tests are realized using a very thin layer of 3YSZ obtained through tape casting. Successively, a more realistic study using the actual 3D-Printed cells produced by IREC is performed. Only small squares, of the same size as the Crofer22 APU, of this 3D-printed 3YSZ are obtained using a cutting machine. For the mechanical tests, 3D-printed parallelepipeds produced by 3DCERAM of dimensions (12.5 x 25 x 2.5) are used.

When used in pastes, 3YSZ is dispersed as fine powder having an average particle size of 0.7 µm and furnished by 3DCERAM.

2.2. Surface characterization: profilometry

The surface roughness of the substrates is evaluated by means of a stylus profilometer (Form Talysurf Intratouch, Taylor Hobson, USA) reported in **Figure 2.2**.

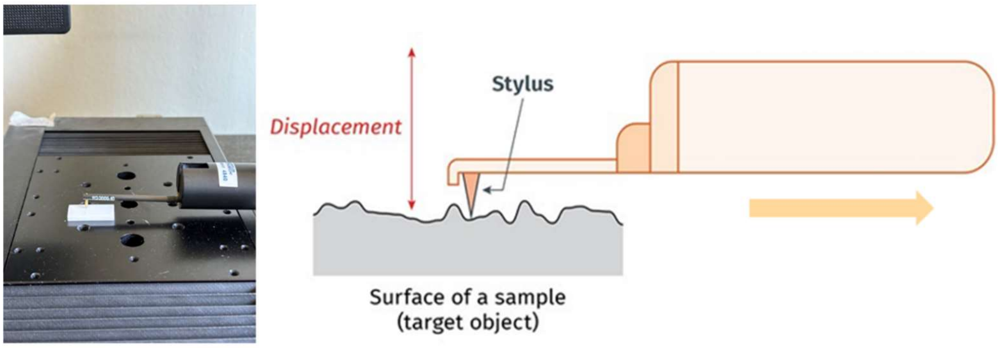

Figure 2.2 Profilometer plate and stylus (left picture) and schematic representation of the working principle (right image) [92]

The sensor can detect variations in surface roughness of the order of tens of nanometres. The height position of the diamond stylus is converted into a digital signal, stored, analysed and displayed. The stylus can move horizontally over the surface to generate a bidimensional measure. Nevertheless, it is also possible to obtain a 3D-surface thanks to the movement of the plate which supports the analysed sample. The plate moves perpendicularly to the stylus, allowing the construction of a three dimensional surface collecting multiple roughness profiles at different positions of the plate. An example of a generated 3D-surface is shown in **Figure 2.3**.

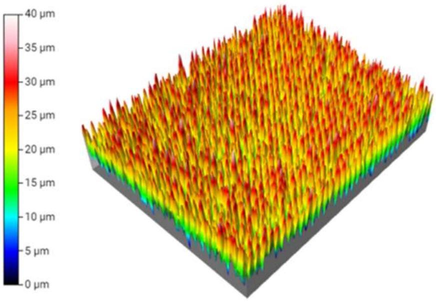

Figure 2.3 Example of a 3D-surface that can be generated through the data analysis of the performed profilometric measurements

Surface roughness parameters are generally categorized into three groups according to its functionality: amplitude, spacing and hybrid parameters [93], [94]. Due to the complexity of surface geometry, 59 parameters can be defined and can be chosen basing on the specific conducted analysis. In this work, only two parameters are considered basing on the existing bibliography [63], [95]. In particular, the arithmetic average height S_a and maximum peak to valley height S_z parameters are reported from the data analysis. The arithmetic average height is the most used parameter for the first roughness assessment of the surface. It is easy to define, easy to measure, and gives a good general description of height variations. Nevertheless, it is not very sensitive to small variations in height of the profile. From the mathematical point of view, it is defined as follows:

$$R_a = \frac{1}{l}\int_0^l |y(x)|\,dx \tag{2.2}$$

The other parameter, S_z, is defined as the vertical distance between the highest peak and the lowest valley ($S_z = S_{v4} + S_{p3}$ from the example of **Figure 2.4**) along the assessment length of the profile [94].

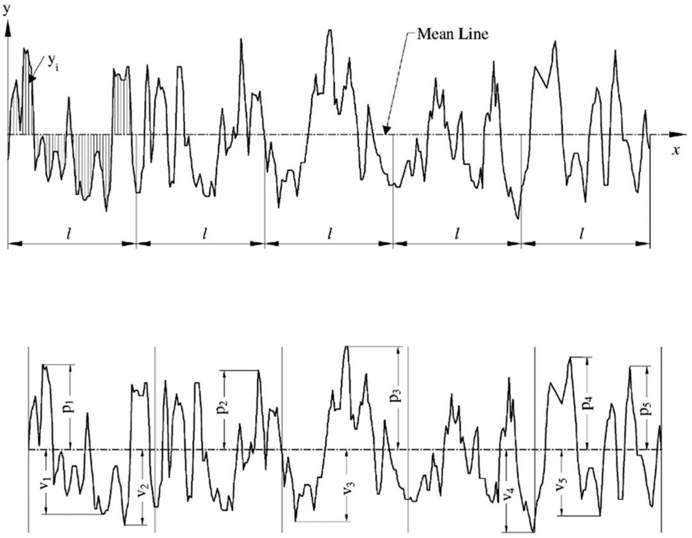

Figure 2.4 *Generic 2D profilometric profile [94].*

In this thesis, the profilometer is used for the evaluation of the surface roughness of 3YSZ and Crofer22 APU substrates, with and without laser modification.

2.3. Glass and glass-ceramic sealant characterization

2.3.1. Thermal and thermo-mechanical analysis

2.3.1.1. Differential Scanning Calorimetry

Differential Scanning Calorimetry (DSC) is a thermo-analytical technique used to measure the heat flow associated with phase transition of a material. A sample and an inert reference are heated (or cooled) with a programmed temperature ramp in a controlled atmosphere. The phase transitions can be identified in the DSC curves, which represent the heat flux as function of the temperature or the time, as positive and negative peaks. Positive peaks identify exothermic processes, such as crystallization, whereas negative peaks identify endothermic processes, such as melting. By observing variations in the DSC curves' slope and peaks presence, it is possible to identify some important glass characteristic temperatures:

- Glass transition temperature T_g, which is the temperature at which the amorphous glass passes from a hard and brittle state to a viscous state.
- Onset temperature of crystallization Tc_{on}, temperature at which the crystallization process starts.
- Glass crystallization temperature T_c, which is the temperature at which the crystallization rate is maximum.
- Melting temperature T_m, the temperature at which the glass passes to liquid state.

The instrument used to perform the analysis, reported in ***Figure*** **2.5**, is the DSC 404 F3 Pegasus (Netzsch-Gerätebau GmbH, Selb, Germany).

.

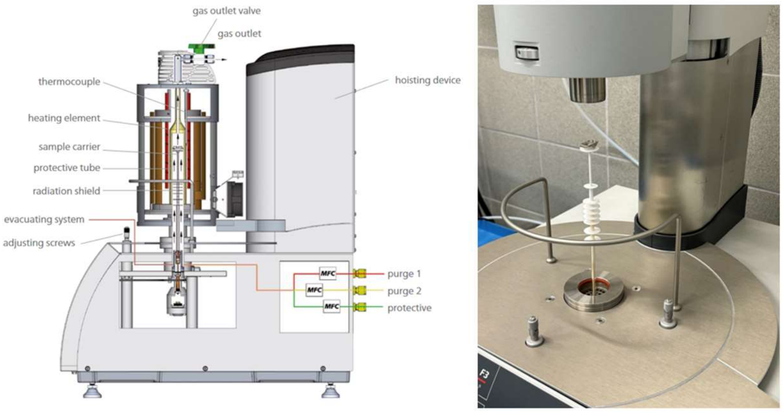

Figure 2.5 *Sketch and picture of the actual DSC 404 F3 Pegasus used for the measurements [97]*

In order to perform the analysis, approximately 50 mg of glass powder are put in a platinum-iridium crucible, while the inert reference is an empty platinum-iridium crucible. The measurements are performed in static air with an argon flux as protective gas. The chosen heating rate is 5 °C/min, from ambient temperature to 1200 °C, coherently with glasses thermal treatments for the joining process.

2.3.1.2. *Hot Stage Microscopy*

Hot Stage Microscopy (HSM) is a technique which combines optical and thermal analysis. The sample is heated at a specified heating rate in a tubular alumina furnace and its morphological evolution is observed through a camera, as schematized in **Figure 2.6**.

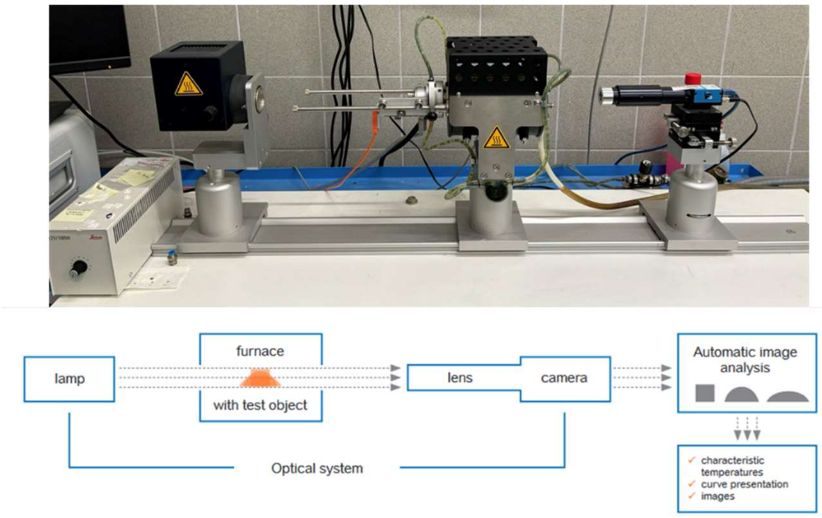

Figure 2.6 *Picture and scheme of the working principle of HSM [97]*

In the analysis performed by HSM, the images are recorded during the heating ramp and the evolution of the cylindrical sample's shape can be observed. Basing on geometrical considerations, the HSM software identifies certain characteristics temperatures [96], [74]:

- First Sintering Temperature (T_{FS})it is the temperature at which the system starts shrinking. This step generally starts approximately 50 °C above the glass transition temperature.
- Maximum Shrinkage Temperature (T_{MS})the temperature at which the maximum densification of the powders occurs before the glass begins to soften.
- Deformation Temperature (T_D)the temperature at which a material begins to deform under the influence of heat. At this temperature, the material shows noticeable changes in its shape or structure, such as samples' corners rounding.
- Sphere Temperature (T_S)the temperature at which the hight/width ratio is equal to one.
- Half-Sphere Temperature (T_{HS}) the temperature at which the hight/width ratio is equal to 0.5.
- Flow Temperature (T_F), temperature at which the height of the sample is equal to 1/3 the hemisphere height.

Moreover, it is possible to assign distinct glass viscosities to these fixed points in order to evaluate temperature-viscosity curves as shown in **Figure 2.7** [11], [98], [99], [100].

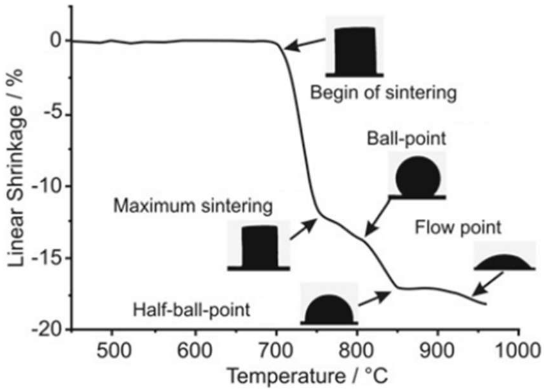

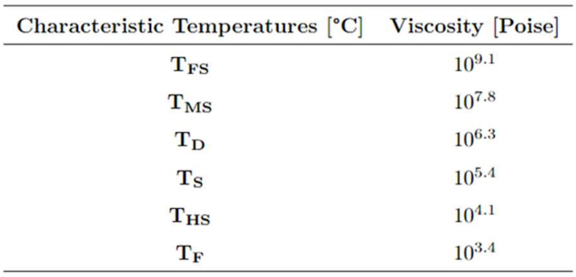

Characteristic Temperatures [°C]	Viscosity [Poise]
T_{FS}	$10^{9.1}$
T_{MS}	$10^{7.8}$
T_D	$10^{6.3}$
T_S	$10^{5.4}$
T_{HS}	$10^{4.1}$
T_F	$10^{3.4}$

Figure 2.7 *Generic HSM curve and fixed viscosity points [11]*

These fixed viscosity points are generally fitted using the Vogel–Fulcher–Tammann equation to obtain viscosity-temperature curves. The VFT equation in logarithmic form is expressed in Equation 2.1.

$$\log \eta = A + \frac{B}{T - T_0} \tag{2.1}$$

Where A, B and T_0 are the fitting parameters [96].

2.3.1.3. Dilatometry

Dilatometry (DIL) is a thermo-mechanical analysis where a specimen is heated with a programmed temperature ramp in a controlled environment. Variations in length are measured by an extensometer at the end of a pushrod linking the sample; in particular the displacement of the extensometer determines an output voltage variation proportional to the sample elongation. Through the comparison of these length changes with the initial length, it is possible to evaluate the thermal strain over a certain temperature range, enabling the determination of the Coefficient of Thermal Expansion.

The measurements are performed on 5 mm width pellets, obtained from mechanically pressed glass powders and subsequently subjected to the same thermal treatment of the joined samples. Therefore, the results refer to the glass-ceramic material, presenting a crystalline and a glassy phase.

In addition to the CTE, the instrument allows the evaluation of the glass transition temperature (T_g) and softening temperature (T_s) of the glass-ceramic.

The device used in this work is the DIL 402 Expedis Classic (Netzsch-Gerätebau GmbH, Selb, Germany)., sketched and reported in **Figure 2.8**.

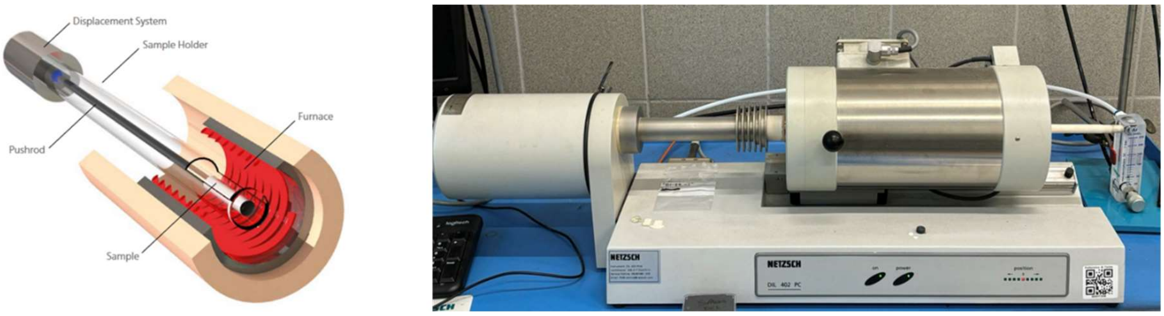

Figure 2.8 *Sketch and picture of the dilatometer DIL 402 Expedis Classic [101]*

2.3.2. X-ray diffraction analysis

X-Ray Diffraction analysis is used for the determination of the crystalline phases produced during the crystallization process of the glass systems. It is performed using an X'Pert Pro MRD diffractometer, with Cu Kα radiation (PANalytical X'Pert Pro, Philips, Almelo, The Netherlands), and with the aid of X-Pert HighScore software, while the phases are identified using the JCPDS database provided by PDF-2 ICDD (International Centre for Diffraction Data, Newton Square, Pennsylvania, the USA).

The instrument consists of three principal devices: an X-ray source, a sample holder and a XRD detector. X-ray beams are chosen because their wavelength is similar to the spacing between atoms in the sample, so the angle of diffraction will be affected by the spacing of the atoms in the molecule. Basically, the atomic planes of the crystals cause the incident X-Rays beam to scatter and interfere with each other, leaving the sample at a certain angle ϑ different from the initial one. The scattered X-Rays are collected by the XRD detector generating a certain diffraction pattern. The obtained diffraction pattern is then compared with the reference pattern for specific phases in order to determine the most probable phases which appear in the sample. In this work, XRD analysis is applied on powder obtained from thermally treated pellets of glass-ceramic materials.

2.4. Robocasting paste formulation

2.4.1. Glass powder characterization

In order to characterize the glass powders from the morphological point of view and to derive the particle size distribution, pictures realized with Field Emission Scanning Electron Microscopy (FESEM; SupraTM 40, Zeiss, Oberko-chen, Germany) are combined with image analysis using ImageJ software. The particle size distribution determination is needed to investigate the influence of powders dimensions on pastes' rheology as discussed in Section 1.6.1.

A brief explanation of FESEM working principle is given. Scanning electron microscopes produce images by means of a beam of electrons, generated by an electron gun, focused on the surface of the sample. These electrons interacts with the atoms of the material generating different responses. The electrons can be scattered from the sample, or they can induce the emission of secondary electrons. The first type are the back scattered electrons, and they give information about the sample composition, topography, mass thickness, and crystallography. Electrons of the second type are called secondary electrons and give information about the sample topography.

For the analysis of the glass powders images, the analysis is done in secondary mode (SED) and analysed with ImageJ by considering the longest side of approximately 250 particles for each glass powder.

2.4.2. Formulation and Rheological characterization of the paste

As reported in Section 1.6.3, the deposition of glass powders by Robocasting technique requires the realization of a highly loaded colloidal suspension, called paste, having strict viscoelastic properties. For the preparation of the pastes, one organic solvent and two organic additives are used. In particular propylene glycol (PG) is used as solvent, Polyvinylpyrrolidone (PVP) K30 as dispersant and Polyvinylpyrrolidone K90 as binder.

The pastes are formulated with a solid loading of 75wt% and a liquid loading of 25wt%. In particular the dispersant (PVPK30) corresponds to the 1wt% of the solid loading and the binder corresponds to the 1wt% of the liquid loading. The organic additives are previously mixed at 5% in weight with PG in two different containers in order to obtain a homogeneous mixture. Subsequently, the PG-PVPK30 and PG-PVPK90 mixtures are added along with PG in a falcon container and mixed, using a mechanical stirrer (**Figure 2.9**), for 10 minutes at 400 rpm.

***Figure 2.9** Mechanical stirrer for the mixing of the pastes*

The solid loading is represented by glass powder or glass powder with the addition of 3YSZ powder. The powders are added and stirred in different steps in order to avoid excessive agglomeration and to allow their correct dispersion in the suspension. Particularly, the powders are added in 4 different steps and mixed at 400 rpm for 10 minutes during each step. Finally, a mixing step of 20 minutes at 500 rpm is performed. The stirring intensity of 400 rpm is chosen for SCHOTT G018-392, whereas for MOSCI 1862 and MOSCI 1729, a rotational velocity of 600 rpm is used, due to difficulties in obtaining a homogeneous mixture without agglomerations.

The composition for 10g of paste is reported in the following table (**Table 2.4**):

***Table 2.4** Paste recipe for 10g with a solid loading of the 75wt.%*

PASTE RECIPE	
SOLID LOADING (glass powder + 3YSZ)	7,5g
LIQUID LOADING (solvent + additives)	2.5g
PVPK30 + PG	1.5g
PVPK90 + PG	0.5g
PG	0.5g

The solid loading is limited to 75wt.%, due to the stirring efficiency of the mechanical stirrer. However, using a planetary mixer (THINKY ARE-250; THINKY Laguna Hills, California) (see

Figure 2.10), it is possible to increase the solid loading to the 80wt.% with a reduction of the mixing time per step thanks to the higher stirring velocity.

Figure 2.10 Picture of the THINKY ARE-250 planetary mixer

Specifically, for the realization of SCHOTT G018-392 and SCHOTT G018-392+3YSZ pastes, the powders are added in four different steps and mixed for 5 minutes at 1000 rpm, with a final defoaming step of 5 minutes at 1200 rpm, followed by a mixing step of 1 minutes at 1000 rpm. The composition of 10g of paste at a solid loading of the 80wt.% is reported in **Table 2.5**.

Table 2.5 Paste recipe for 10g with a solid loading of the 80wt.%

PASTE RECIPE	
SOLID LOADING (glass powder + 3YSZ)	8.0g
LIQUID LOADING (solvent + additives)	2.0g
PVPK30 + PG	1.6g
PVPK90 + PG	0.4g
PG	0.0g

The rheological characterization of the pastes is performed with a Controlled Stress Single Head Rotational Rheometer (DHR-2, TA Instruments, Waters, USA), reported in **Figure 2.11**.

Figure 2.11 *Rotational Rheometer DHR-2, TA Instruments, Waters, USA [96]*

Specifically, this type of rheometer is characterized by a flat plate geometry. The paste is deposited on the static plate by means of a spatula and the moving head is slowly lowered in order to obtain a correctly filled configuration, as shown in **Figure 2.12**.

Figure 2.12 *Measurement setup of the rotational rheometer head*

The rheometer allows the evaluation of viscosity and viscoelastic properties (G' and G'') through the relation between constitutive equations of the material and device's parameters (i.e. applied torque, angular displacement and angular velocity of the plate). In particular, three types of test are performed on the pastes: Steady-Shear Flow Sweep Test, Oscillatory Amplitude Sweeps test and Three Interval Thixotropy Test (TITT).

In the Steady-Shear Flow Sweep Test, the shear rate is increasingly varied in the range 0.01 – 500 s^{-1} and the corresponding values of viscosity and shear stress are collected. This type of test is used to simulate the behaviour of the paste during the extrusion process. In the oscillatory amplitude sweep test, the storage and loss moduli are measured versus an increasing oscillatory amplitude at constant frequency, as reported in **Figure 2.13**.

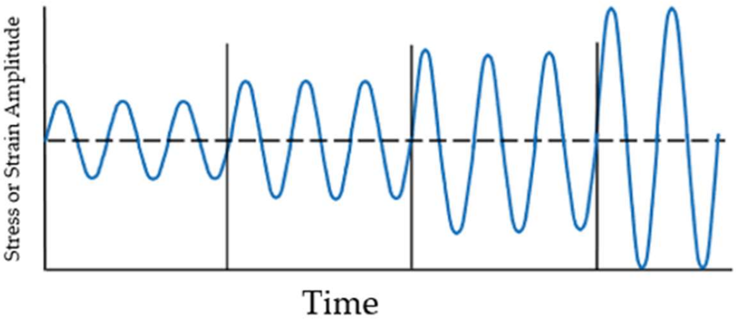

Figure 2.13 Example of Stress (Strain) Amplitude vs Time for Oscillatory Amplitude Test [102]

The Three Interval Thixotropy Test, or oscillatory strain step-change, is used to evaluate the time needed for the liquid-solid transition of the paste and the percentage recovery of the original viscosity value. In detail, using the results of the oscillatory amplitude sweep, two shear rate values below and above the critical yield value are applied for a certain amount of time to the paste and the corresponding values of viscosity are collected. In this work, a low shear rate of 10 s^{-1} and a high shear rate of 200 s^{-1} are applied for 30 seconds each and the relaxation time and viscosity are evaluated.

2.4.3. Robocasting

Pastes deposition is performed using the ZMorphVX (Zmorph S.A., Wroclaw, Poland) multitool 3D printer equipped with a thick paste extruder toolhead (see **Figure 2.14 (a)**). A screw piston, driven by a stepper motor, is inserted into a 5 ml syringe where the paste is subsequently loaded (see **Figure 2.14 (b)**) . The desired shape is deposited by uploading in the 3D printer memory a CAD model which can be selected before the setup of the system. Precisely, the CAD model is generated through Zmorph S.A.'s software Voxalizer and uploaded as a .gcode file.

In this work, the Robocasting 3D printer is used for the deposition of a glass/ceramic powder loaded paste on a 3YSZ substrate for the realization of a Crofer22APU/sealant/3YSZ joint.

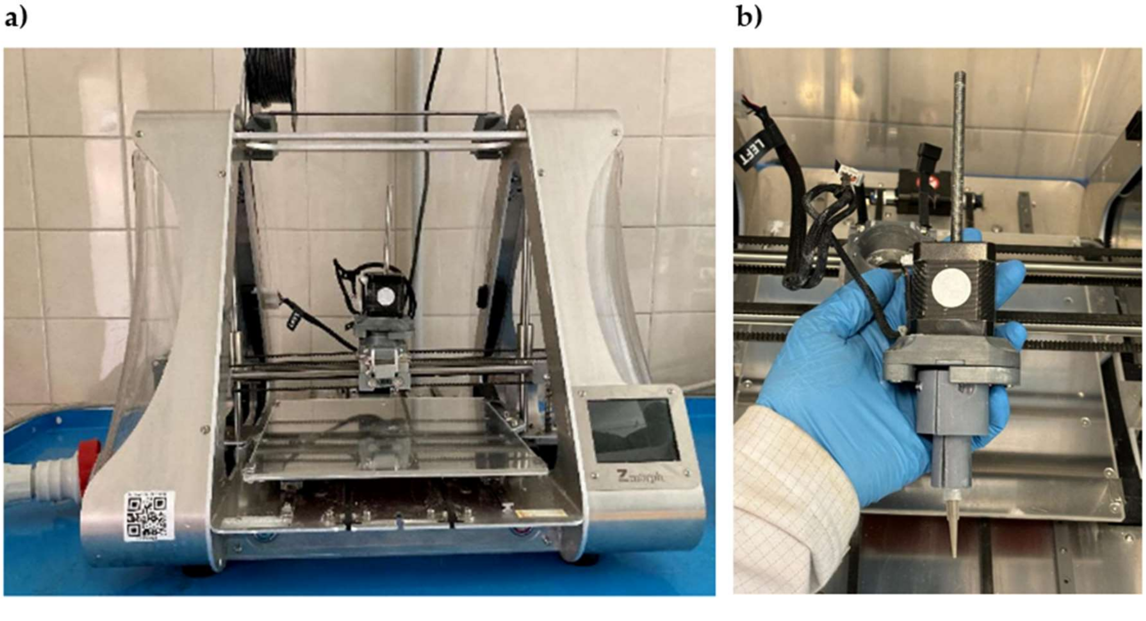

***Figure 2.14** a) ZMorphVX 3D printer; b) Thick paste extruder toolhead*

2.5. Joining, morphology and mechanical tests

Joined samples are realized between 3YSZ (electrolyte material) and Crofer22 APU (interconnect material) using the three commercial glasses MO-SCI 1862 (Ba-based), MO-SCI 1729 (Sr-based) and SCHOTT G018-392 (Ba-based). Subsequently, scanning electron microscopy is performed in order to assess the compatibility of the dissimilar joints. In order to have a better understanding of the microstructural composition of the analysed materials, Energy Dispersive X-Ray Spectroscopy (EDS) is performed and coupled with XRD analysis. EDS is a technique for the elemental and chemical characterization of a sample. The working principle is based on the collision of electrons with the material and the subsequent emission of X-Rays. The EDS analysis can be used to determine the elemental composition of individual points or to map out the distribution of elements from the imaged area. EDS is performed on joints in order to better identify elements present in the glass-ceramic sealant. EDS is integrated in the JCM-6000Plus Benchtop Scanning Electron Microscope (JEOL, Tokyo, Japan), used also for the SEM analysis of the joined samples Crofer22APU/sealant/3YSZ.

The samples are assembled in two different configurations, as shown in **Figure 2.15**:

- (a) sandwich-like structure for morphology characterisation
- (b) misaligned joints for shear strength mechanical test (single lap offset, SLO)

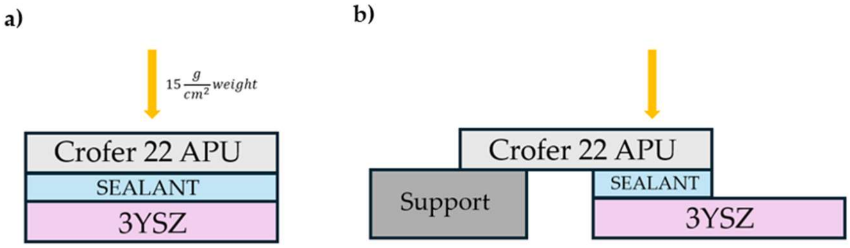

Figure 2.15 *Schematization of joints preparation for SEM observation and mechanical testing: a) for cross-section observation; b) for shear strength mechanical test*

Preliminary tests are done depositing glass powders on substrates as a slurry. The slurry is done mixing glass powder (70 vol%) with ethanol (30 vol%). The substrates are previously polished by putting them in an ultrasonic cleaner for ten minutes inside a beaker containing ethanol and acetone. Subsequently the slurry is deposited on the 3YSZ substrate using a spatula. Finally, the Crofer22 APU is positioned on top of the slurry in order to process a sandwich-like structure, as schematized in figure **Figure 2.15 (a)**. The same process is followed in the case of joints realized with pastes. In the case of the pastes with a solid loading of 75wt.%, after the deposition, the substrates are dried in oven at 90 °C for thirty minutes in order to avoid the spillage of the paste after the positioning of the Crofer22 APU. Moreover, in order to facilitate the joining process, a weight of 15 g/cm^2 (considering the joined area only) is placed on the upper layer of the joint. On the other hand, thanks to the improved rheological properties of pastes with a solid loading of the 80% (discussed in Section 3.2.2.2), it is possible to place the Crofer22APU layer before the drying step in oven. Finally, the weight are added after the drying of the sandwich-like structure. Successively, the samples are thermally treated in furnace (LHT418PN2, Nabertherm GmbH, Lilienthal/Bremen, Germany) as reported in **Table 2.2**. For MO-SCI 1862 and MO-SCI 1729 also other joining attempts at higher temperature, respectively 950 and 900 °C, are done basing on experimental results.

The sandwich-like Crofer22APU/sealant/3YSZ joints are analysed at the SEM, where also EDS is performed. For this purpose, the samples are previously polished with sandpaper 120 to sandpaper 4000 and coated with platinum.

For the realization of the SLO mechanical test samples, an aluminium oxide support under the upper layer is placed to obtain a parallel configuration, as shown in **Figure 2.15 (b)**. The rest of the procedure followed for the realization of the joints is the same previously discussed for the sandwich-like structure joints. In this work, the SLO test at room temperature is used for the evaluation of the shear mechanical properties of Crofer22APU/sealant/3YSZ joints. The experimental setup for the test is shown in **Figure 2.16**. The SLO in compression test is adapted from the standard ASTM D905-08. This configuration is designed to minimize the bending and rotation of the joined system, to obtain a parallel displacement between the joined substrates, which generates pure shear [103].

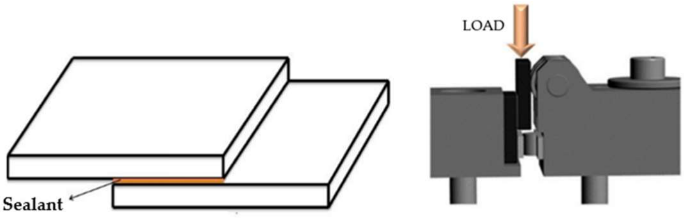

Figure 2.16 *Experimental setup for Single Lap Offset Test [103]*

The top-view and cross section of the broken substrates are then analysed to observe the fracture nature, adhesive or cohesive, and the joining area is calculated, using a digital calibre, for the evaluation of the shear stress. The compressive shear strength in [Mpa] is calculated dividing the applied load [N] by the joining area [mm^2]

Based on the experimental results, SCHOTT G018-392+10wt%3YSZ composite system is selected to continue the experimental campaign with a pressurized test to evaluate the resistance of the joined structure under a pressure gradient of 5 bar at room temperature. This choice will be addressed in the following sections. The as-joined structure is schematized in **Figure 2.17**.

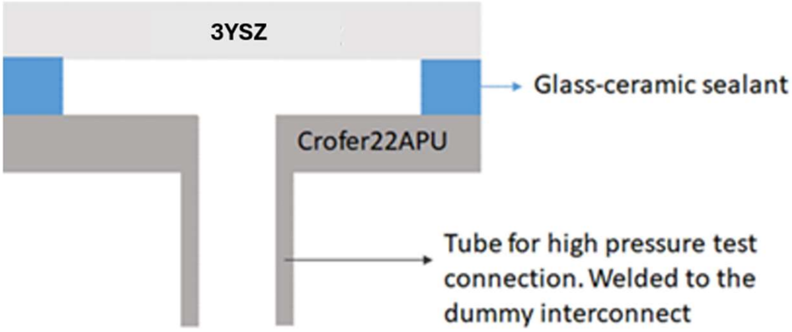

Figure 2.17 *Ideal vertical cross section of the experimental setup for pressurized test of the Crofer22APU/sealant/3YSZ*

The 3YSZ used for this test is a 44x44 mm 3D printed square, while the Crofer22 APU is a 50x50 mm square with a tube in the rear part, as schematized in **Figure 2.17**, where air would flow during the pressurized test.

The joint is realized through Robocasting deposition of SCHOTT G018-392+10wt%3YSZ powder loaded paste on the 3YSZ substrate, followed by its positioning on the Crofer22APU layer, drying in oven and thermal treatment for the joining process in furnace (MANFREDI™ 1100; Manfredi+Reddish Stone, Pinerolo, Torino, Italia). For the realization of this joint, an alumina weight of 215g is put on the 3YSZ layer.
The deposited geometry is a 36x36 mm square realized through Voxalizer software and imported in the Robocasting 3D printer. The geometry is shown in **Figure 2.18**. The reason of the addition of a line before the desired square will be addressed in Section 3.4.

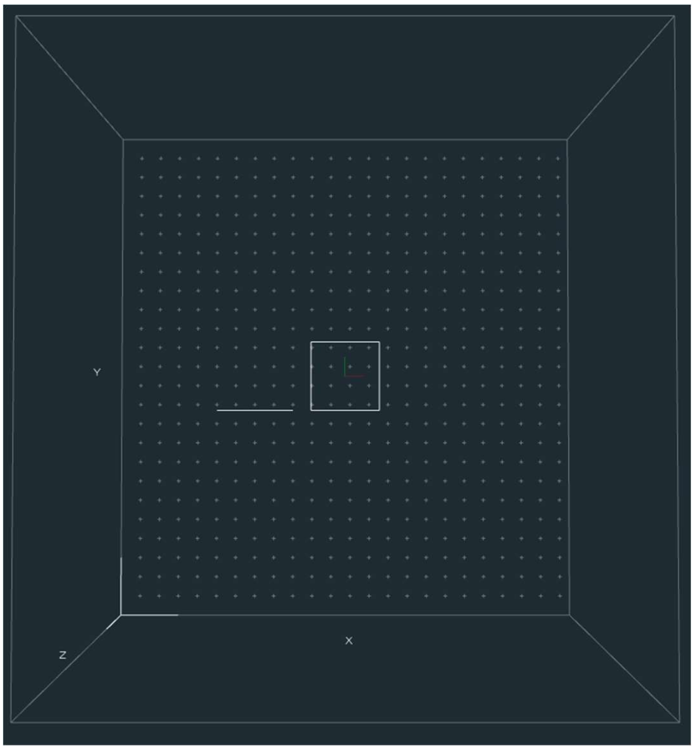

Figure 2.18 Geometry generated for the final Robocasting deposition trial through Voxalizer graphic interface with the addition of a simple geometry (line) before the extrusion of the actual geometry

The paste deposition is optimized in subsequent trials by modifying the printing parameters. The parameters of the last trial, for the realization of the joint in **Figure 2.17**, using a nozzle with a diameter of 1.6 mm, are reported in **Table 2.6**.

***Table 2.6** Printing parameters set on Voxalizer for the last deposition trial for the realization of the joined sample*

PRINTING PARAMETERS	
Layer count	1
Layer height	0.6 mm
Pat width	160 mm
Travel speed	120 mm/s
Print speed	1 mm/s
Retraction height	10 mm
Retraction amount	0 mm
Retraction speed	10 mm/s
Retraction min distance	0
Extra length on restart	0 mm

3. RESULTS AND DISCUSSION

3.1. Design of high-pressure resistant joints by surface tailoring

3.1.1. Laser processing and profilometry

There are limited studies in the scientific literature about the effect of surface roughness on the wettability and bonding strength of glass-ceramic sealants on metallic interconnectors and other SOFC/SOEC components. Smeacetto et al. [63] and Altan et al. [95] showed beneficial effects in increasing surface roughness, respectively related to torsional shear strength and tensile strength of Crofer22APU/sealant/Crofer22APU joints. Specifically, in Smeacetto et al., a 30% increase in torsional shear strength is registered, thanks to the mechanical interlocking effect given by glass infiltration inside the laser-generated protrusions. In this work, surface laser modification are applied on Crofer22APU substrates in order to assess improvements in wettability and pure shear strength of the joined substrates through Single Lap Offset test. The roughness of the obtained surfaces is evaluated through profilometric analysis, as explained in Section 2.2. Basing on experimental results, also the roughness of 3YSZ substrates is measured in order to address a possible influence of this factor on the joining process outcome.

3.1.1.1.3YSZ substrates

The results of the profilometric analysis on 3YSZ substrates, listed in Section 2.1.3, are shown in **Table 3.1**. Two measurements are performed in different areas of the surface. These results reveal no relevant differences between the different 3YSZ substrates, with all of them having a fairly smooth surface.

Table 3.1 *Roughness parameters of 3YSZ substrates evaluated through analysis at the profilometer*

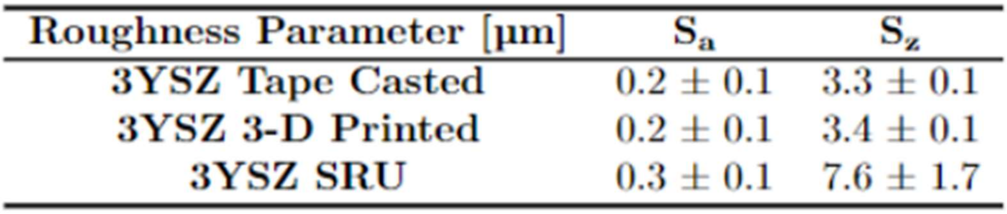

Roughness Parameter [μm]	S_a	S_z
3YSZ Tape Casted	0.2 ± 0.1	3.3 ± 0.1
3YSZ 3-D Printed	0.2 ± 0.1	3.4 ± 0.1
3YSZ SRU	0.3 ± 0.1	7.6 ± 1.7

A recostruction of the surface obtained through the profilometric analysis is reported in **Figure 3.1** for the 3D printed electrolyte, the roughest among the three surfaces.

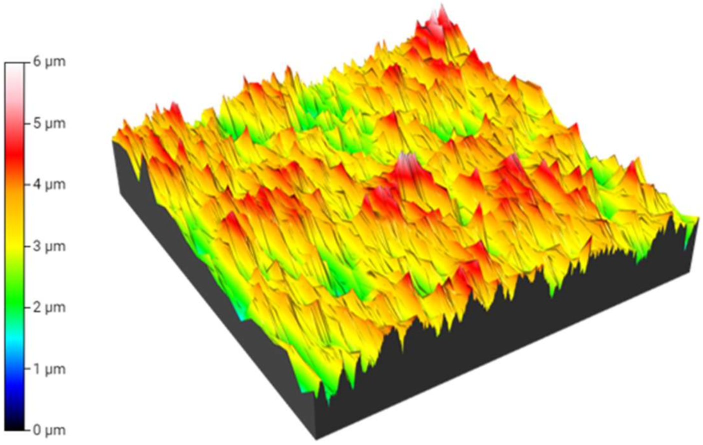

Figure 3.1 *3D-surface obtained through the profilometric analysis of 2x2 mm square of the 3D-printed electrolyte from SRU of the final SOEC stack*

Additionally, small differences in surface roughness are registered between the two opposite sides of the 3D-printed electrolyte, with the bottom part during 3D printing being rougher concerning the other one.

3.1.1.2.Crofer22APU substrates

The results of the profilometric analysis on Crofer22 APU substrates are reported in **Table 3.2**.

Table 3.2 *Roughness parameters obtained through profilometric analysis of as-received Crofer22 APU and lasered Crofer22 APU*

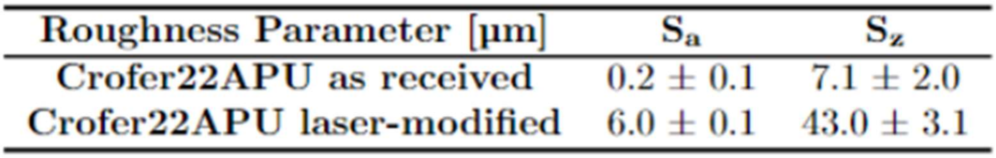

Roughness Parameter [µm]	S_a	S_z
Crofer22APU as received	0.2 ± 0.1	7.1 ± 2.0
Crofer22APU laser-modified	6.0 ± 0.1	43.0 ± 3.1

The laser modifications of the surface can be better appreciated looking at the FE-SEM image of **Figure 3.2**. Looking at the results, it is easy to observe relevant differences in surface roughness parameters. As-received Crofer22 APU presents a smooth surface, similar to the 3YSZ substrates for SLO. On the contrary, the lasered Crofer22 APU S_a parameter is thirty times higher than the S_a of the polished ones. The high value of S_z indicates the presence of significant peaks and pits.

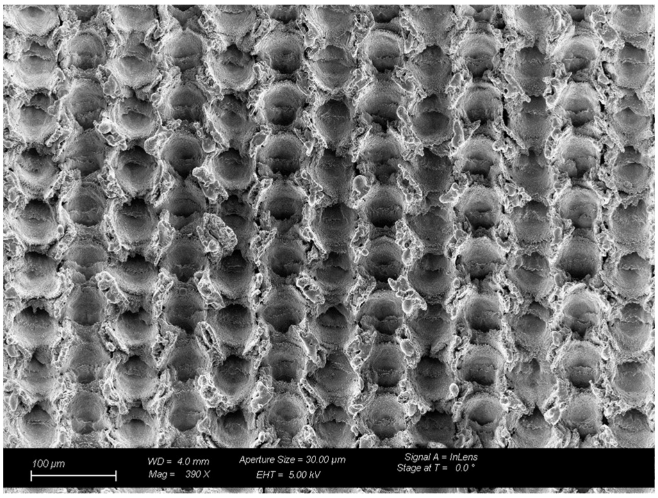

Figure 3.2 *FE-SEM image of Crofer22APU surface after laser process*

These remarkable differences can be observed in the reconstructed 3D-surface by profilometric analysis in **Figure 3.3**.

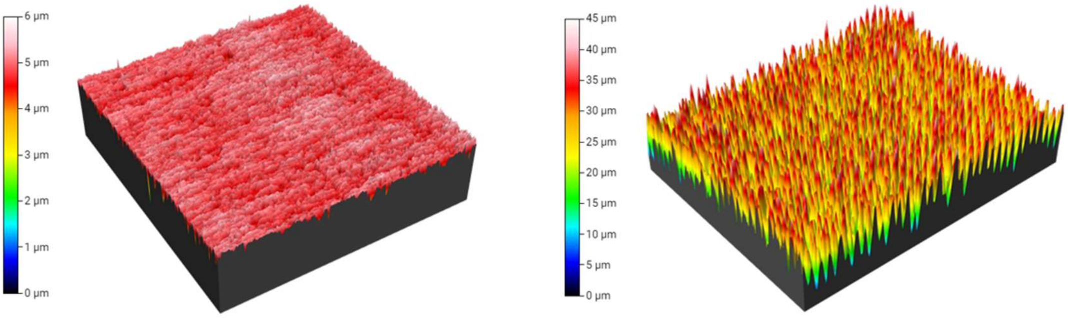

Figure 3.3 *3D surface generated through profilometric analysis of an area of 2x2 of the polished and lasered Crofer22 APU substrates*

Another relevant consideration on the laser-processed surface characterization is related to the formation of a Fe and Cr rich oxide scale identified by Smeacetto et al. through XRD analysis, showing a Cr_2FeO_4 phase [63]. This is due to the fact that the laser process is performed in static air atmosphere and, therefore, in presence of oxygen. The effect of this oxide scale on long term operation of SOC is yet to be assessed.

3.2. Glass-ceramic sealants for SOCs: thermal, thermo-mechanical and rheological characterization

3.2.1. Thermal and thermo-mechanical analysis of the sealants

The following sections address the thermal analysis, that is DSC, HSM and DIL, performed on commercial glass powders and, in the case of DIL analysis, on pellets obtained starting from powders by uniaxially pressing, and subsequently through sintering and crystallization of the sample by means of the thermal treatment reported in the datasheets.

3.2.1.1.DSC and HSM results

Experimental DSC curves for glass powders are shown in **Figure 3.4 (a)**. It can be observed that the three glasses have different characteristic temperatures, with T_g (glass transition temperature) ranging from 610 $°C$ to 715 $°C$ and T_c (glass crystallization temperature) from 741 $°C$ to 980 $°C$.

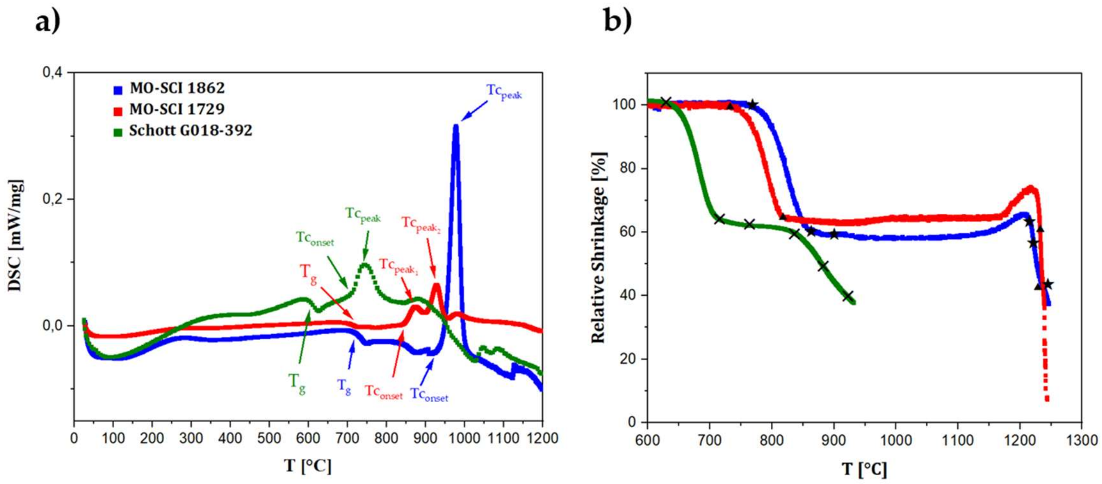

Figure 3.4 *In this figure the DSC curves (a) and the HSM curves (b) for the glasses MO-SCI 1862, MO-SCI 1729 and SCHOTT G018-392 are reported. In (b), the black crosses identify the characteristic temperatures for SCHOTT G018-392, the black triangles for MO-SCI 1729 and the black stars for MO-SCI 1862.*

The values of temperatures for the glass transition, onset and peak of crystallization are reported in **Table 3.3**. Moreover, it can be observed that the glass MO-SCI 1729 shows two crystallization peaks, respectively at 875 and 930 $°C$. DSC analysis is performed also on glass powder pastes in order to determine the burnout time and temperature of the organic additives. The additives evaporation and burning out temperatures are identified by the negative and positive peaks at about 70, 150 and 300 °C.

Table 3.3 *Characteristic temperatures extrapolated from DSC results for MO-SCI 1729, MO-SCI 1862 and SCHOTT G018-392*

Characteristic T [°C]	T_g	Tc_{on}	Tc_{peak1}	Tc_{peak2}
MO-SCI 1862	715	930	980	-
MO-SCI 1729	705	845	875	930
SCHOTT G018-392	610	711	741	-

With reference to **Table 2.2**, it can be noticed that the producers suggest temperatures for the thermal treatment at the onset of the crystallization process for MO-SCI 1729 glass, below the crystallization onset for MO-SCI 1862 and beyond the crystallization peak in the case of SCHOTT G018-392.

Finally, a DSC is performed on pastes composed of SCHOTT G0183-392 and 3YSZ at 5 and 10 percent in weight in order to observe possible variations in the characteristic temperatures. However, no differences are registered.

Figure 3.4(b) shows the curves measured through Hot-Stage Microscopy with the relative shrinkage of the cylindrical sample as function of the temperature. The characteristic temperature identified on HSM curves are reported in **Table 3.4**. Comparing these curves with the DSC results, it can be observed that the maximum sintering temperature is lower than the crystallization temperature for each one of the three glasses. Therefore, the formation of crystalline phases starts after the maximum densification of the system. It can be noticed that while MO-SCI 1862 and MO-SCI 1729 curves have a similar trend, SCHOTT G018-392 system has low characteristics temperatures.

Table 3.4 *Characteristic temperatures extrapolated from Heating Stage Microscopy results for MO-SCI 1729, MO-SCI 1862 and SCHOTT G018-392*

Characteristic T [°C]	T_{FS}	T_{MS}	T_D	T_S	T_{HS}	T_F
MO-SCI 1862	775	850	890	1215	1222	1237
MO-SCI 1729	740	825	-	-	1232	1237
SCHOTT G018-392	620	705	764	838	880	922

Consequently, a composite system, consisting in a paste based on SCHOTT G018-392 glass powder and 3YSZ powder, has been analysed. The 3YSZ powder is added in the paste formulation in order to obtain a homogeneous dispersion inside the system as explained in Section 2.4.2. Through HSM analysis of this composite system, an increase in the characteristic temperatures is observed, as it is possible to observe in **Figure 3.5** and **Table 3.5**.

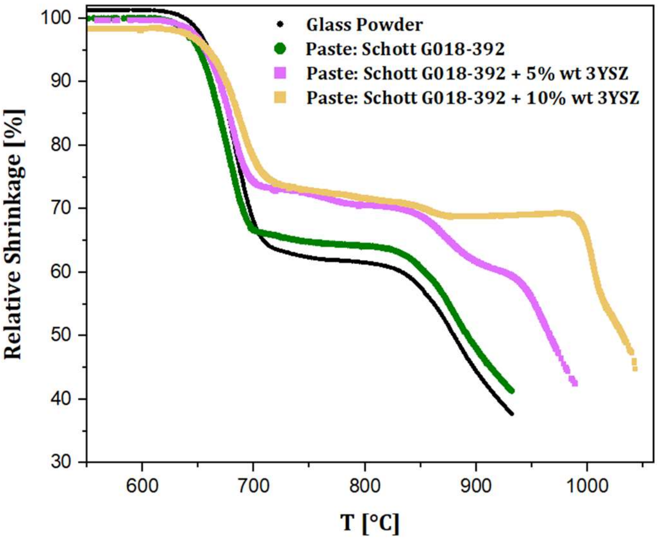

Figure 3.5 *HSM results for SCHOTT G017-392 pastes with 5% and 10% 3YSZ addition*

Table 3.5 *Characteristic temperatures extrapolated from HSM for SCHOTT G018-392/3YSZ pastes with 5wt% and 10wt% addition of 3YSZ*

Characteristic T [°C]	T_{FS}	T_{MS}	T_D	T_S	T_{HS}	T_F
SCHOTT G018-392	620	705	764	838	880	922
SCHOTT G018-392 + 3YSZ 5%wt	630	705	806	855	933	979
SCHOTT G018-392 + 3YSZ 10%wt	630	720	811	987	1004	1035

HSM curves can be used, as explained in Section 2.3.1.2, for the calculation of the viscosity curves of the glass systems as function of temperature. The viscosity curves are reported in **Figure 3.6**. It is possible to observe the increase in viscosity for the SCHOTT G018-392 systems with the addition of 3YSZ. These results are matched in scientific literature for glass/YSZ composites realized with different methods, such as mixing and milling of glass and YSZ inert particles [104], [105].

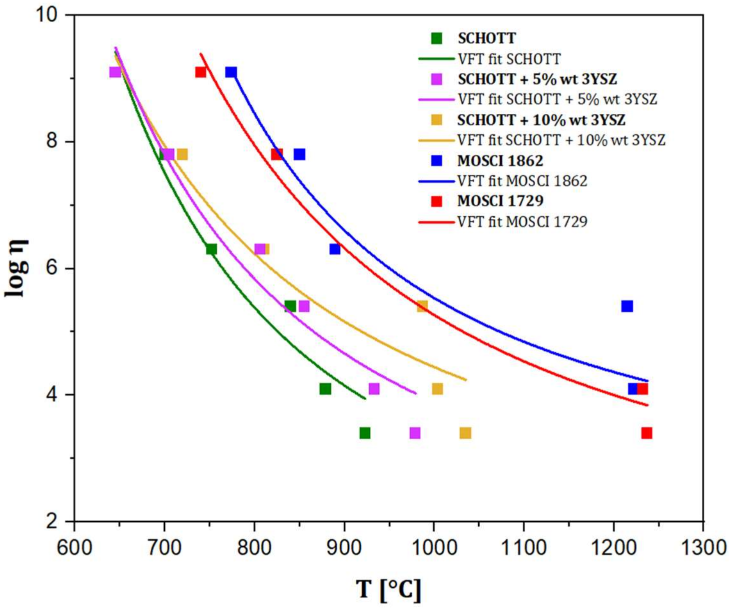

Figure 3.6 *Viscosity curves of the glass systems and the SCHOTT G018-392/3YSZ systems evaluated using the Vogel–Fulcher–Tammann equation*

3.2.1.2.Dilatometry

The experimental data collected in the dilatometric analysis of pellets obtained through uniaxial pressing of glass powders, thermally treated as reported in **Table 2.2**, are represented in **Figure 3.7**, with T_G and T_S being the glass transition temperature and the softening dilatometric temperature, respectively.

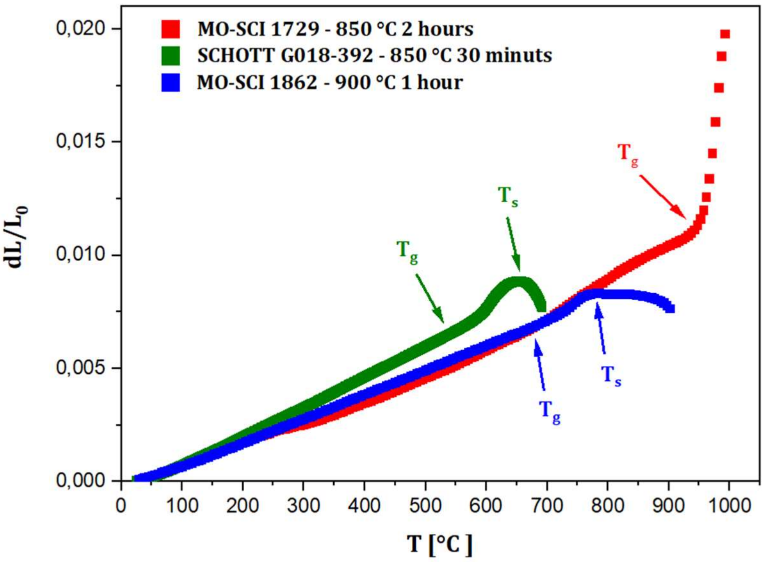

Figure 3.7 *DIL curves for the three glass-ceramic systems obtained through the suggested thermal treatments in the datasheet of the commercial glasses.*

The Coefficient of Thermal Expansion of the glass-ceramics are compared in the range $300 - 500\ ^{\circ}C$ where the dilatometric curve is linear for all the three systems. The CTEs are listed in **Table 3.6**.

Table 3.6 *Coefficients of thermal expansion and dilatometric characteristic temperatures obtained through dilatometric analysis for the different glass-ceramic systems. The CTEs are evaluated in the range 300-500 °C are all the curves follows a linear trend.*

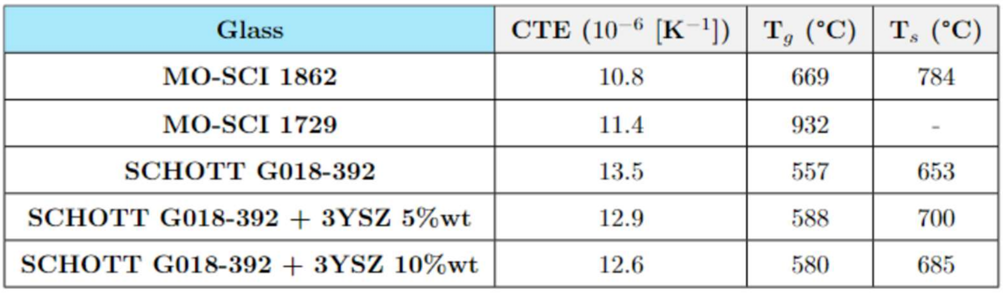

Glass	CTE (10^{-6} [K^{-1}])	T_g (°C)	T_s (°C)
MO-SCI 1862	10.8	669	784
MO-SCI 1729	11.4	932	-
SCHOTT G018-392	13.5	557	653
SCHOTT G018-392 + 3YSZ 5%wt	12.9	588	700
SCHOTT G018-392 + 3YSZ 10%wt	12.6	580	685

In the case of SCHOTT G018-392, the pellets are realized also using the pastes with 3YSZ addition in order to evaluate possible variations of characteristic temperatures and CTE. The pellets are obtained after paste drying and pressing, followed by the same thermal treatment to which SCHOTT G018-392 system is subjected. The curves are reported in **Figure 3.8**. Increasing the amount of 3YSZ, it is possible to observe a reduction in the CTE of the system, shifting from 13.5 X 10^{-6} K^{-1} to 12.6 X 10^{-6} K^{-1} in case of 10wt% 3YSZ addition. The reduction is most likely related to the contribution of the lower CTE of 3YSZ. Moreover, an increase in the softening point is registered in the case of the SCHOTT G018-392/3YSZ composite system, shifting from 653 °C to 700 °C in the case of 5wt% addition of 3YSZ.

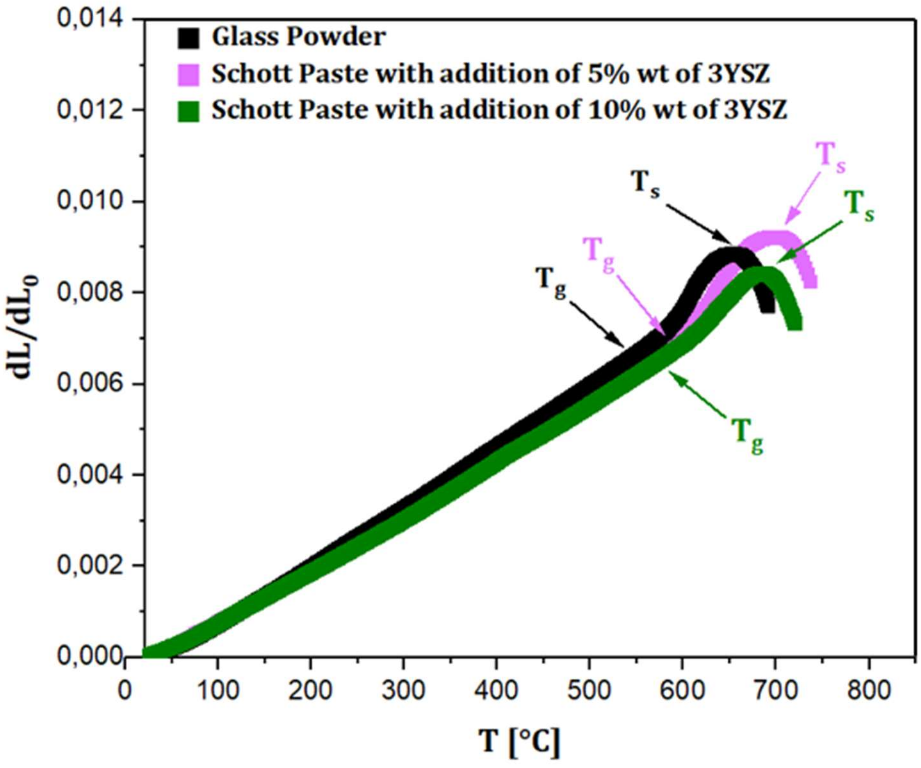

Figure 3.8 *DIL curves for SCHOTT G018-392/3YSZ systems compared with DIL for SCHOTT G018-392 glass-ceramic*

3.2.2. Rheological analysis of pastes

3.2.2.1. Particle sized distribution

Aiming to determine the particle size of the three glass systems used in this study (i.e., MO-SCI 1862, MO-SCI 1729 and SCHOTT G018-392) FESEM micrographs have been analysed by means of the ImageJ software. From this analysis, it emerges that the glass powders are characterized by similar heterogeneous distributions, with particles ranging from 1 ÷ 2 μm to more than 40 μm (**Figure 3.9**). Nevertheless, for each glass approximately the 80% of the particles lie in the range $0\ to\ 5\ \mu m$. This analysis is in accordance with the value presented in the datasheet, where it is reported a maximum particle size of 45 μm, without specifying the actual distribution.

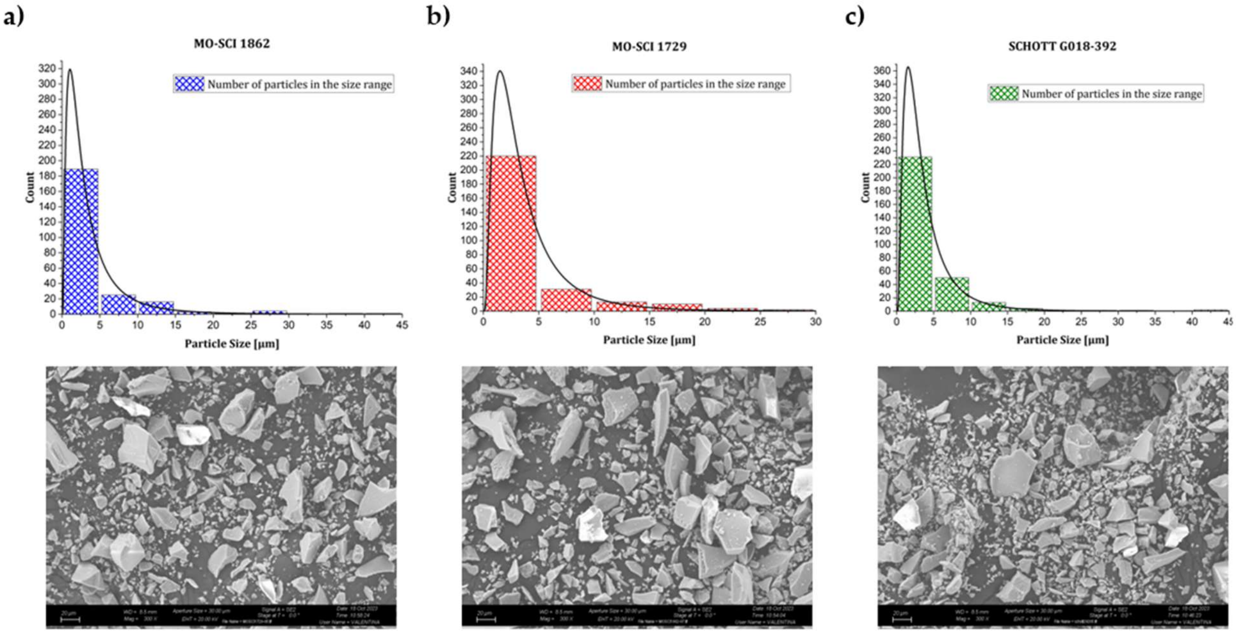

Figure 3.9 *In this figure, the particle size distributions for the three analysed commercial glasses using FE-SEM images and ImageJ analysis are reported: a)MO-SCI 1862, b)MO-SCI 1729 and c)SCHOTT G018-392.*

3.2.2.2.Rheological characterization

In this section, the rheological characterization of the pastes realized with each one of the three analysed commercial glasses is reported. As discussed in Section 2.4.2, rheological tests simulating the real printing conditions are done in order to preliminarily assess the printability of the pastes by means of robocasting technique.

Before analysing the inks at the rheometer, it is possible to observe relevant differences in viscosity by taking the pastes with a spatula and observing how and how fast the dripping evolves (see **Figure 3.10**). In this way it is possible to preliminarily observe that pastes realized with MOSCI 1862 and MOSCI 1729 are considerably more viscous with respect to SCHOTT G018-392 pastes.

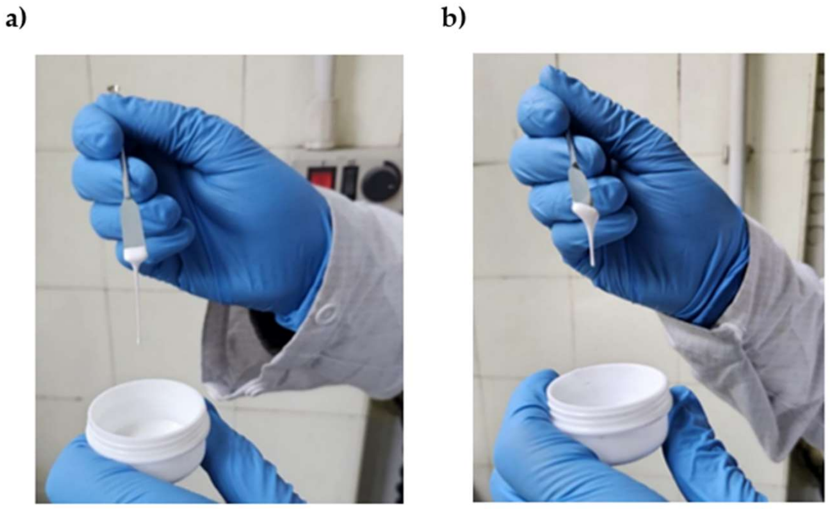

Figure 3.10 *SCHOTT G018-392 pastes after the mixing process with a solid loading of: (a) 75% and (b) 80%.*

Steady-shear Flow Sweep test results

During extrusion, the inks are subjected to elevated shear rates. Steady-Shear Flow Sweep Test is performed in order to simulate this condition and the evaluated viscosity is plotted as function of the shear rate. From **Figure 3.11** it is possible to observe that each paste follows a shear thinning behaviour, with viscosity decreasing as the shear rate is increased. The viscosity reduction while extrusion pressure is applied facilitate the process and avoid nozzle clogging. Nevertheless, there are substantial differences in viscosity values among the inks. Since observing the particle size distribution in **Figure 3.9,** it is possible to note that there are no relevant differences between the commercial glasses powder, this result is most likely related to the inter-particle interactions.

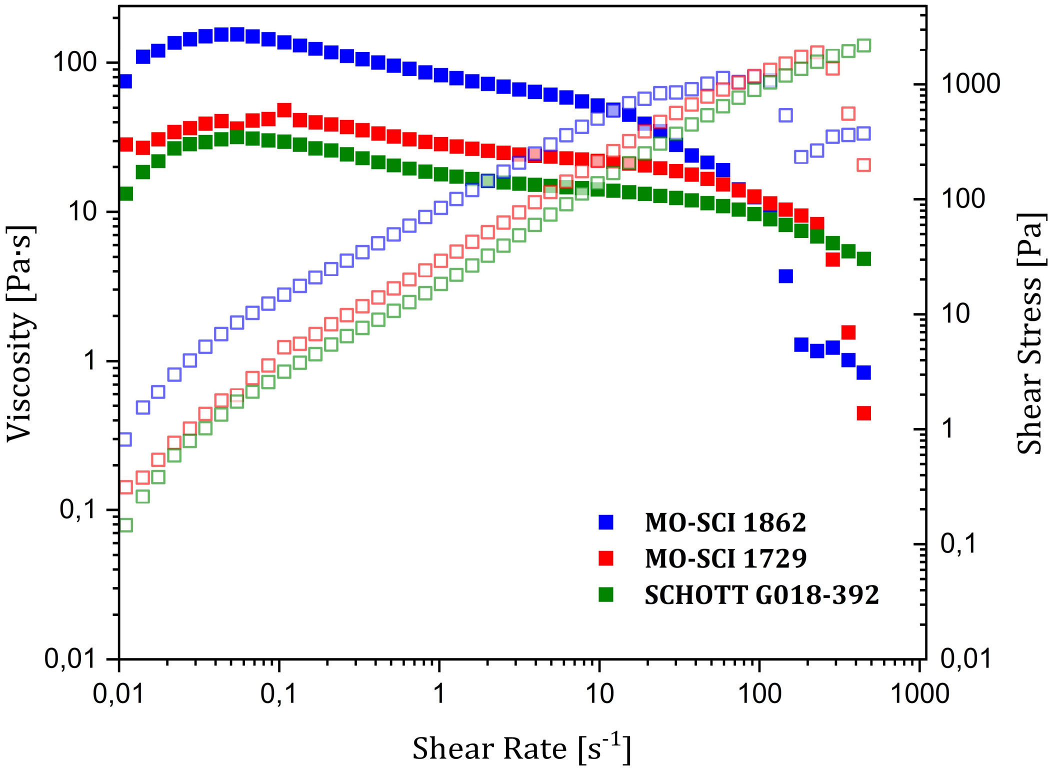

Figure 3.11 *Steady-Shear Flow Sweep Test for three pastes realized with the analysed commercial glasses. The shear rate is varied from 0.01 s^{-1} to 500 s^{-1}*

MO-SCI 1862 paste shows the highest viscosity up to approximately shear values of 100 s^{-1}, followed by a sudden drop and appearance of oscillations. This is mostly related to the paste rapture during the test at high shear rates (see **Figure 3.12**).

Figure 3.12 *Frame of the end of the Flow Sweep Test for MO-SCI 1862 paste, where it is possible to see ink outflow and rapture from the geometry*

Subsequently, the effect of 3YSZ powder addition to each system is analysed. A reduction of the viscosity of the inks for each system is observed, as reported in **Figure 3.13** for SCHOTT G018-392 pastes.

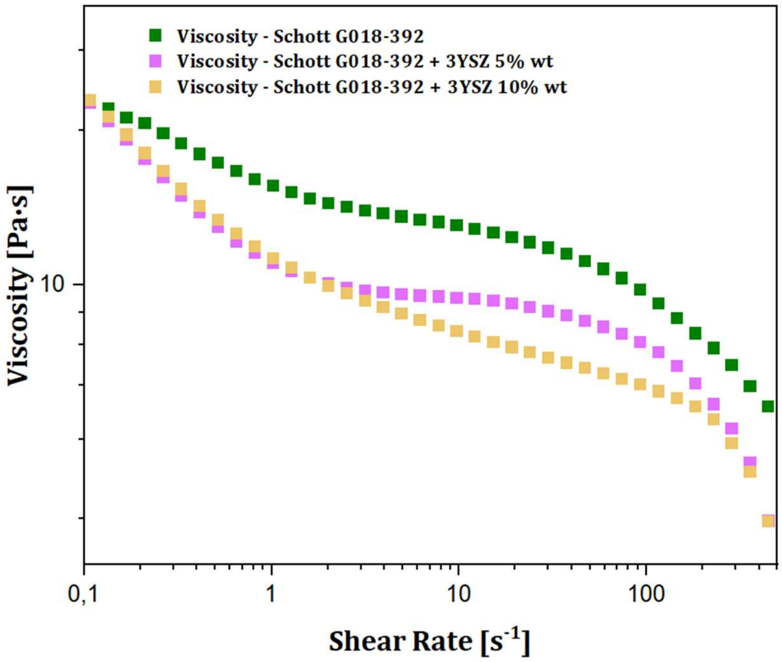

Figure 3.13 *Effect of 3YSZ powder addition to the colloidal suspension on the Steady-Shear Flow Sweep Test results for SCHOTT G018-392 pastes*

This result might be related to the dispersant-like role of 3YSZ particles which, having a smaller size with respect to glass particles, lead to the generation of a bi-modal particle size distribution, whose effect on rheological properties are discussed in Section 1.6.1.

A paste with such low values of viscosity, however, might not be suitable for Robocasting deposition, due to after deposition flowability and shape retention issues. As a consequence, a modification of the solid loading, another relevant parameter influencing the paste viscosity, is introduced in the analysis. In **Figure 3.14**, the effect of increasing the solid loading from the 75% to the 80%, keeping constant the additive percentages, is reported. The viscosity of the 80% solid loading pastes is substantially higher than the respective 75% solid loading pastes.

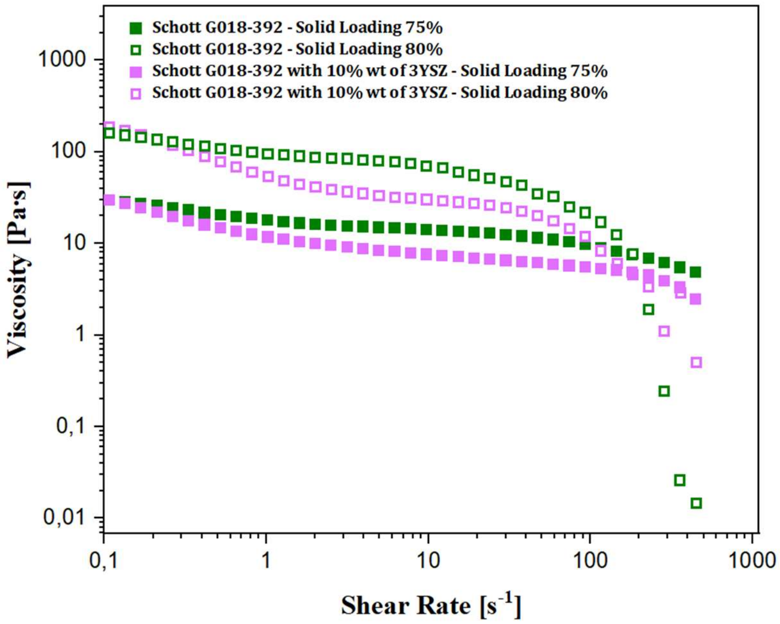

__Figure 3.14__ Effect of increasing the total solid loading of the ink from 75% to 80% for SCHOTT G018-392 and SCHOTT G018-392/3YSZ systems

Three Interval Thixotropy Test results

After deposition, the paste should ideally be able to recover its original viscosity value in order to retain its shape and avoid flow. The TITT test, whose results are reported in **Table 3.7** and **Figure 3.15**, simulates the transition between the extrusion phase and the rest phase after ink deposition on the substrate, by applying a high shear rate and subsequently a low shear rate. In this experiment, a shear rate of 10 s^{-1} is applied for 60 seconds and is followed by a shear rate of 200 s^{-1}applied for another 60 seconds. It is possible to observe that the pastes show different behaviour both in the high shear section and low shear section. In particular, the pastes with a higher viscosity show a lower viscosity recover with respect to low-viscosity pastes. In this sense, the addition of 3YSZ leads to an increase in the viscosity recover and paste stability at elevated shear rates.

__Table 3.7__ TITT viscosity recover with respect to the initial viscosity value of the inks after the first and second holding at a high shear rate of 200 s^(-1)

PASTE	INITIAL VISCOSITY [Pa*s]	1^{st} Recover [%]	2^{nd} Recover [%]
⬛ **MO-SCI 1862**	**45**	57	53
🟦 **MO-SCI 1862+3YSZ 5%wt**	**40**	80	56
🟥 **MO-SCI 1729**	**23**	58	42
🟦 **MO-SCI 1729+3YSZ 5%wt**	**14**	86	69
🟩 **SCHOTT G018-392**	**17**	74	65
🟪 **SCHOTT G018-392+5%wt**	**10**	73	70
🟧 **SCHOTT G018-392+10%wt**	**8**	94	92

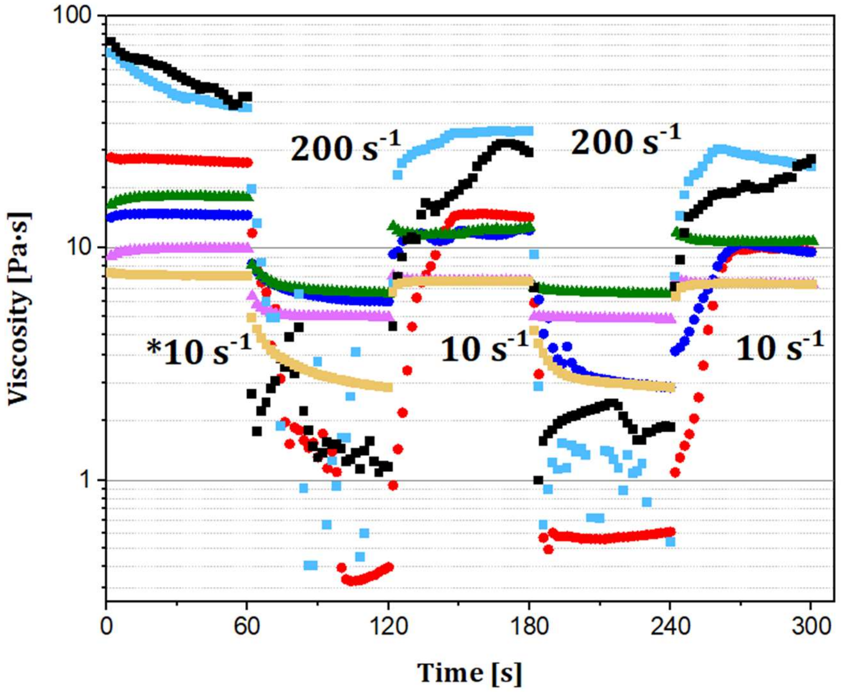

Figure 3.15 *TITT curves representing viscosity as function of time. *The pastes are initially subjected to a low shear rate of* $10\ s^{-1}$ *and to a subsequent high shear rate of* $200\ s^{-1}$*, simulating the resting and extruding steps of robocasting process*

Oscillatory Amplitude test results

To ensure self-support and subsequent layer support capabilities, the paste should present a liquid-like to solid-like transition after the extrusion and deposition processes with a sufficient yield stress. To characterize this behaviour, an oscillatory amplitude test for the evaluation of the critical stress and the definition of the solid and liquid region of the paste is used. In this type of test, the storage and loss modulus (see section 1.6.3) are measured as function of an increasing oscillatory amplitude of the rotating rheometer head at fixed frequency, equal to $1Hz$ in this experiment. The test is done on MO-SCI 1862 and SCHOTT G018-392+10%wt 3YSZ pastes with a solid loading of 75wt%.

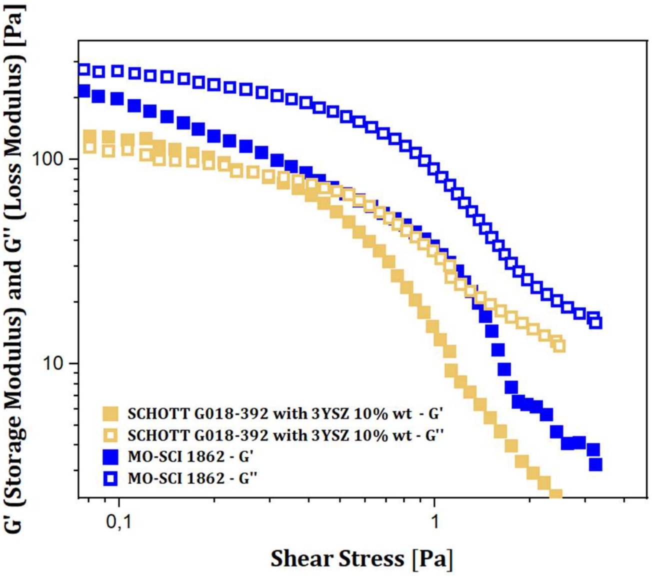

Figure 3.16 *Oscillatory Amplitude test at a fixed frequency of* $1Hz$ *for the evaluation of the solid-like to liquid-like transition behaviour of the analysed pastes*

From **Figure 3.16**, it can be observed that MO-SCI 1862 paste does not show a solid-to-liquid transition in the applied shear stress range. Indeed, the loss modulus is higher than the storage modulus for the whole stress range of the measure. On the other hand, SCHOTT G018-392 with 10%wt 3YSZ paste shows critical yield stress with solid-like to liquid-like transition at very low oscillation stresses. As a consequence, these pastes would probably not be suitable for Robocasting deposition process or, at least they would not be apt for realization of self-standing multilayered geometries.

3.3. Interconnect (Crofer22 APU) to electrolyte (3YSZ) joining

Completed the thermal characterization of the three commercial glasses, considered as candidates to be used as glass-ceramic sealant in SOEC applications, joined samples with interconnector and electrolyte materials are analysed. This is done through the realization of Crofer22APU/sealant/3YSZ joints, subsequently observed at a microstructural level through SEM analysis. Furthermore, glass-ceramic pellets are finely milled and XRD analysis is performed on the obtained powders and combined with EDS point analysis and mapping results in order to identify the crystalline phases formed during the joining and crystallization processes at elevated temperatures.

3.3.1. Morphological and chemical characterisation: SEM, EDS and X-ray diffraction analyses

Preliminary joints are realized using approximately 1x1 mm squares from a 3YSZ tape-casted thin sheet, of the order of some micrometres width, and from a Crofer22APU sheet having a width of 0.5 mm.

Observing the four joined samples shown in **Figure 3.17,** MO-SCI 1862 and MO-SCI 1729 glass-ceramic systems seem to have opposite compatibility behaviour with Crofer22APU and 3YSZ substrates. These joints are realized depositing glass powder pastes on Crofer22APU substrates, drying it at a temperature between 90 and 100 °C and leaning the 3YSZ tape on top of it. The samples in **Figure 3.17(b)** shows only the interface between MO-SCI 1729 sealant and Crofer22APU, since the 3YSZ tape is not joined with the glass-ceramic, showing poor wettability on the electrolyte material. On the other hand, good compatibility with Crofer22APU with absence of cracks and porosity occurs. As far as MO-SCI 1862 samples are concerned, from **Figure 3.17(a)**, this glass-ceramic system seem to show good compatibility with 3YSZ, whereas cracks are present at the glass-Crofer22 APU interface. Nevertheless, in the case of the lasered Crofer22APU, a good infiltration of the glass-ceramic during the joining process occurred with no interfacial cracking at both sides.

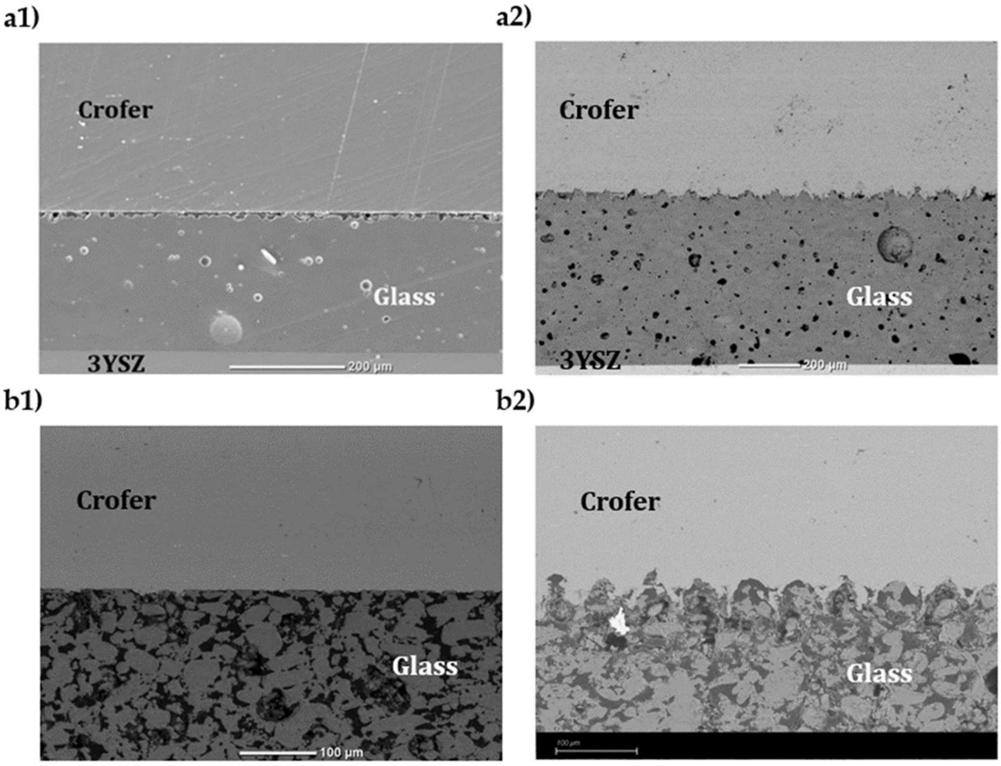

Figure 3.17 *MO-SCI 1862 (a) and MO-SCI 1729 (b) joined samples. The joints on the left are realized using as received Crofer22 APU substrates, while the ones on the right with lasered ones*

XRD, reported in **Figure 3.19**, performed on MO-SCI 1862 powder from milled pellet obtained through thermal treatment at 900 °C for two hours and EDS analysis, shown in **Figure 3.18** and **Table 3.8**, performed on the joined samples suggest the formation of Walstromite ($Ca_2BaSi_3O_9$) ICDD 01-073-1907.

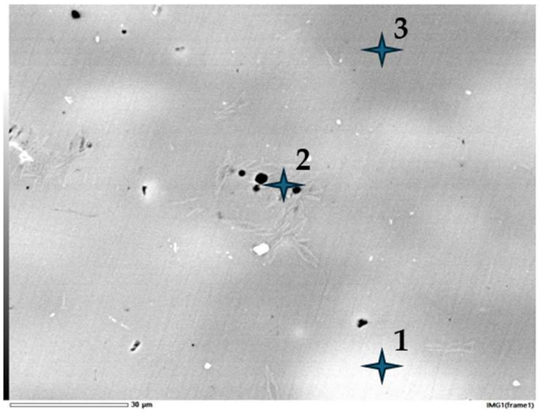

Figure 3.18 *SEM micrograph of a MO-SCI 1862 joined sample with the highlighted points of the EDS analysis.*

Table 3.8 *Point analysis results referred to the points highlighted in* ***Figure 3.18****.*

Atomic [%]	O	Si	Ba	Ca	Al
1	57.3	22.5	8.5	9.1	1.8
2	57.5	23.9	7.5	8.1	2.14
3	58.4	23.1	6.7	9.2	1.8

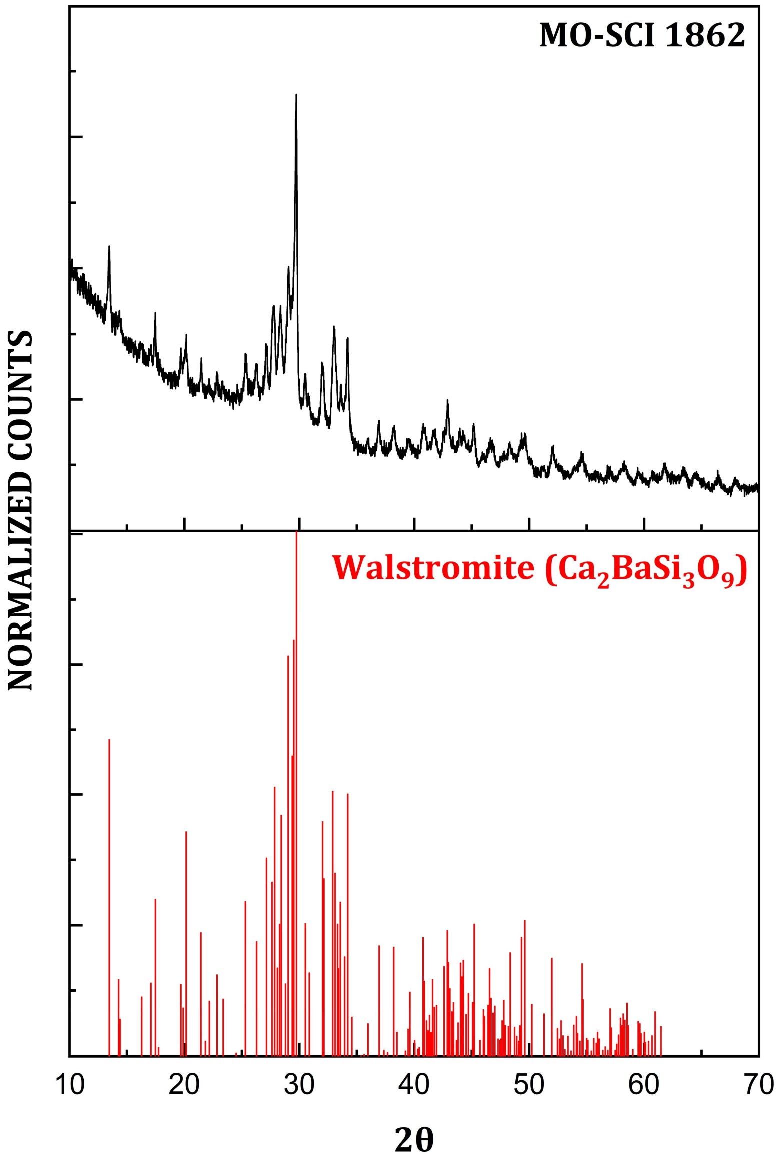

Figure 3.19 XRD analysis on MO-SCI 1862 glass-ceramic powder obtained after thermal treatment at 900 °C for 1 hour with ascending ramp of 5 °C/min and descending ramp of 3 °C/min

EDS analysis on MO-SCI 1729 joined sample suggest the formation of at least two different phases after thermal treatment at 850 °C for 2 hours. Precisely, basing on EDS results reported in **Figure 3.20** and **Table 3.9**, two strontium containing phases seem to be present: a Zinc-containing phase (light grey, point 1 and 2 in **Figure 3.20**) and one which does not contain zinc (dark grey, point 3 and 4 in **Figure 3.20**). Boron (B) atomic percentage is not reported, Due to difficulty of EDS analysis in identifying light elements.

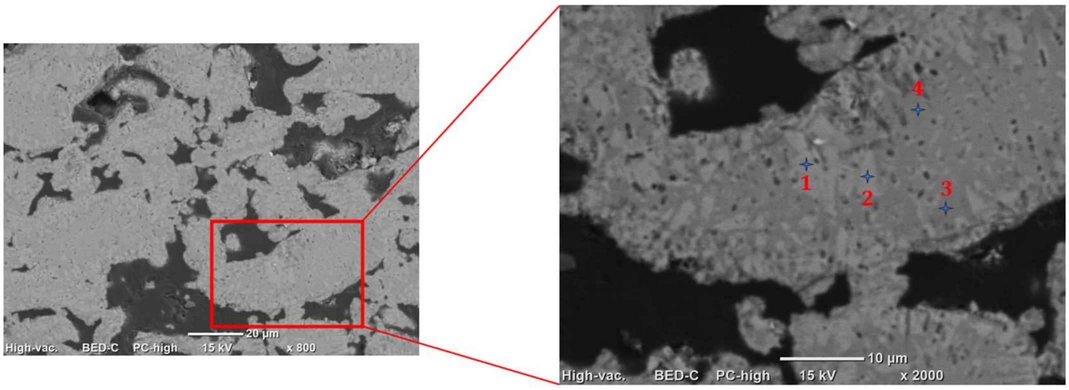

Figure 3.20 *SEM micrograph of a MO-SCI 1729 joined sample with the highlighted points of the EDS analysis.*

Table 3.9 *EDS analysis of Crofer22APU/MO-SCI 1729 referred to the points highlighted in* ***Figure 3.20****.*

Atomic [%]	O	Si	Sr	Ca	Al	Zn	Ti
1	56.7	16.3	11.9	7.3	1.8	4.6	1.2
2	54.7	17.2	12.3	7.3	1.8	5.2	1.5
3	58.5	16.5	9.7	11.2	2.3	0.6	1.2
4	53.3	17.9	10.5	9.9	2.2	1.8	1.3

XRD analysis (**Figure 3.21**) through Xpert-Highscore software identifies a Zinc-containing phase, Hardystonite ($Ca_2ZnSi_2O_7$, ICDD 00-035-0745), as one of the main phases. Two other phases can be identified through XRD analysis, namely the strontium containing phase Strontium Silicate $SrSiO_3$ (ICDD 01-087-0474) and Silicon Oxide (Coesite, ICDD 01-079-0445). Further analyses are needed to identify the peak at 28.3°.

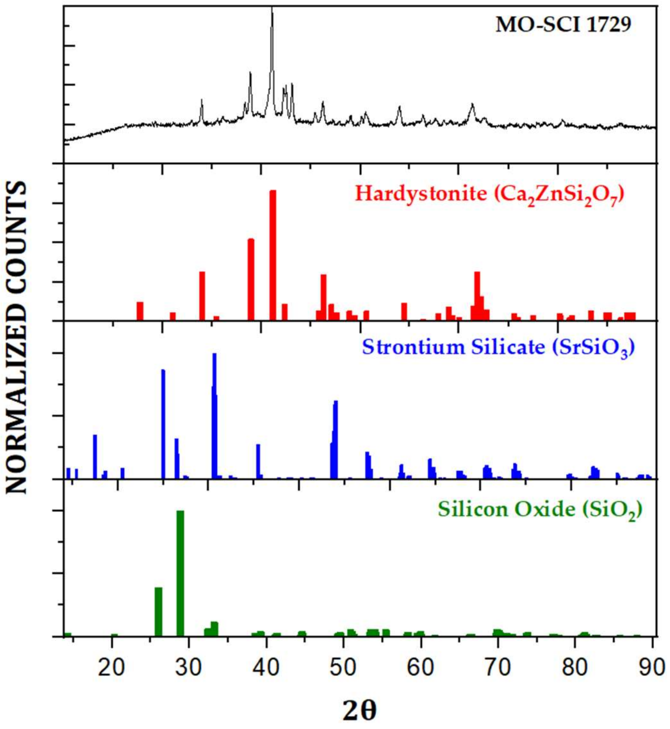

Figure 3.21 *XRD analysis on milled pellet of MO-SCI 1729 with a thermal treatment at 850 °C for 2 hours*

The SCHOTT G018-392 system led to encouraging results. As can be observed in **Figure 3.22,** good adhesion seems to be obtained with smooth interfaces at 3YSZ and Crofer22 APU sides, with no cracks or relevant pores.

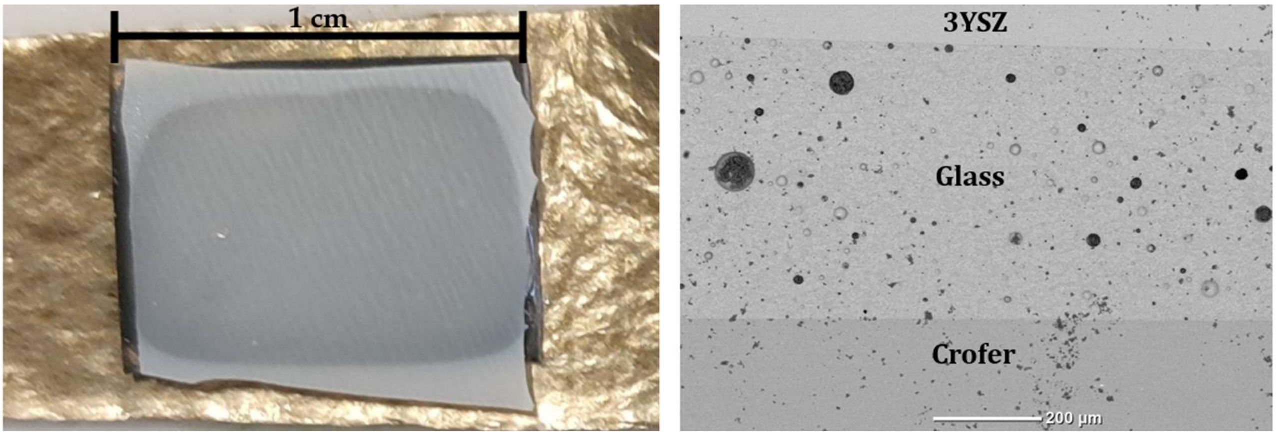

Figure 3.22 *SCHOTT G018-392 (paste) joined sample*

Other samples with 3YSZ tape are realized using pastes with 5wt% 3YSZ addition and with laser processed Crofer22APU. Even in this case, good results are obtained as can be seen in the SEM images of **Figure 3.23**, where good adhesion at 3YSZ side and infiltration in Crofer22 APU laser generated protrusion is obtained.

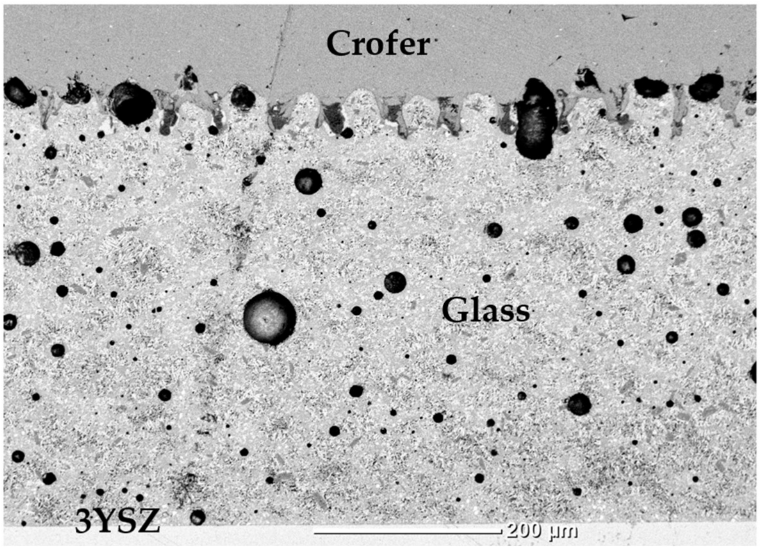

Figure 3.23 *SCHOTT G018-392 with 5%wt 3YSZ (paste) joined sample*

EDS point analysis and mapping are performed on joined samples to identify the different crystalline phases produced during the thermal treatment of the glass. **Figure 3.24** shows a micrograph and EDS calcium elemental map of the joined area of the Crofer22APU/Schott G018-392/ 3YSZ sample, treated at 850 °C for 30 minutes, with a heating/cooling rate of 5 $^{\circ}C/min$ and $3^{\circ}C/min$, respectively.

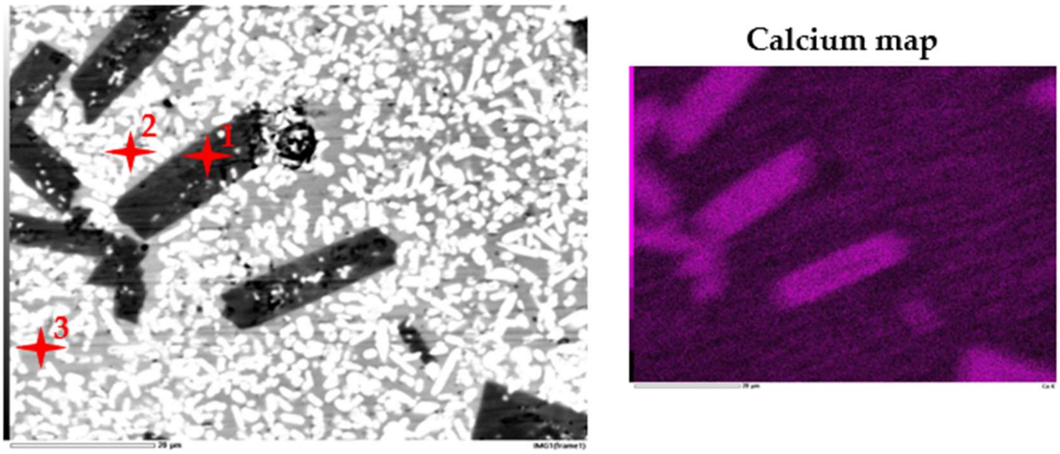

Figure 3.24 SEM micrograph of a Crofer22APU/ SCHOTT G018-392/3YSZ sample with calcium EDS elemental map.

Table 3.10 EDS Point analysis results referred to the points highlighted in Figure 3.24.

Atomic [%]	O	Si	Ba	Ca	Al	Zn
1	55.7	20.9	9.9	13.0	0.3	0.2
2	58.0	16.0	17.4	4.0	2.9	1.7
3	61.3	12.9	14.6	5.4	3.6	2.1

Table 3.10 EDS Point analysis results referred to the points highlighted in **Figure 3.24**. Coupling this with XRD analysis of **Figure 3.25**, it is possible to guess the crystalline phases characterising the glass-ceramic system. The major crystalline phase appearing is Barium Silicate ($BaSiO_3$, ICDD 00-026-1402), which should be represented by the needle-shaped white crystals. The second main phase could be Calcium-Barium Silicate ($BaCa_2Si_3O_9$, ICDD 01-073-1907), identified thanks to the EDS map of **Figure 3.24**, highlighting high Ca concentration in the big dark rectangular crystals.

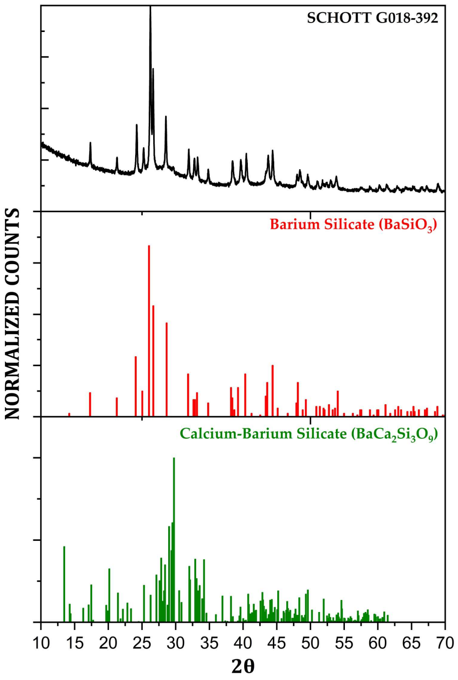

Figure 3.25 XRD analysis on SCHOTT G018-392 glass-ceramic powder obtained after thermal treatment at 850 °C for 30 min with heating rate of 5 °C/min and cooling rate of 3 °C/min

Some differences seem to arise in the composite system obtained through 3YSZ addition. SEM micrographs are taken from Crofer22APU/SCHOTTG01-392+10wt%3YSZ/3YSZ joined sample, treated at 850 °C for 30 min with a heating ramp of 5 °C/min and a cooling ramp of 3 °C/min Observing the micrograph of **Figure 3.26**, it is possible to notice the absence of the dark black crystals of the calcium containing phase of the SCHOTT G018-392 sample. On the other hand, looking at the XRD analysis results in **Figure 3.27**, performed on powder from pellet of SCHOTTG01-392+10wt%3YSZ treated at 850 °C for 30 min with ascending ramp of 5 °C/min and descending ramp of 3 °C/min, and the SEM micrograph, the white needle-shaped Barium Silicate phase seem to appear even in this case.

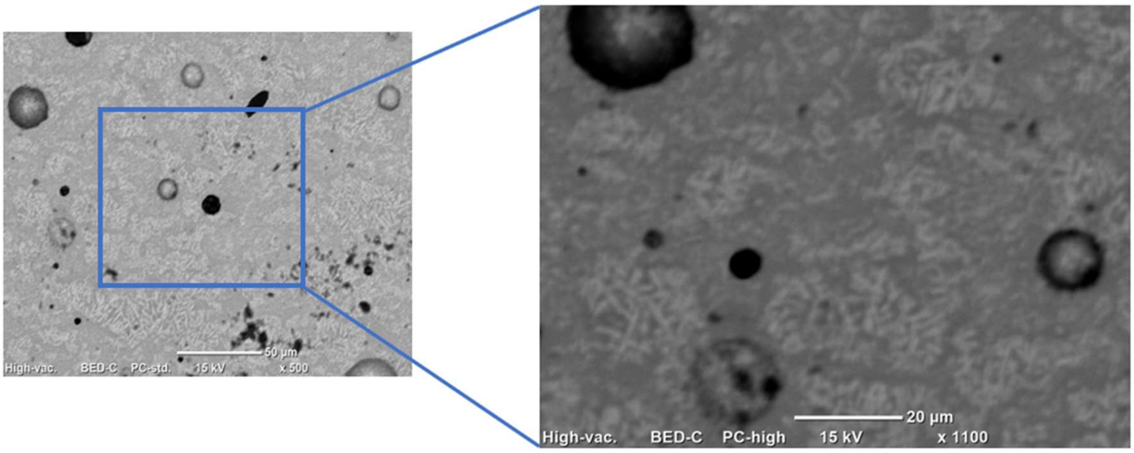

Figure 3.26 *SEM micrograph of Crofer22APU/SCHOTTG01-392+10wt%3YSZ/3YSZ joined sample, treated at 850 °C for 30 min with ascending ramp of 5 °C/min and descending ramp of 3 °C/min*

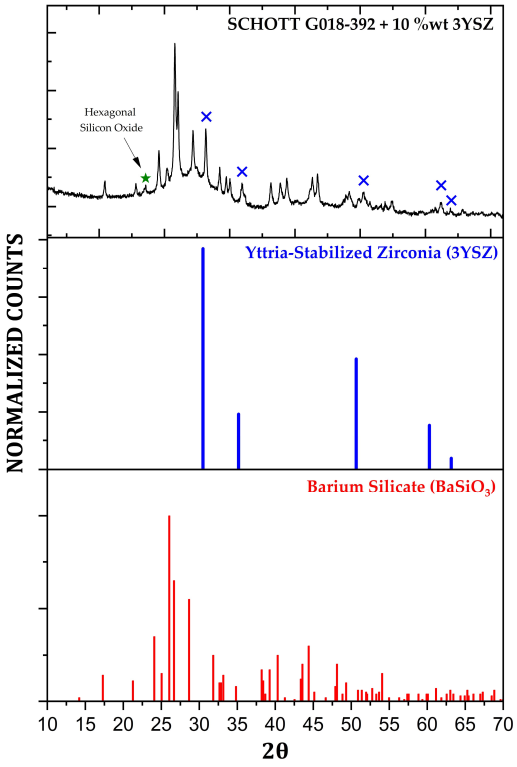

Figure 3.27 *XRD analysis performed on SCHOTT G018-392+10wt%3YSZ powder obatined from pellet treated at 850 °C for 30 min with ascending ramp of 5 °C/min and descending ramp of 3 °C/min*

The major difference with the previous XRD pattern is represented by the 3YSZ peaks, highlighted in **Figure 3.27**. EDS mapping on Zirconium (Zr) is performed in order to assess the degree of homogeneity of 3YSZ distribution throughout the glass-ceramic (see **Figure 3.28**). Furthermore, another hexagonal silicon oxide crystalline phase seems to be present in this composite system.

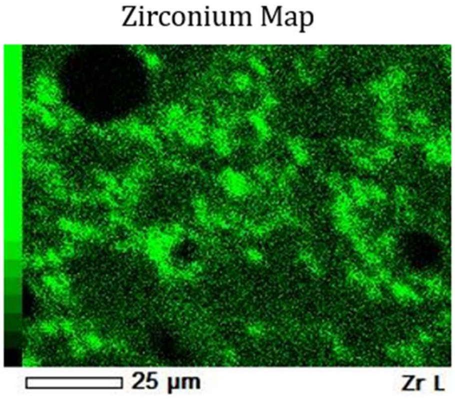

*Figure 3.28 EDS mapping of Zirconium (Zr) referred to **Figure 3.26***

Subsequently, joints are realized by cutting small squares from the actual 3YSZ 3D-printed electrolyte from the areas are the glass-ceramic will be deposited in the final stack. Joining tests are also attempted using 3YSZ and Crofer22APU thicker substrates used for the single lap offset mechanical tests (SLO).

MO-SCI 1729 (**Figure 3.29(a))** and MO-SCI 1862 (**Figure 3.29(b)**) joined samples with 3D-printed 3YSZ from the actual SRU electrolyte lead to unsuccessful result with complete or almost complete detachment of the joints during the polishing process, as it can be observed in **Figure 3.29**, probably due to poor adhesion and discontinuous interfaces at 3SYZ side.

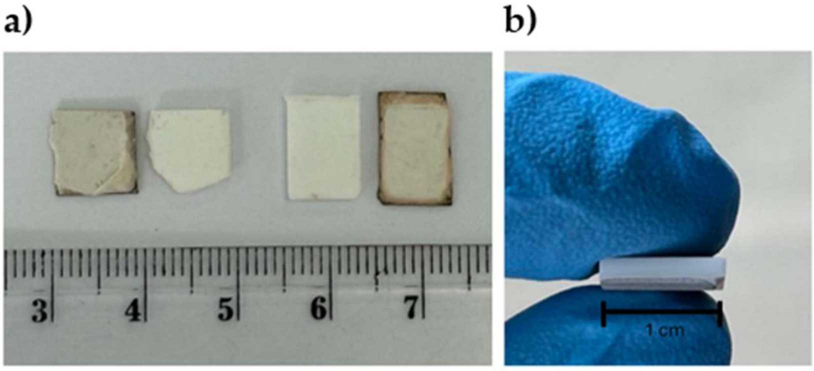

Figure 3.29 MO-SCI 1729 (a) and MO-SCI 1862 (b) joined samples

Other trials are done using SLO substrates, nevertheless, bad results are obtained even in this case. In **Figure 3.30**, a MO-SCI 1862 unsuccessful joined sample is shown. It is possible to observe the glass-ceramic sealant on 3YSZ side only and a yelloish layer which could be attributed to Cr-reaction layer. However, XRD analysis should be performed to asses the formation of barium chromate.

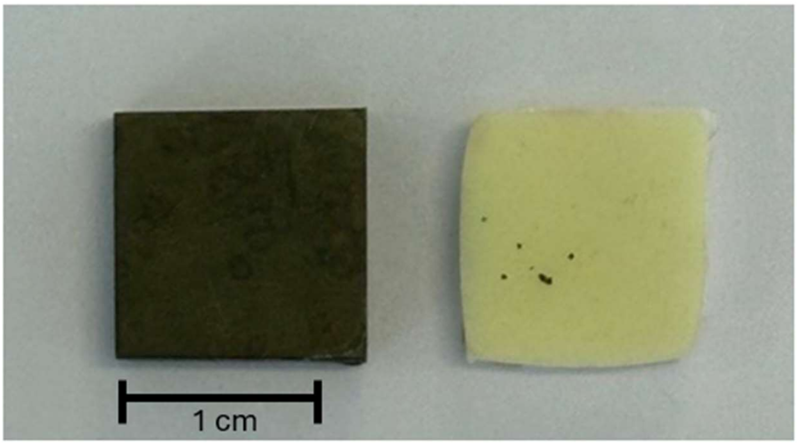

Figure 3.30 MO-SCI 1862 joined sample with half SLO substrates

A final attempt with MO-SCI 1729 and MO-SCI 1862 is done increasing the thermal treatment of 50 °C, from 850°C to 900 °C and from 900 °C to 950 °C, respectively. Using laser processed Crofer22APU, in order to try to increase the wettability on the metallic substrate, one sample each for SLO test are realized. The results of the mechanical tests are reported in Section 3.3.2.
On the contrary, SCHOTT G018-392 system and SCHOTT G018-392 with 3YSZ 10wt% addition system lead to good results in terms of joined samples observation with electrolyte and interconnector material. In **Figure 3.31**, SEM images of slurry deposited SCHOTT G018-392 are reported. These joined samples are subjected to a thermal ageing at 850 °C of 5 hours with a weight of 15 g/cm^2 in order to observe the high temperature behaviour of the glass-ceramic system. After the test, no spillage of the glass-ceramic and no relevant variation of the joint width are observed. Moreover, smooth interfaces with absence of cracks can be observed at both sides.

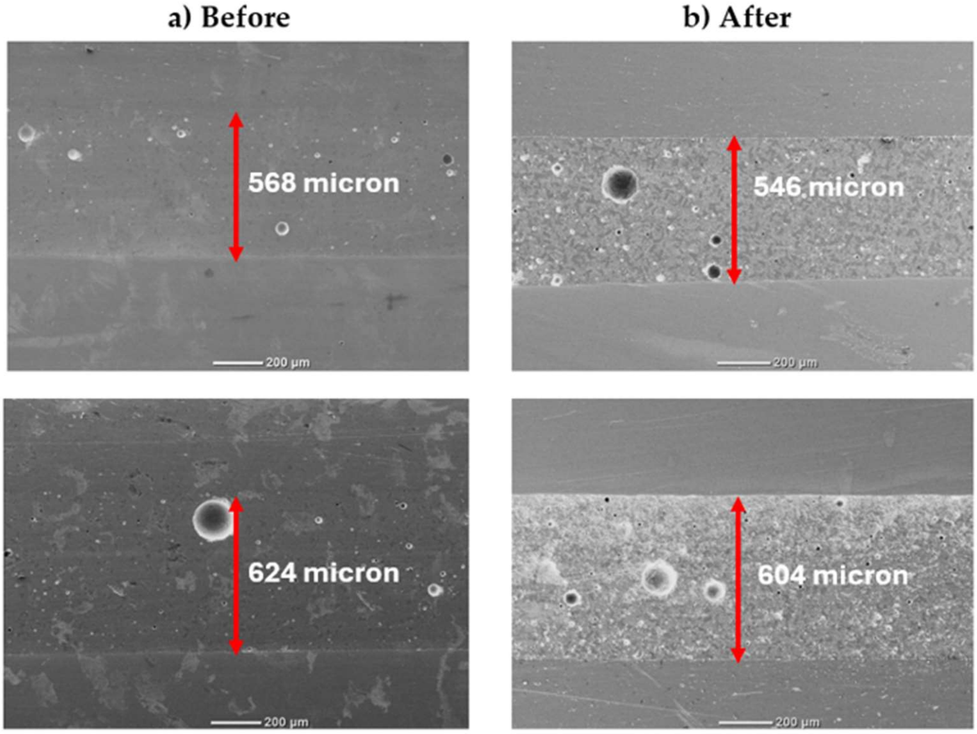

Figure 3.31 SCHOTT G018-392 "creep" test 5 hours at 850 °C with a weight of 15 g/cm^2. samples with 3YSZ electrolyte from SRU and Crofer22 APU (0.5 mm width)

Nonetheless, some cracks are identified in SEM images before the thermal ageing test, as shown in **Figure 3.32.**

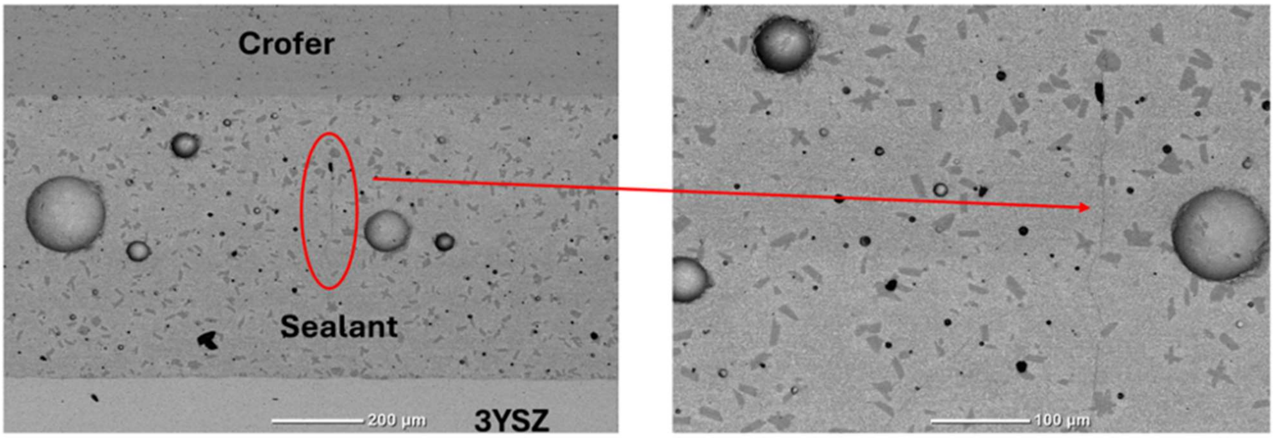

Figure 3.32 *SCHOTT G018-392 (slurry) as-joined samples with 3YSZ electrolyte from SRU and Crofer22 APU (0.5 mm width)*

Other joints are realized using SCHOTT G018-392 (**Figure 3.33(a)**) and SCHOTT G018-392+10wt%3YSZ (**Figure 3.33(b)**) pastes, with and without laser modified Crofer22APU. The results are reported in **Figure 3.33**. It is possible to observe that this 3D-Printed 3YSZ present a rougher surface concerning the tape-casted 3YSZ as evidenced by the higher S_z parameter (see Section 3.1.1.1). Even in this situation, good adhesion to the substrates is obtained.

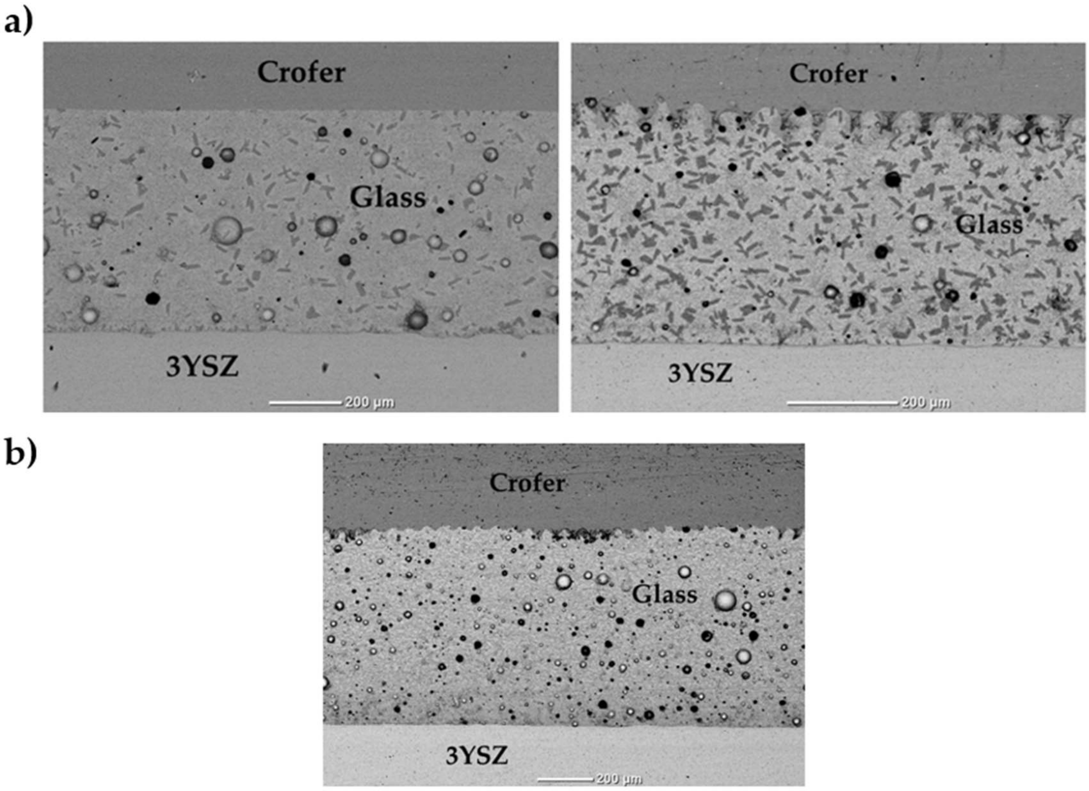

Figure 3.33 *SCHOTT G018-392 and SCHOTT G018-392+10%wt3YSZ (pastes) joined samples with 3YSZ electrolyte square cut from SRU and square of Crofre22APU (0.5 mm width)*

3.3.2. Mechanical test

During SOEC/SOFC operation the glass-ceramic sealant is subjected to both tensile and shear stresses. As a consequence, the long term reliable operation of the stack is strictly dependent on the mechanical properties of the sealant and of the joined system. In the present work, the method used for the evaluation of the pure shear strength of the metal-to-ceramic joint is the Single Lap Offset (SLO) test, in two different conditions: at room temperature and operative temperature.

As far as MO-SCI 1862 and MO-SCI 1729 glass systems are concerned, only two sample each are mechanically testes. The glass powders are deposited on the 3YSZ substrates as slurry obtained mixing powders and ethanol. The misaligned samples, realized as explained in Section 2.5, are done using lasered Crofer22APU substrates, since better glass infiltration and joining is registered from previous samples observing SEM images. Temperatures of 950°C and 900 °C with an ascending ramp of 5 °C/min and a descending ramp of 3 °C/min are used for the joining thermal treatment of MO-SCI 1862 and MO-SCI 1729, respectively. This is done since for both systems unsuccessful results are obtained using the suggested thermal treatments on the datasheets. Nevertheless, poor mechanical properties, reported in **Table 3.11**, are evaluated compared to SCHOTT G018-392 systems, discussed in the following paragraphs. From **Figure 3.34**, it is possible to observe one of the possible causes of the failed joining process, namely the possible formation of Barium and Strontium chromates. Further XRD analysis should be performed to confirm the formation of chromates

Table 3.11 *SLO test results for LaseredCrofer22APU/MO-SCI1862/3YSZ and LaseredCrofer22APU/MO-SCI1729/3YSZ joints*

	Shear Strength [Mpa]
MO-SCI 1729	4.1
MO-SCI 1862	1.4

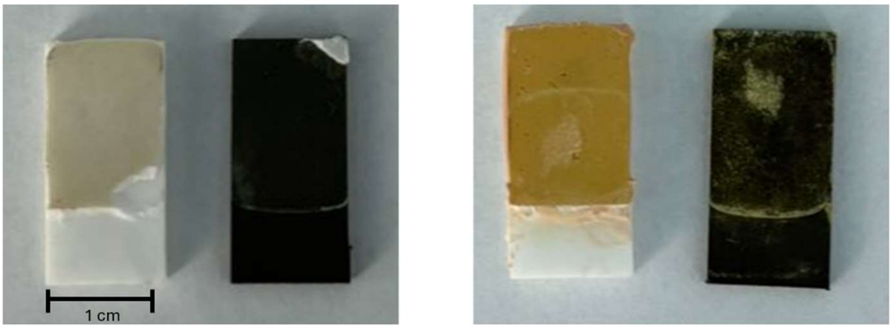

Figure 3.34 *MO-SCI 1862 and MO-SCI 1729 samples after SLO test*

As far as SCHOTT G018-392 is concerned, the glass powder is deposited on the 3YSZ substrates as a paste and four different configurations of joints are prepared, as explained in Section 2.5. Both SCHOTT G018-392 system and SCHOTT G018-392 with 10wt% 3YSZ addition system are analysed. The joints for SLO tests are prepared with as-received Crofer22 APU and lasered Crofer22 APU. This is done in order to assess a possible improvement in the pure shear strength of the as-joined samples and modification of the fracture surface nature, as reported in [63]. Three samples for each substrate-paste combination are analysed. The as-joined samples right after joining process in oven are shown in **Figure 3.35** for SCHOTT G018-392 paste.

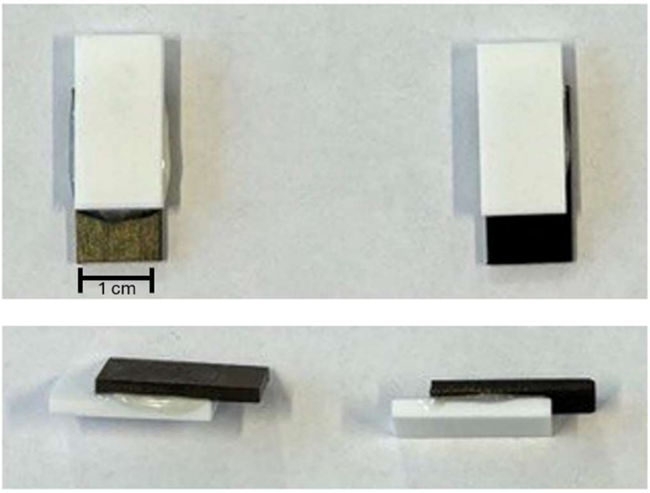

Figure 3.35 *Samples for SLO test obtained with SCHOTT G018-392 paste: polished Crofer22 APU (left) and lasered Crofer22APU (right)*

The results of the test are reported in **Table 3.12** along with the stress-displacement curves in **Figure 3.36** obtained through the testing device data for two of the analysed samples. It can be observed that the average results for shear strength are in line with the values reported in previous works using a similar testing setup [55], [57]. In contrast with the experimental evidence from [63], where a 30% increase in torsional shear strength is found with the laser modified Crofer22 APU surface, a slight increase in shear strength is registered in this case with laser modification introduction. Nevertheless, peak values of 15.5 Mpa and 23 Mpa are registered with SCHOTT G018-392 and SCHOTT G018-392/3YSZ systems with lasered Crofer22APU substrate. A broader measurement campaign, to be completed also with the tests for SCHOTT G018-392+10wt%3YSZ system with as received Croferr22 APU substrates, should be pursued in order to have more statistically reliable data.

Table 3.12 *SLO test results for LaseredCrofer22APU/SCHOTTG018-392/3YSZ and LaseredCrofer22APU/SCHOTTG018-392+3YSZ/3YSZ joints*

Shear Strength [Mpa]	Crofer22APU polished 320	Crofer22APU Laser modified
SCHOTT G018-392	13.1 ± 1.3	13.4 ± 2.4
SCHOTT G018-392 + 10%wt 3YSZ	-	16.8 ± 5.7

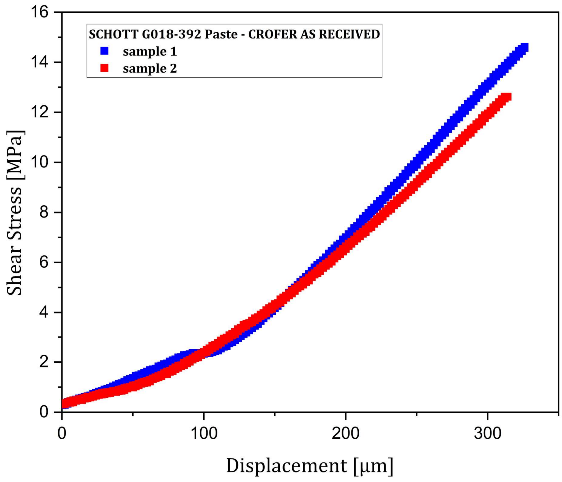

Figure 3.36 *Stress-displacement curves obtained through testing device data for two of the tested samples*

On the other hand, relevant differences are encountered in the fracture surface depending on Crofer22APU surface roughness. As-received Crofer22 APU having low values of surface roughness (**Table 3.2**) showed predominantly adhesive fracture surface with sealant on 3YSZ substrates after test and mixed mode fracture surface with glass-ceramic on both sides, as can be observed in **Figure 3.37(a1),** for SCHOTT G018-392, and **Figure 3.37((a2)**, for SCHOTT G018-392 with 10wt% 3YSZ. On the contrary, sample with laser modified Crofer22APU, presenting higher values of surface roughness, showed adhesive fracture surface with sealant on the Crofer22 APU side only, as can be observed in **Figure 3.37((b1),** for SCHOTT G018-392, and **Figure 3.37((b2)**, for SCHOTT G018-392 with 10wt% 3YSZ. Therefore, the laser modification and the resulting interlocking effect seem to improve the bond strength of glass-ceramic sealant with Crofer22APU.

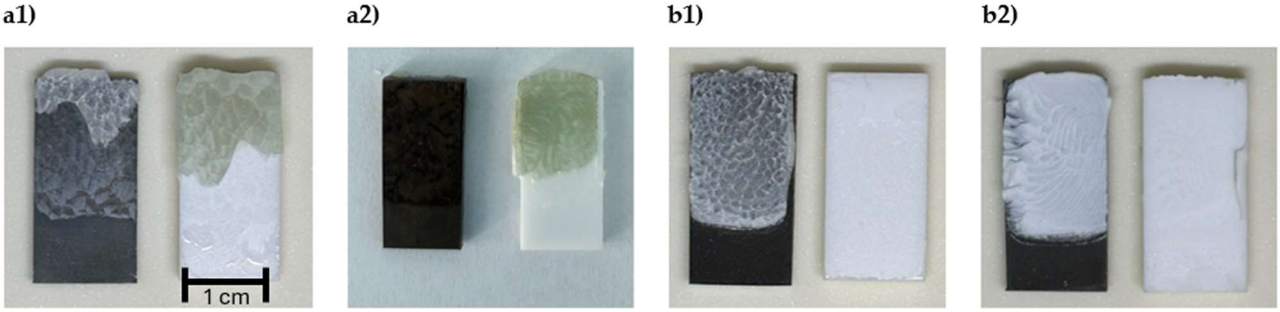

***Figure** 3.37 After SLO test pictures for two as-received Crofer22 APUsamples, as-rec.CROFER22APU/SCHOTT G018-392/3YSZ (a1) and as-rec.CROFER22APU/SCHOTT G018-392+10wt%3YSZ/3YSZ (a2), and two lasered samples, laseredCROFER22APU/SCHOTT G018-392/3YSZ (b1) and laseredCROFER22APU/SCHOTT G018-392+10wt%3YSZ/3YSZ (b2)*

3.4. Preparation of sealed substrates for high-pressure tightness testing under real operating conditions

Even if a broader experimental campaign on MO-SCI 1862 and MO-SCI 1729, basing on the available experimental results, i.e. joined samples observation through SEM and mechanical SLO tests results, discussed in Section 3.3, SCHOTT G018-392 with 10wt% 3YSZ addition is selected for the high-pressure tightness testing sample, explained in Section 2.5. The chosen paste for the Robocasting process, is the one with SCHOTT G018-392 and 10%wt of 3YSZ with a solid loading of 80%, considering the results of the rheological properties of Section 3.2.2.2, which show a higher viscosity with respect to the 75% solid loading paste. In the following paragraph, the various deposition trials are reported.

A 1.2 mm nozzle and the following parameters are used for the first deposition trial (**Table 3.13**):

Table 3.13 *Printing parameters set on Voxalizer for the first deposition trial*

PRINTING PARAMETERS	
Layer count	1
Layer height	0.6 mm
Pat width	60 mm
Travel speed	120 mm/s
Print speed	2 mm/s
Retraction height	1 mm
Retraction amount	0 mm
Retraction speed	10 mm/s
Retraction min distance	0
Extra length on restart	0.5 mm

For the first trial, a 36x36 mm square is generated by means of the Voxalizer software, as shown in **Figure 3.38**.

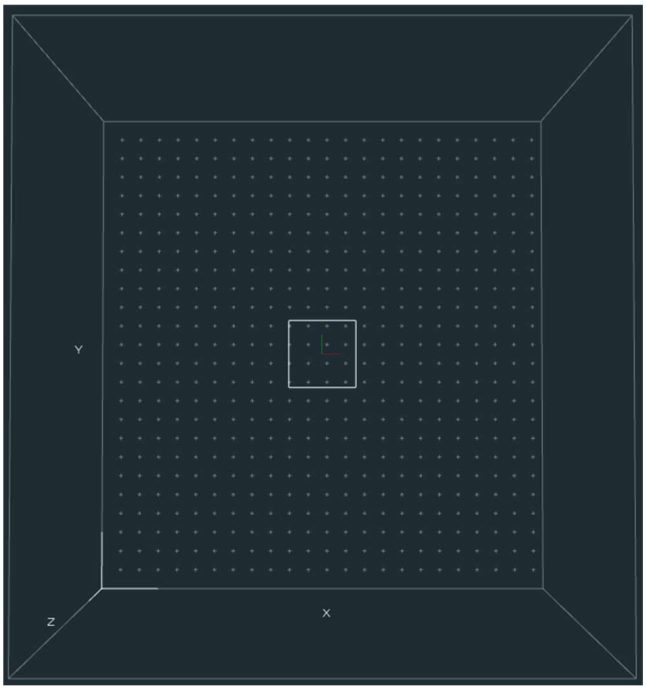

Figure 3.38 *Geometry generated for the first Robocasting deposition trial through Voxalizer graphic interface*

The geometry obtained using these printing parameters is shown in **Figure 3.39**. It can be observed that the resulting squares are characterized by the non-uniform width of the different sides and by irregularities in the bottom left corner. This could be mostly related to the low extrusion speed, regulated by the path width parameter, and by an excessively high amount of paste extruded at the beginning of the deposition.

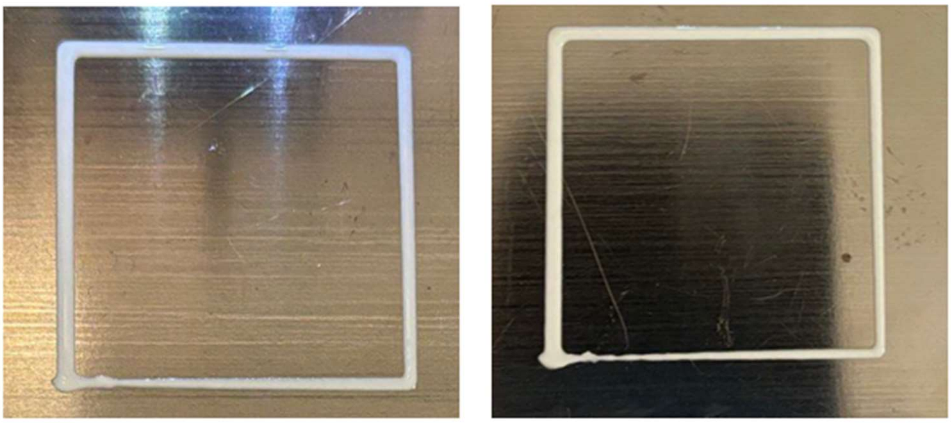

Figure 3.39 *Two deposition trials with the same printing parameters on Crofer22APU sheet*

A solution to the highlighted problems is found by adding the extrusion of a simple geometry before the deposition of the actual one (see **Figure 3.40**) and by increasing the path width parameter. Also, the retraction height is increased to avoid the interference of the nozzle with the deposited paste at the end of deposition. Finally, the extra length on restart is eliminated, because it is negatively influencing the first deposition moments. The printing parameters for the second deposition trial are listed in **Table 3.14**

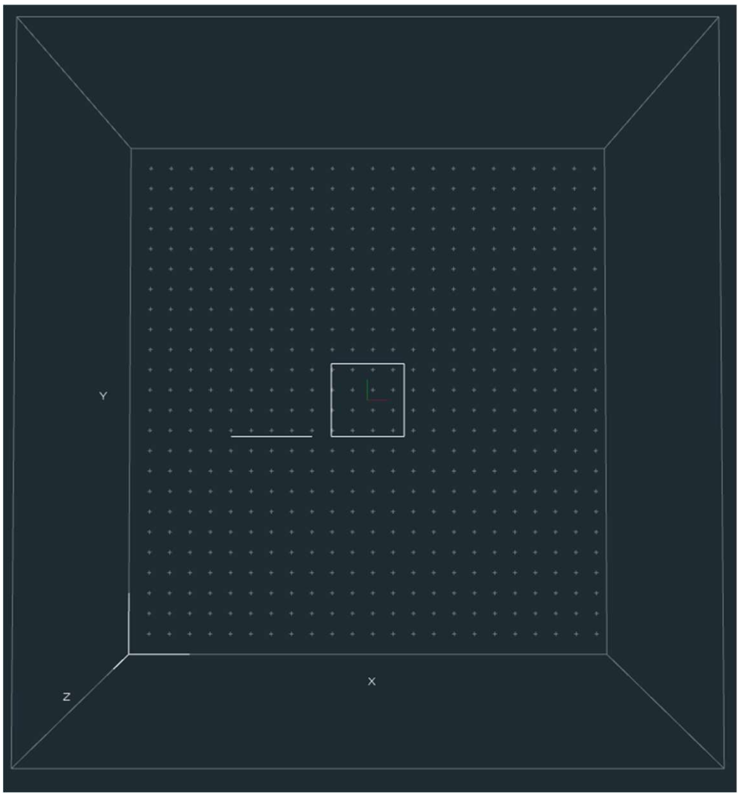

Figure 3.40 Geometry generated for the second Robocasting deposition trial through Voxalizer graphic interface with the addition of a simple geometry (line) before the extrusion of the actual geometry in order to avoid delayed extrusion and excessive ink deposition at the beginning of the process

Table 3.14 *Printing parameters set on Voxalizer for the second deposition trial*

PRINTING PARAMETERS	
Layer count	1
Layer height	0.6 mm
Pat width	80 mm
Travel speed	120 mm/s
Print speed	2 mm/s
Retraction height	10 mm
Retraction amount	0 mm
Retraction speed	10 mm/s
Retraction min distance	0
Extra length on restart	0 mm

The printing process is done on the 3YSZ square in order to optimize the positioning of the substrate for the final deposition process before joining. The result is shown in **Figure 3.41**. It can be observed that the generated geometry is continuous and homogeneous from the point of view of the path width. The deposited green part seemed to show good shape retention and self-support capability.

Figure 3.41 Printed shape with the parameters of Table 3.3 on 3YSZ substrate

A profilometric analysis is performed on the deposited green part after drying in an oven at 90 °C for 15 minutes. The reconstructed 3D object is reported in **Figure 3.42**. From the side view, it is possible to observe that the extruded filament does not have a perfectly uniform height, with a maximum height of 456 μm with respect to the layer height parameter set to 0.6 mm on the gcode.

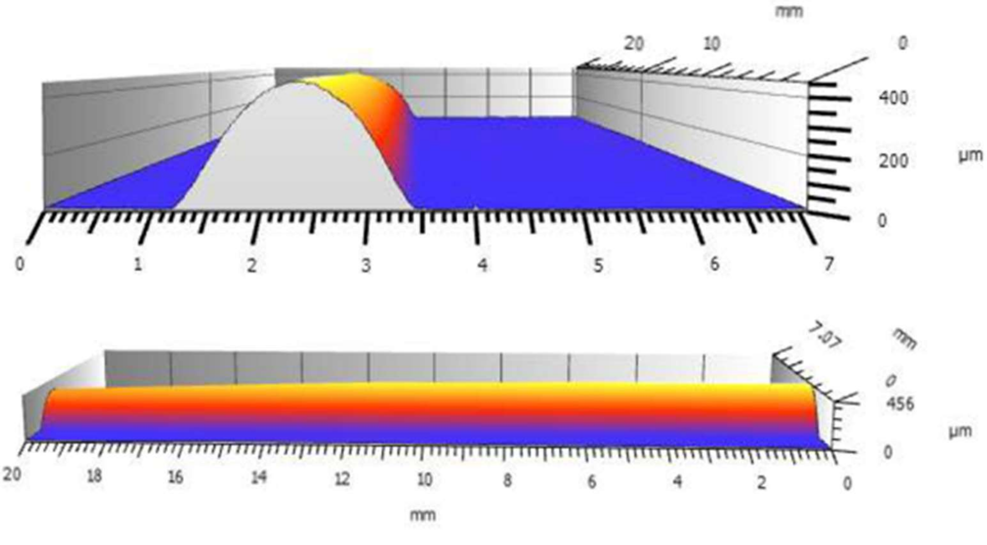

Figure 3.42 3D reconstruction through profilometric analysis of the Robocasting deposition of *Figure 3.41*.

A first attempt for the realization of the sample to be tested is done using the substrate in **Figure 3.41**. A weight of 15 g/cm^2 considering the area of the deposited filament is added to help the joining process, which is performed in furnace with a thermal treatment at 900 °C for 30 minutes with an ascending ramp of 5°C and a descending ramp of 3 °C/min. The result is shown in **Figure 3.43**.

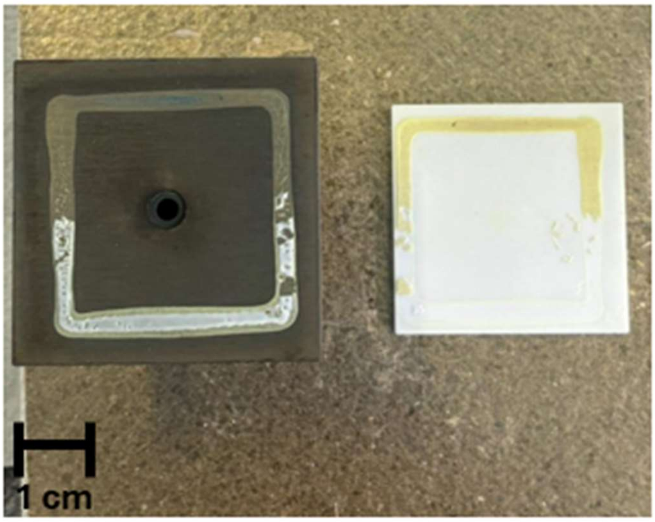

***Figure* 3.43** *First attempt for the realization of sample for high-pressure tightness testing*

The first attempt is unsuccessful, with the two substrates detaching immediately after the sample is removed from the oven, probably also due to the uneven weight distribution over the Crofer22 APU substrate.

The following attempt is done modifying the printing parameters for the sealant deposition, in order to obtain a wider and higher layer. The parameters of the last trial, for the realization of the joint in **Figure 2.17**, using a nozzle with a diameter of 1.6 mm, are reported in **Table 3.15**. The deposited filament is shown in **Figure 3.44**.

***Table* 3.15** *Printing parameters set on Voxalizer for the last deposition trial for the realization of the joined sample*

PRINTING PARAMETERS	
Layer count	1
Layer height	0.6 mm
Pat width	160 mm
Travel speed	120 mm/s
Print speed	1 mm/s
Retraction height	10 mm
Retraction amount	0 mm
Retraction speed	10 mm/s
Retraction min distance	0
Extra length on restart	0 mm

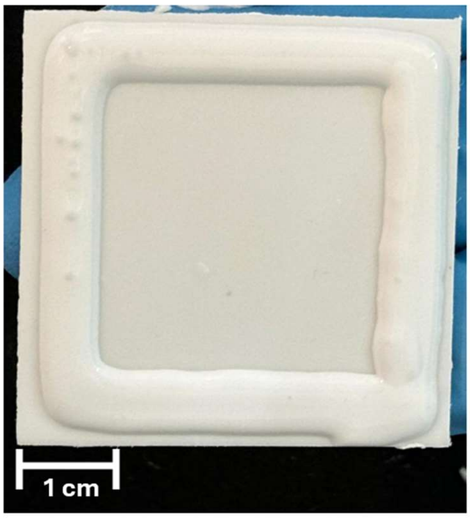

Figure 3.44 *Printed shape with the parameters of* ***Table 3.15*** *on 3YSZ substrate*

The joint is realized by placing the 3YSZ substrate on the Crofer22 APU substrate, followed by drying in oven at 90 °C for 30 minutes. Subsequently, a weight of 215 g, higher with respect to the 15 g/cm^2 which were generally used in this work, is placed on the 3YSZ. The thermal treatment used for the joining process involves a first ascending ramp of 1 °C to 120 °C, a second ascending ramp of 2 °C/min up to 300 °C and a final ascending ramp of 3 °C/min up to 900 °C, with a dwelling time of 30 minutes. Successively, a descending ramp of 1 °C is set. The joined sample is shown in **Figure 3.45**.

Figure 3.45 *Sample for high-pressure tightness test*

CONCLUSIONS

This thesis is focused on the characterization of sealants for SOEC applications at a temperature of 850 °C and a delta pressure of 5 bar. The sealant is a critical component in a SOEC stack as it has to fulfil two main tasks: avoiding gas mixing at the electrodes and providing electrical insulation to avoid short circuits in the stack. Furthermore, sealants must show suitable mechanical properties to withstand tensile and shear stresses arising during stack operation, in order to ensure system integrity.

Three commercial glass systems were considered as sealant for SOEC application, namely two barium-based glasses, MO-SCI 1862 and SCHOTT G018-392, and one strontium-based glass, MO-SCI 1729. The characterization of the glasses, was divided into four different sections: i) rheological characterization of glass powder loaded pastes for Robocasting deposition, ii) thermal characterization of the glasses through DSC and HSM analysis and thermomechanical characterization of the respective glass-ceramic systems through dilatometric analysis, iii) morphological and chemical characterization of the Crofer22APU/sealant/3YSZ joints through SEM, EDS and XRD analysis, iv) mechanical characterization of the Crofer22APU/sealant/3YSZ joints through SLO tests. As far as the substrates characterization is concerned, a profilometric analysis was done on Crofer22 APU and 3YSZ substrates in order to assess the surface roughness. Specifically, Croferr22 APU substrates were subjected to an Infrared Nanosecond fibre laser treatment in order to increase surface roughness and investigate its beneficial effects in increasing the mechanical interlocking effect, thus enhancing the adhesion of the sealing system. Finally, sealant deposition was performed through Robocasting for the realization of a sample for high-pressure tightness testing.

According to the rheological analysis results of equally formulated propylene glycol based pastes, the inks show a similar shear-thinning behaviour with viscosity decreasing for higher shear rates. However, despite the same particle size distribution, the three systems have different viscosity values, with MO-SCI 1862 being the most viscous one in a shear rate range from 0.01 to 100 s^{-1}, followed by MO-SCI 1729 and SCHOTT G018-392 pastes. Additionally, it was demonstrated that the addition of 3YSZ powder, having a lower size with respect to glass powder particles, to the pastes, maintaining unvaried the solid loading, lead to a reduction of viscosity over the whole range of applied shear rates. Finally, the variation of the solid loading was investigated, observing a significant increase in viscosity shifting from 75wt% to 80wt% solid loading.

The most relevant result of the thermal analysis is represented by the investigation of the SCHOTT G018-392+3YSZ system, processed through the homogeneous dispersion of 3YSZ powder in SCHOTT G018-392 paste. This system was considered due to the low characteristic temperatures and low viscosity at operating temperature of SCHOTT G018-392 system alone. Concerning the base systems, HSM analysis and DIL analysis on this composite system show an increase in viscosity and a reduction of the CTE, respectively.

The results of SEM analysis on the Crofer22APU/sealant/3YSZ joined samples were different depending on the analysed glass system. Crofer22APU/MO-SCI1862/3YSZ and Crofer22APU/MO-SCI 1729/3YSZ samples showed poor adhesion at both as-received Crofer22 APU and 3YSZ sides with cracks and discontinuous interfaces. However, both systems showed good infiltration in Crofer22 APU laser generated crevices. Crofer22APU/SCHOTTG018-392/3YSZ and Crofer22APU/SCHOTTG018-392+(5wt% and 10wt%)3YSZ/3YSZ samples presented good adhesion of the sealant at both interconnect and electrolyte material sides, with no relevant cracks or pores and continuous interfaces.

SLO mechanical tests at room temperature on Crofer22APU/SCHOTTG018-392/3YSZ and Crofer22APU/SCHOTTG018-392+10wt%3YSZ/3YSZ lead to good pure shear strength values of approximately 13 MPa and 17 MPa respectively, in line with the values found in scientific literature for other glass sealants considered for SOEC applications. Fracture surface modes observation highlighted an adhesive fracture to 3YSZ substrates or mixed fracture surface with sealant on both sides in case of samples processed with as-received Crofer22 APU. On the other hand, adhesive fracture with sealant on Crofer22 APU sides was observed for samples realized with laser-machined Crofer22 APU substrates. This results lead to the conclusion that enhanced surface roughness of the substates obtained through laser processing can have positive effect on the adhesion of the sealant.

One Crofer22APU(lasered)/MO-SCI1862/3YSZ sample and one Crofer22APU(lasered)/MO-SCI1729/3YSZ sample were subjected to SLO test obtaining poor shear strength values of 1.4 and 4.1 MPa, respectively. However, a broader experimental campaign should be done before excluding these systems.

Basing on the obtained experimental results, the SCHOTT G018-392+10wt%3YSZ was chosen for the preparation of the sample for high-pressure tightness testing. Specifically, the paste with a solid loading of the 80wt% was selected, according to the better rheological properties for the paste with a solid loading of the 75wt%. The Robocasting printing parameters were modified to obtain a filament having uniform height and width.

Additional optimization, in terms of pressure balancing and fixtures during the joining treatment are foreseen.

The results of this research support the idea that the strategy of surface modification can substantially modify the shear strength resistance and the fracture mode of metal to ceramic joined samples; this concept will be validated with a shear strength assessment at 850°C.

BIBLIOGRAPHY

[1] J. Becker, «Joint Research Centre», *Nature*, vol. 296, fasc. 5855, pp. 283–283, mar. 1982, doi: 10.1038/296283c0.

[2] «Net Zero Roadmap: A Global Pathway to Keep the 1.5 °C Goal in Reach - 2023 Update».

[3] «Global Hydrogen Review 2023», 2023.

[4] S. Shiva Kumar e H. Lim, «An overview of water electrolysis technologies for green hydrogen production», *Energy Rep.*, vol. 8, pp. 13793–13813, nov. 2022, doi: 10.1016/j.egyr.2022.10.127.

[5] Q. Hassan, V. S. Tabar, A. Z. Sameen, H. M. Salman, e M. Jaszczur, «A review of green hydrogen production based on solar energy; techniques and methods», *Energy Harvest. Syst.*, vol. 11, fasc. 1, p. 20220134, gen. 2024, doi: 10.1515/ehs-2022-0134.

[6] «https://medium.com/phystechventures/natural-hydrogen-as-a-mineral-resource-5e3281a177df».

[7] *Green hydrogen cost reduction: scaling up electrolysers to meet the 1.5^0 C climate goal*. Abu Dhabi: Irena, 2020.

[8] M. Götz *et al.*, «Renewable Power-to-Gas: A technological and economic review», *Renew. Energy*, vol. 85, pp. 1371–1390, gen. 2016, doi: 10.1016/j.renene.2015.07.066.

[9] European Commission. Joint Research Centre., *Current status of chemical energy storage technologies: trends in research, development and deployment in Europe and the rest of the world.* LU: Publications Office, 2020. Consultato: 31 marzo 2024. [Online]. Disponibile su: https://data.europa.eu/doi/10.2760/280873

[10] X. Sun *et al.*, «Earth-Abundant Electrocatalysts in Proton Exchange Membrane Electrolyzers», *Catalysts*, vol. 8, fasc. 12, p. 657, dic. 2018, doi: 10.3390/catal8120657.

[11] M. A. Laguna-Bercero, A c. di, *High Temperature Electrolysis*, vol. 95. in Lecture Notes in Energy, vol. 95. Cham: Springer International Publishing, 2023. doi: 10.1007/978-3-031-22508-6.

[12] J. Lei, H. Ma, G. Qin, Z. Guo, P. Xia, e C. Hao, «A Comprehensive Review on the Power Supply System of Hydrogen Production Electrolyzers for Future Integrated Energy Systems», *Energies*, vol. 17, fasc. 4, p. 935, feb. 2024, doi: 10.3390/en17040935.

[13] S. E. Wolf *et al.*, «Solid oxide electrolysis cells – current material development and industrial application», *J. Mater. Chem. A*, vol. 11, fasc. 34, pp. 17977–18028, 2023, doi: 10.1039/D3TA02161K.

[14] Y. Zheng *et al.*, «A review of high temperature co-electrolysis of H_2O and CO_2 to produce sustainable fuels using solid oxide electrolysis cells (SOECs): advanced materials and technology», *Chem. Soc. Rev.*, vol. 46, fasc. 5, pp. 1427–1463, 2017, doi: 10.1039/C6CS00403B.

[15] M. Henke, C. Willich, J. Kallo, e K. A. Friedrich, «Theoretical study on pressurized operation of solid oxide electrolysis cells», *Int. J. Hydrog. Energy*, vol. 39, fasc. 24, pp. 12434–12439, ago. 2014, doi: 10.1016/j.ijhydene.2014.05.185.

[16] M. Riedel, M. P. Heddrich, e K. A. Friedrich, «Analysis of pressurized operation of 10 layer solid oxide electrolysis stacks», *Int. J. Hydrog. Energy*, vol. 44, fasc. 10, pp. 4570–4581, feb. 2019, doi: 10.1016/j.ijhydene.2018.12.168.

[17] S. H. Jensen, C. Graves, M. Chen, J. B. Hansen, e X. Sun, «Characterization of a Planar Solid Oxide Cell Stack Operated at Elevated Pressure», *J. Electrochem. Soc.*, vol. 163, fasc. 14, pp. F1596–F1604, 2016, doi: 10.1149/2.1171614jes.

[18] S. Zarabi Golkhatmi, M. I. Asghar, e P. D. Lund, «A review on solid oxide fuel cell durability: Latest progress, mechanisms, and study tools», *Renew. Sustain. Energy Rev.*, vol. 161, p. 112339, giu. 2022, doi: 10.1016/j.rser.2022.112339.

[19] G. Flis e G. Wakim, «Solid Oxide Electrolysis: A Technology Status Assessment».

[20] A. Pandiyan, A. Uthayakumar, R. Subrayan, S. W. Cha, e S. B. Krishna Moorthy, «Review of solid oxide electrolysis cells: a clean energy strategy for hydrogen generation», *Nanomater. Energy*, vol. 8, fasc. 1, pp. 2–22, giu. 2019, doi: 10.1680/jnaen.18.00009.

[21] L. A. Jolaoso, I. T. Bello, O. A. Ojelade, A. Yousuf, C. Duan, e P. Kazempoor, «Operational and scaling-up barriers of SOEC and mitigation strategies to boost H2 production- a comprehensive review», *Int. J. Hydrog. Energy*, vol. 48, fasc. 85, pp. 33017–33041, ott. 2023, doi: 10.1016/j.ijhydene.2023.05.077.

[22] «electrolyser IEA citazione per applicazioni SOEC in industria», [Online]. Disponibile su: https://www.iea.org/energy-system/low-emission-fuels/electrolysers

[23] M. Ni, M. Leung, e D. Leung, «Technological development of hydrogen production by solid oxide electrolyzer cell (SOEC)», *Int. J. Hydrog. Energy*, vol. 33, fasc. 9, pp. 2337–2354, mag. 2008, doi: 10.1016/j.ijhydene.2008.02.048.

[24] P. Atkins, J. D. Paula, e J. Keeler, *Atkins' Physical Chemistry*, 12^a ed. Oxford University Press, 2022. doi: 10.1093/hesc/9780198847816.001.0001.

[25] J. Larminie e A. Dicks, *Fuel cell systems explained*, 2. Aufl., Nachdruck. Chichester Weinheim: Wiley, 2009.

[26] A. Tarancón e V. Esposito, «3D Printing for Energy Applications».

[27] A. Zhakeyev, P. Wang, L. Zhang, W. Shu, H. Wang, e J. Xuan, «Additive Manufacturing: Unlocking the Evolution of Energy Materials», *Adv. Sci.*, vol. 4, fasc. 10, p. 1700187, ott. 2017, doi: 10.1002/advs.201700187.

[28] «https://doi.org/10.1002/wene.96».

[29] A. Nechache e S. Hody, «Alternative and innovative solid oxide electrolysis cell materials: A short review», *Renew. Sustain. Energy Rev.*, vol. 149, p. 111322, ott. 2021, doi: 10.1016/j.rser.2021.111322.

[30] M. A. Laguna-Bercero, «Recent advances in high temperature electrolysis using solid oxide fuel cells: A review», *J. Power Sources*, vol. 203, pp. 4–16, apr. 2012, doi: 10.1016/j.jpowsour.2011.12.019.

[31] H. Hayashi, T. Saitou, N. Maruyama, H. Inaba, K. Kawamura, e M. Mori, «Thermal expansion coefficient of yttria stabilized zirconia for various yttria contents», *Solid State Ion.*, vol. 176, fasc. 5–6, pp. 613–619, feb. 2005, doi: 10.1016/j.ssi.2004.08.021.

[32] N. Mahato, A. Banerjee, A. Gupta, S. Omar, e K. Balani, «Progress in material selection for solid oxide fuel cell technology: A review», *Prog. Mater. Sci.*, vol. 72, pp. 141–337, lug. 2015, doi: 10.1016/j.pmatsci.2015.01.001.

[33] P. A. Connor *et al.*, «Tailoring SOFC Electrode Microstructures for Improved Performance», *Adv. Energy Mater.*, vol. 8, fasc. 23, p. 1800120, ago. 2018, doi: 10.1002/aenm.201800120.

[34] S. Biswas, G. Kaur, G. Paul, e S. Giddey, «A critical review on cathode materials for steam electrolysis in solid oxide electrolysis», *Int. J. Hydrog. Energy*, vol. 48, fasc. 34, pp. 12541–12570, apr. 2023, doi: 10.1016/j.ijhydene.2022.11.307.

[35] D. A. Osinkin *et al.*, «Thermal expansion, gas permeability, and conductivity of Ni-YSZ anodes produced by different techniques», *J. Solid State Electrochem.*, vol. 18, fasc. 1, pp. 149–156, gen. 2014, doi: 10.1007/s10008-013-2239-4.

[36] S. P. Jiang e S. H. Chan, «A review of anode materials development in solid oxide fuel cells», *J. Mater. Sci.*, vol. 39, fasc. 14, pp. 4405–4439, lug. 2004, doi: 10.1023/B:JMSC.0000034135.52164.6b.

[37] G. Zou, W.-C. Feng, Y.-F. Song, e G.-X. Wang, «Recent Advances in Anode Materials of Solid Oxide Electrolysis Cells».

[38] J.-H. Kim, R.-H. Song, J.-H. Kim, T.-H. Lim, Y.-K. Sun, e D.-R. Shin, «Co-synthesis of nano-sized LSM–YSZ composites with enhanced electrochemical property», *J. Solid State Electrochem.*, vol. 11, fasc. 10, pp. 1385–1390, lug. 2007, doi: 10.1007/s10008-007-0317-1.

[39] A. Princivalle e E. Djurado, «Nanostructured LSM/YSZ composite cathodes for IT-SOFC: A comprehensive microstructural study by electrostatic spray deposition», *Solid State Ion.*, vol. 179, fasc. 33–34, pp. 1921–1928, ott. 2008, doi: 10.1016/j.ssi.2008.05.006.

[40] J. Schefold, A. Brisse, e F. Tietz, «Nine Thousand Hours of Operation of a Solid Oxide Cell in Steam Electrolysis Mode», *J. Electrochem. Soc.*, vol. 159, p. A137, gen. 2012, doi: 10.1149/2.076202jes.

[41] A. Petric, P. Huang, e F. Tietz, «Evaluation of La–Sr–Co–Fe–O perovskites for solid oxide fuel cells and gas separation membranes», *Solid State Ion.*, vol. 135, fasc. 1, pp. 719–725, 2000, doi: https://doi.org/10.1016/S0167-2738(00)00394-5.

[42] Z. Yang, K. S. Weil, D. M. Paxton, e J. W. Stevenson, «Selection and Evaluation of Heat-Resistant Alloys for SOFC Interconnect Applications», *J. Electrochem. Soc.*, vol. 150, fasc. 9, p. A1188, 2003, doi: 10.1149/1.1595659.

[43] J. W. Fergus, «Metallic interconnects for solid oxide fuel cells», *Mater. Sci. Eng. A*, vol. 397, fasc. 1–2, pp. 271–283, apr. 2005, doi: 10.1016/j.msea.2005.02.047.

[44] L. C. Ajitdoss, F. Smeacetto, M. Bindi, D. Beretta, M. Salvo, e M. Ferraris, «Mn1.5Co1.5O4 protective coating on Crofer22APU produced by thermal co-evaporation for SOFCs», *Mater. Lett.*, vol. 95, pp. 82–85, mar. 2013, doi: 10.1016/j.matlet.2012.12.079.

[45] D. U. Tulyaganov, A. A. Reddy, V. V. Kharton, e J. M. F. Ferreira, «Aluminosilicate-based sealants for SOFCs and other electrochemical applications − A brief review», *J. Power Sources*, vol. 242, pp. 486–502, nov. 2013, doi: 10.1016/j.jpowsour.2013.05.099.

[46] J. W. Fergus, «Sealants for solid oxide fuel cells», *J. Power Sources*, vol. 147, fasc. 1–2, pp. 46–57, set. 2005, doi: 10.1016/j.jpowsour.2005.05.002.

[47] F. Smeacetto, M. Salvo, F. D. D'Hérin Bytner, P. Leone, e M. Ferraris, «New glass and glass–ceramic sealants for planar solid oxide fuel cells», *J. Eur. Ceram. Soc.*, vol. 30, fasc. 4, pp. 933–940, mar. 2010, doi: 10.1016/j.jeurceramsoc.2009.09.033.

[48] J. E. Shelby, *Introduction to Glass Science and Technology*. The Royal Society of Chemistry, 2005. doi: 10.1039/9781847551160.

[49] M. Kerstan e C. Rüssel, «Barium silicates as high thermal expansion seals for solid oxide fuel cells studied by high-temperature X-ray diffraction (HT-XRD)», *J. Power Sources*, vol. 196, pp. 7578–7584, set. 2011, doi: 10.1016/j.jpowsour.2011.04.035.

[50] G. N. Shabanova, V. V. Taranenkova, A. N. Korogodskaya, e E. V. Khristich, «Structure of the BaO—Al $_2$ O $_3$ —SiO $_2$ System (A Review)», *ChemInform*, vol. 34, fasc. 47, p. chin.200347238, nov. 2003, doi: 10.1002/chin.200347238.

[51] A. Rost, «Degradation of Sealing Glasses for SOFC under Electrical Load and Dual Atmosphere», *J. Ceram. Sci. Tech.*, fasc. 02, 2012, doi: 10.4416/JCST2012-00002.

[52] H. Javed *et al.*, «Glass-Ceramic Sealants for SOEC: Thermal Characterization and Electrical Resistivity in Dual Atmosphere», *Energies*, vol. 13, fasc. 14, p. 3682, lug. 2020, doi: 10.3390/en13143682.

[53] M. Ferraris *et al.*, «Torsional shear strength behavior of advanced glass-ceramic sealants for SOFC/SOEC applications», *J. Eur. Ceram. Soc.*, vol. 40, fasc. 12, pp. 4067–4075, set. 2020, doi: 10.1016/j.jeurceramsoc.2020.04.034.

[54] M. Fakouri Hasanabadi, A. H. Kokabi, M. A. Faghihi-Sani, S. M. Groß-Barsnick, e J. Malzbender, «Room- and high-temperature torsional shear strength of solid oxide fuel/electrolysis cell sealing material», *Ceram. Int.*, vol. 45, fasc. 2, pp. 2219–2225, feb. 2019, doi: 10.1016/j.ceramint.2018.10.134.

[55] M. J. Da Silva, J. F. Bartolomé, A. H. De Aza, e S. Mello-Castanho, «Glass ceramic sealants belonging to BAS (BaO–Al 2 O 3 –SiO 2) ternary system modified with B 2 O 3 addition: A different approach to access the SOFC seal issue», *J. Eur. Ceram. Soc.*, vol. 36, fasc. 3, pp. 631–644, feb. 2016, doi: 10.1016/j.jeurceramsoc.2015.10.005.

[56] S. Rodríguez-López *et al.*, «Mechanical properties of solid oxide fuel cell glass-ceramic sealants in the system BaO/SrO-MgO-B2O3-SiO2», *J. Eur. Ceram. Soc.*, vol. 37, fasc. 11, pp. 3579–3594, set. 2017, doi: 10.1016/j.jeurceramsoc.2017.03.054.

[57] H. Javed *et al.*, «Shear Performance at Room and High Temperatures of Glass–Ceramic Sealants for Solid Oxide Electrolysis Cell Technology», *Materials*, vol. 12, fasc. 2, p. 298, gen. 2019, doi: 10.3390/ma12020298.

[58] H. Javed *et al.*, «Novel SrO-Containing Glass-Ceramic Sealants for Solid Oxide Electrolysis Cells (SOEC): Their Design and Characterization under Relevant Conditions», *Materials*, vol. 15, fasc. 17, p. 5805, ago. 2022, doi: 10.3390/ma15175805.

[59] Y.-S. Chou, J. W. Stevenson, e P. Singh, «Effect of pre-oxidation and environmental aging on the seal strength of a novel high-temperature solid oxide fuel cell (SOFC) sealing glass with metallic interconnect», *J. Power Sources*, vol. 184, fasc. 1, pp. 238–244, set. 2008, doi: 10.1016/j.jpowsour.2008.06.020.

[60] Y.-S. Chou, J. W. Stevenson, G.-G. Xia, e Z.-G. Yang, «Electrical stability of a novel sealing glass with (Mn,Co)-spinel coated Crofer22APU in a simulated SOFC dual environment», *J. Power Sources*, vol. 195, fasc. 17, pp. 5666–5673, set. 2010, doi: 10.1016/j.jpowsour.2010.03.052.

[61] «Fuel Cells - 2015 - Selçuk - Measurement of Mechanical Strength of Glass-to-Metal Joints (1).pdf».

[62] M. Ferraris, A. Ventrella, M. Salvo, M. Avalle, F. Pavia, e E. Martin, «Comparison of shear strength tests on AV119 epoxy-joined carbon/carbon composites», *Compos. Part B Eng.*, vol. 41, fasc. 2, pp. 182–191, mar. 2010, doi: 10.1016/j.compositesb.2009.10.008.

[63] F. Smeacetto *et al.*, «Torsional behaviour of glass-joined, laser-processed Crofer 22 APU interconnect: Unravelling the effect of surface roughness on the shear strength», *Ceram. Int.*, vol. 48, fasc. 22, pp. 32837–32843, nov. 2022, doi: 10.1016/j.ceramint.2022.07.210.

[64] C. Sun, Y. Wang, M. D. McMurtrey, N. D. Jerred, F. Liou, e J. Li, «Additive manufacturing for energy: A review», *Appl. Energy*, vol. 282, p. 116041, gen. 2021, doi: 10.1016/j.apenergy.2020.116041.

[65] A. Pesce, A. Hornés, M. Núñez, A. Morata, M. Torrell, e A. Tarancón, «3D printing the next generation of enhanced solid oxide fuel and electrolysis cells», *J. Mater. Chem. A*, vol. 8, fasc. 33, pp. 16926–16932, 2020, doi: 10.1039/D0TA02803G.

[66] M. R. Weimar, L. A. Chick, D. W. Gotthold, e G. A. Whyatt, «Cost Study for Manufacturing of Solid Oxide Fuel Cell Power Systems», PNNL--22732, 1126362, set. 2013. doi: 10.2172/1126362.

[67] S. Masciandaro, M. Torrell, P. Leone, e A. Tarancón, «Three-dimensional printed yttria-stabilized zirconia self-supported electrolytes for solid oxide fuel cell applications», *J. Eur. Ceram. Soc.*, vol. 39, fasc. 1, pp. 9–16, gen. 2019, doi: 10.1016/j.jeurceramsoc.2017.11.033.

[68] L. Wei *et al.*, «A novel fabrication of yttria-stabilized-zirconia dense electrolyte for solid oxide fuel cells by 3D printing technique», *Int. J. Hydrog. Energy*, vol. 44, fasc. 12, pp. 6182–6191, mar. 2019, doi: 10.1016/j.ijhydene.2019.01.071.

[69] R. I. Tomov *et al.*, «Direct ceramic inkjet printing of yttria-stabilized zirconia electrolyte layers for anode-supported solid oxide fuel cells», *J. Power Sources*, vol. 195, fasc. 21, pp. 7160–7167, nov. 2010, doi: 10.1016/j.jpowsour.2010.05.044.

[70] V. Esposito *et al.*, «Fabrication of thin yttria-stabilized-zirconia dense electrolyte layers by inkjet printing for high performing solid oxide fuel cells», *J. Power Sources*, vol. 273, pp. 89–95, gen. 2015, doi: 10.1016/j.jpowsour.2014.09.085.

[71] S. Anelli, M. Rosa, F. Baiutti, M. Torrell, V. Esposito, e A. Tarancón, «Hybrid-3D printing of symmetric solid oxide cells by inkjet printing and robocasting», *Addit. Manuf.*, vol. 51, p. 102636, 2022, doi: https://doi.org/10.1016/j.addma.2022.102636.

[72] D. A. Rau, C. B. Williams, e M. J. Bortner, «Rheology and printability: A survey of critical relationships for direct ink write materials design», *Prog. Mater. Sci.*, vol. 140, p. 101188, dic. 2023, doi: 10.1016/j.pmatsci.2023.101188.

[73] F. Jin *et al.*, «Optimisation and application of high solid loading stereolithography 3D printing ceramic cores slurry», *Ceram. Int.*, vol. 50, fasc. 2, pp. 3574–3583, gen. 2024, doi: 10.1016/j.ceramint.2023.11.107.

[74] J. Mewis e N. J. Wagner, *Colloidal Suspension Rheology*, 1ª ed. Cambridge University Press, 2011. doi: 10.1017/CBO9780511977978.

[75] H. A. Barnes, *A handbook of elementary rheology*. Aberystwyth: University of Wales Institute of Non-Newtonian Fluid Mechanics, 2000.

[76] J. Jacob, S. Grelier, M. Grau, e B. Chorein, «Effect of Dispersing Agents on the Stability of Recycled Paints», *Coatings*, vol. 12, fasc. 11, p. 1722, nov. 2022, doi: 10.3390/coatings12111722.

[77] N. Wang *et al.*, «Preparation of High-Stability Ceramic Slurry with Gel Behavior for Stereolithography 3D Printing», *Materials*, vol. 16, fasc. 7, p. 2816, apr. 2023, doi: 10.3390/ma16072816.

[78] A. Pesce, A. Hornés, M. Núñez, A. Morata, M. Torrell, e A. Tarancón, «3D printing the next generation of enhanced solid oxide fuel and electrolysis cells», *J. Mater. Chem. A*, vol. 8, fasc. 33, pp. 16926–16932, 2020, doi: 10.1039/D0TA02803G.

[79] S. Márquez *et al.*, «3D printed electrolyte-supported solid oxide cells based on Ytterbium-doped scandia-stabilized zirconia», *J. Phys. Energy*, vol. 6, fasc. 1, p. 015016, gen. 2024, doi: 10.1088/2515-7655/ad17e3.

[80] A. M. Martos *et al.*, «3D printing of reversible solid oxide cell stacks for efficient hydrogen production and power generation», *J. Power Sources*, vol. 609, p. 234704, lug. 2024, doi: 10.1016/j.jpowsour.2024.234704.

[81] N. Mex, P. D. Calvert, e de Angelis, «75 Inventors: Joseph Cesarano, III, Albuquerque»,.

[82] J. Cesarano, «A Review of Robocasting Technology», *MRS Proc.*, vol. 542, p. 133, 1998, doi: 10.1557/PROC-542-133.

[83] M. Kuhn, T. Napporn, M. Meunier, S. Vengallatore, e D. Therriault, «Direct-write microfabrication of single-chamber micro solid oxide fuel cells», *J. Micromechanics Microengineering*, vol. 18, fasc. 1, p. 015005, gen. 2008, doi: 10.1088/0960-1317/18/1/015005.

[84] S. Lamnini, H. Elsayed, Y. Lakhdar, F. Baino, F. Smeacetto, e E. Bernardo, «Robocasting of advanced ceramics: ink optimization and protocol to predict the printing parameters - A review», *Heliyon*, vol. 8, fasc. 9, p. e10651, set. 2022, doi: 10.1016/j.heliyon.2022.e10651.

[85] V. Saggiomo, «3D Printed Devices for Catalytic Systems», in *Catalyst Immobilization*, 1ª ed., M. Benaglia e A. Puglisi, A c. di, Wiley, 2020, pp. 369–408. doi: 10.1002/9783527817290.ch11.

[86] «Massimo Rosa - PhD Thesis.pdf».

[87] A. M'Barki, L. Bocquet, e A. Stevenson, «Linking Rheology and Printability for Dense and Strong Ceramics by Direct Ink Writing», *Sci. Rep.*, vol. 7, fasc. 1, p. 6017, lug. 2017, doi: 10.1038/s41598-017-06115-0.

[88] «https://wiki.anton-paar.com/it-it/scansioni-di-ampiezza/».

[89] «https://mo-sci.com/wp-content/uploads/2021/11/GL1862-Data-Sheet-1.pdf».

[90] «https://mo-sci.com/wp-content/uploads/2022/11/GL1729-Data-Sheet.pdf».

[91] SCHOTT AG, «Preliminary Data Sheet - Glass No: G018-392».

[92] «https://www.gdandtbasics.com/what-is-a-profilometer/».

[93] R. Deltombe, K. J. Kubiak, e M. Bigerelle, «2. How to select the most relevant 3D roughness parameters of a surface», *Scanning*, vol. 36, fasc. 1, pp. 150–160, gen. 2014, doi: 10.1002/sca.21113.

[94] E. S. Gadelmawla, M. M. Koura, T. M. A. Maksoud, I. M. Elewa, e H. H. Soliman, «1. Roughness parameters», *J. Mater. Process. Technol.*, vol. 123, fasc. 1, pp. 133–145, apr. 2002, doi: 10.1016/S0924-0136(02)00060-2.

[95] T. Altan e S. Celik, «3. Effect of surface roughness of the metallic interconnects on the bonding strength in solid oxide fuel cells», *Int. J. Hydrog. Energy*, vol. 45, fasc. 60, pp. 35118–35129, dic. 2020, doi: 10.1016/j.ijhydene.2020.03.136.

[96] M. Pascual, A. Duran, e M. Prado, «A New Method for Determining Fixed Viscosity Points of Glasses», *Eur. J. Glass Sci. Technol. Part B Phys. Chem. Glas.*, vol. 46, pp. 512–520, set. 2005.

[97] «viscosity-points (1).pdf».

[98] «Pascual, M.J.; Pascual, L.; Durán, A. Determination of the viscosity temperature curve for glasses on the basis of fixed viscosity points determined by hot stage microscopy. Phys. Chem. Glasses 2001, 42, 61–66.».

[99] «Scholze H (1962) Der Einfluss Von Viskositaet Und Oberflchenspannung Auf Erhitzungsmikroskopische Messungen an Glaesern Berichte Der Deutschen Keramischen Gesellschaft 59:63–68».

[100] A. Zawada, M. Lubas, e A. Nowak, «Experimental vs. Theoretical Viscosity Determination of Aluminosilicate Glasses», *Materials*, vol. 16, fasc. 17, p. 5789, ago. 2023, doi: 10.3390/ma16175789.

[101] «DIL_Classic_en_web.pdf».

[102] «15_ DHR_Rheology_Theory.pdf».

[103] M. Ferraris, M. Salvo, V. Casalegno, S. De La Pierre, L. Goglio, e A. Benelli, «Torsion Test vs. Other Methods to Obtain the Shear Strength of Elastic-Plastic Adhesives», *Appl. Sci.*, vol. 12, fasc. 7, p. 3284, mar. 2022, doi: 10.3390/app12073284.

[104] M. Brochu, B. D. Gauntt, R. Shah, G. Miyake, e R. E. Loehman, «Comparison between barium and strontium-glass composites for sealing SOFCs», *J. Eur. Ceram. Soc.*, vol. 26, fasc. 15, pp. 3307–3313, gen. 2006, doi: 10.1016/j.jeurceramsoc.2005.08.002.

[105] P. Rao e R. N. Singh, «Sintering and thermal expansion behaviors of glass and glass–YSZ composites as self-repairable seals for SOFC», *J. Am. Ceram. Soc.*, vol. 106, fasc. 1, pp. 157–165, gen. 2023, doi: 10.1111/jace.18534.